

**Investigation of Advanced Material Through Digital Volume Correlation Measurement  
Techniques**

**Cristofaro Salvatore Timpano**

A THESIS SUBMITTED TO THE FACULTY OF GRADUATE STUDIES IN PARTIAL  
FULFILLMENT OF THE REQUIREMENTS FOR THE DEGREE OF MASTER OF APPLIED  
SCIENCE

Graduate Program in Mechanical Engineering

York University

Toronto, Ontario

October 2020

© Cristofaro Salvatore Timpano, 2020

## ii Abstract

Composite materials are seeing increased industrial usage in high-performance applications where lightweight, high-strength, and material tailorability is required. Due to their heterogeneous structure, displacement and strain fields developed under loading conditions are often complex and difficult to predict. Digital volume correlation (DVC) offers a novel method for the deformation analysis of composite structures. Through the utilization of micro-computed tomography datasets can be obtained and utilized to visualize three-dimensional dataset for DVC. This thesis explores the utilization of DVC for the analysis of composite materials. A methodology is developed based on artificially seeding materials with micro-particles to acquire the sufficient image contrast. A rigid body displacement test is then utilized to evaluate the errors associated with each particle, narrow DVC parameters, and select between particles. Utilizing this methodology displacement and strain fields were obtained for copper seeded epoxy, and 3D printed copper impregnated PLA sample under compressive, and tensile loading respectively.

### **iii Dedication**

This thesis is dedicated to my loving parents, Daniele and Caterina Timpano, brother, Matteo Timpano, grandfather, Damiano Angilletta, and grandmother, Raphaella Angilletta who passed away during the writing of this thesis.

## **iv Acknowledgments**

I would like to extend my deepest gratitude to my supervisor Dr. Garrett Melenka for the opportunity to do my research under his guidance. Dr. Garrett Melenka vision, and guidance for my research has helped inspire me throughout my researcher term with him. His open availability, and “no question is a bad question” attitude exemplified him as a consummate professional and mentor. This aided me in developing a clear sense of direction for my research and always providing me with a path forward. He taught me how to develop a clear experimental methodology, to help achieve my desired research goals. Dr. Melenka instilled a sense of open mindedness toward the implications of research and criticality required from a researcher. It was truly a privilege to work under Dr. Melenka’s supervision where I gain many skills that I could utilize in both my professional and personal life. I would like to extend my appreciation for his help and consider him not only an exemplary supervisor, but a close friend.

I would also like to acknowledge all my close lab and research mates who are too many to mention individually. You always made the research space both fun and inviting place. As true friends everyone had an unselfish attitude and wanted to provide help in anyway, they could toward each other’s research. The support provided by everyone was something I will never forget, as you were all always there when I required your assistance. Everyone’s differing perspective aided me in the development of my thesis work. Beyond academics, our time spent outside the lab space was consistently entertaining.

## v Table of Contents

ii	Abstract.....	ii
iii	Dedication.....	iii
iv	Acknowledgments .....	iv
v	Table of Contents.....	v
vi	List of Tables .....	x
vii	List of Figures.....	xii
viii	List of Abbreviations .....	xvi
ix	List of Variables .....	xvii
	Chapter 1: Introduction.....	1
	1.1 Motivation .....	1
	1.2 Thesis Objective.....	3
	1.3 Thesis Scope.....	3
	1.4 Thesis outline .....	4
	1.5 References .....	5
	Chapter 2: Literature Review .....	8
	2.1 Introduction .....	8
	2.2 Composites .....	9
	2.2.1 Fundamentals of Composites.....	9
	2.2.2 Composite Classification .....	11

2.2.3	Laminate Composites.....	12
2.2.4	Braided Composites .....	14
2.2.5	Injection Moulding Composites.....	18
2.2.6	Fused Filament Fabrication (FFF) Composites .....	20
2.3	Digital Image Correlation.....	22
2.3.1	Image Acquisition for Surface Measurements.....	22
2.3.2	Fundamentals of DIC .....	23
2.3.3	DIC for Mechanics of Materials .....	27
2.4	Volume Measurements and Digital Volume Correlation.....	31
2.4.1	Fundamentals of Micro-Computed Tomography .....	31
2.4.2	Micro-Computed Tomography for Composite Analysis .....	32
2.4.3	Fundamentals of Digital Volume Correlation (DVC) .....	36
2.4.4	Open-Source DVC .....	38
2.4.5	DVC Contrast Enhancement.....	39
2.4.6	DVC of Trabecular Bone .....	40
2.4.7	DVC of Traditional Materials.....	42
2.4.8	DVC of Composite and Non-Traditional Materials.....	44
2.4.9	Gaps in Literature .....	47
2.5	Conclusion.....	49
2.6	References .....	49

Chapter 3: Artificial Seeding for Micro-Computed Tomography Image Contrast Enhancement

for Digital Volume Correlation ..... 61

3.1 Introduction ..... 61

3.2 Methodology ..... 65

3.2.1 Sample Preparation ..... 65

3.2.2 Computed Tomography ..... 67

3.2.3 Pre-Processing for Digital Volume Correlation..... 70

3.2.4 Contrast, Particle Distribution and Cross-Correlation Measurement ..... 71

3.2.5 Digital Volume Correlation ..... 73

3.2.6 Artificial Displacement Error Calculations ..... 73

3.2.7 Effects of Data Downsampling..... 75

3.2.8 DVC Displacement and Strain..... 75

3.3 Results and Discussion..... 78

3.3.1 Particle Selection ..... 78

3.3.2 Artificial Displacement Error Calculations ..... 84

3.3.3 Sample Displacement..... 89

3.3.4 Strain Data ..... 92

3.4 Conclusion..... 96

3.5 References ..... 98

Chapter 4: Digital Volume Correlation Analysis of PLA based fused filament fabrication

copper infused composites* .....	104
4.1 Introduction .....	104
4.2 Methodology .....	108
4.2.1 Manufacturing.....	108
4.2.2 Micro-Computed Tomography .....	110
4.2.3 Reconstruction .....	112
4.2.4 Image Segmentation.....	114
4.2.5 Digital Volume Correlation .....	121
4.3 Results and Discussion.....	124
4.3.1 Image Segmentation.....	124
4.3.2 Digital Volume Correlation of Downsampled data .....	129
4.4 Conclusions .....	139
4.5 References .....	140
Chapter 5: Conclusions, Recommendations, and Future Works .....	146
5.1 Conclusions .....	146
5.2 Recommendations .....	152
5.3 Future Works.....	154
Appendices .....	156
Appendix A: Image Segmentation Formulations .....	156



Appendix B: MATLAB Code..... 162

## vi List of Tables

Table 2-1: Summary of inputs used in micro-CT for DVC experiments .....	47
Table 2-2: Summary of input parameters for DVC software .....	48
Table 3-1: Size and density of particles used for epoxy seeding .....	67
Table 3-2: Scanning parameters utilized for acquiring tomographs of seeded epoxy.....	69
Table 3-3: Image sizes utilized for DVC measurements .....	72
Table 3-4: Greyscale thresholds utilized for particle segmentation.....	73
Table 3-5: Correlation parameters used with FIDVC for subset and artificial displacement accuracy test.....	75
Table 3-6: DVC parameters utilized to determine optimal overlap between subsets.....	75
Table 3-7 Correlation parameters used for the compression test on the cylindrical epoxy coupon .....	78
Table 3-8: Amount of particle within a 128x128x128 subset.....	82
Table 3-9: Standard Deviation of the distance between the centroid of the seeding particle and center of the subset.....	84
Table 3-10: Zero Normalized cross-correlation coefficients for 128x128x128 voxel displaced by 35 $\mu\text{m}$ .....	85
Table 3-11: Amount of particle within a 32 x 32 x 32 voxel correlation window .....	87
Table 4-1: Manufacturing parameters for slicer software utilized to produced tensile coupon .	110
Table 4-2: List of scan parameters utilized to image the tensile coupon.....	112
Table 4-3: Image processing parameters used to define the cross-sectional area of 100 N and 200 N datasets .....	117

Table 4-4: Image processing parameters used to define the cross-sectional area of 150 N datasets .....	118
Table 4-5: Image processing parameters to segment out sample air gaps for 100 N, 150 N and 200 N dataset.....	121
Table 4-6: Digital volume correlation input parameters for displacement and strain measurements of copper-PLA sample .....	125
Table 4-7: Statistical analysis of the cross-section area for different load conditions.....	129
Table 4-8: Air gap volume and actual sample infill density measured for a 3 mm section through $\mu$ -CT .....	130

## vii List of Figures

Figure 2-1: Diagram of the three types of reinforcements for composites: a) Continuous and short fibers, b) Particulate, and c) Flakes.....	10
Figure 2-2: Cross-Section of a stacked fibre laminate with layers stacked at: $0^\circ$ , $45^\circ$ , and $90^\circ$ ....	14
Figure 2-3: Schematics of types of 2D diamond braids: a) biaxial braid, & b) Triaxial braid .....	15
Figure 2-4: Schematic drawings of the three most common braided composite patterns: a) Diamond (1/1), b) Regular (2/2), and c) Hercules (3/3) .....	16
Figure 2-5: Interlaced structure and braid angle of 2D tubular braided composite shown on a true carbon fibre preform with a diamond unit cell. ....	17
Figure 2-6: Schematic of a diamond braid that has gone from the state a) unjammed to b) jammed.....	18
Figure 2-7 Braid coverage for a) closed mesh braid and b) open mesh braid. ....	18
Figure 2-8: Example Schematic of a 2D DIC for a sample under mechanical loading.....	24
Figure 2-9: Example of a speckled test sample for DIC and representative correlation window	25
Figure 2-9: Example of a speckled test sample for DIC and representative correlation window	26
Figure 2-10: Schematic drawing showing the layout and operation of a $\mu$ -CT machine during the scanning of sample material.....	32
Figure 2-11: Composite architecture (Tow, voids, and matrix) of a reconstructed cross-section of a tubular braided composite with an 11.1 inner diameter (ID) produced from $\mu$ -CT.....	35
Figure 2-12: Depiction of displaced DVC sub-volume where reference particle U and W displace to from the reference state f to deformed state g' where they are shown as U' and W' respectively. ....	38

Figure 3-1: Test epoxy sample for DVC analysis: (a) Final cured sample of the epoxy-copper sample, (b) Epoxy sample within the material test stage. The material test stage is placed within the  $\mu$ -CT scanner for in-situ mechanical testing ..... 68

Figure 3-2: Example images from CT scan of copper impregnated epoxy sample: a) X-ray shadow projection showing the sample with central hole and b) reconstructed cross-section across the A-A plane (contrast-enhanced where the copper particles and epoxy can be seen) .... 70

Figure 3-3: 3D Model of the copper impregnated sample: a) Geometrical solid model showing the coordinate planes: i) XY plane, ii) XY plane, & iii) YZ plane, and b) 3D reconstruction of the sample geometry from  $\mu$ -CT tomographs..... 78

Figure 3-4: Comparison of the greyscale histogram and sample CT Slice: a) 200  $\mu$ m copper, b) 50  $\mu$ m copper, c) 25  $\mu$ m copper, d) 10  $\mu$ m aluminum nitride, and e) 50  $\mu$ m zirconium (IV) oxide ..... 80

Figure 3-5: 2D representation of the two cases of particle distribution throughout the sample: a) agglomeration of particles within a region, and b) random distribution of particle ..... 81

Figure 3-6: Histogram of amount of particles at different distances from correlation window centroid: a) 200  $\mu$ m copper sample, b) 50  $\mu$ m copper sample, c) 25  $\mu$ m copper sample, and d) 50  $\mu$ m zirconium (IV) sample ..... 83

Figure 3-7: Percentage error produced from DVC calculation compared against three standard subset sizes..... 87

Figure 3-8: Effect of percentage overlap of subsets on overall accuracy ..... 88

Figure 3-9: Error produced as a result of down sampling numerically displaced data: a) full resolution dataset, b) 1/3 reduced resolution dataset ..... 90

Figure 3-10: Views of displacement of the sample along the direction of compression: a) isometric view, b) yz plane, and c) xy plane.....	92
Figure 3-11: Views of displacement of the full resolution sample along the direction of compression: a) isometric view, b) yz-plane, and c) xy-plane .....	93
Figure 3-12: Equivalent Von Mises strain for the down-sampled epoxy sample subjected to compressive loading: a) Isometric View b) yz-plane and c) xy-plane.....	95
Figure 3-13: Equivalent Von Mises strain for the down-sampled epoxy sample subjected to compressive loading with edge effect removed: a) Isometric View b) yz-plane and c) xy-plane	96
Figure 3-14: Equivalent Von Mises strain for the full-resolution epoxy sample subjected to compressive loading: a) Isometric View, b) yz-plane, c) xy-plane view and d) strain across y-axis and z-axis of hole .....	97
Figure 4-1: Cross-section sketch of the tensile couple: a) ASTM D638-14 type V b) modified design to fit in MTS .....	110
Figure 4-2: Representation of the tensile coupons printing scheme: a) nozzle path, b) slicer view of the center layer of coupon .....	111
Figure 4-3: Model render of the MTS loaded with tensile coupon.....	111
Figure 4-4: Shadow projections of the copper PLA sample for a) 100 N, b) 150 N, and c) 200 N loads .....	113
Figure 4-5: Reconstructed cross-section of copper PLA sample with enhanced contrast.....	115
Figure 4-6: Segmentation of copper PLA sample cross-section: a) $\mu$ -CT image, and b) filled sample cross-section .....	117
Figure 4-7: Schematic showing original reconstruction plane from micro-CT, and resliced plane .....	120

Figure 4-8: Pores identification steps for copper PLA sample: a)  $\mu$ -CT image, b) filtered and despeckled, c) large despeckled and closed, d) inversed image highlighting air gaps ..... 122

Figure 4-9: Illustration of DVC discretization process of sample into individual speckled subset. .... 123

Figure 4-10:  $\mu$ -CT data for 128 voxel correlation window size: a) single  $\mu$ -CT slice from correlation window, b) resultant greyscale histogram for correlation window ..... 127

Figure 4-11: Variation of cross-section area through 3mm section of the sample: a) cross-section area variation through 3mm gauge length of the sample, b) percentage change of cross-section area compared to 100 N load ..... 128

Figure 4-12: Displacement in direction (z-axis) of tensile load: a) isometric view of displacement for 100-150 N test, b) XZ plane displacement for 100-150 N test, c) isometric view of displacement 100-200 N test, d) XZ plane view of displacement for 100-200 N test..... 132

Figure 4-13: Volumetric strain  $\epsilon_{xx}$  developed through the sample: a) isometric view of 100 to 150 N test, b) XZ plane view of 100 to 150 N test, c) isometric view of 100 to 200 N test, d) XZ plane view of 100 to 200 N test, d) strain profile across the sample width. .... 135

Figure 4-14: Volumetric  $\epsilon_{yy}$  developed through the sample: a) isometric view of 100 to 150 N test, b) XZ plane view of 100 to 150 N test, c) isometric view of 100 to 200 N test, d) XZ plane view of 100 to 200 N test, d) strain profile across the sample width. .... 136

Figure 4-15: Volumetric strain  $\epsilon_{zz}$  developed through the sample: a) isometric view of 100 to 150 N test, b) XZ plane view of 100 to 150 N test, c) isometric view of 100 to 200 N test, d) XZ plane view of 100 to 200 N test, d) strain profile across the sample width. .... 139

## viii List of Abbreviations

2D	Two Dimensional
2D DIC	2D Digital Image Correlation
3D	Three Dimensional
3D DIC	3D Digital Image Correlation
AM	Additive Manufacturing
CAD	Computer Aided Design
CC	Cross Correlation
CMC	Ceramic Matrix Composite
DVC	Digital Volume Correlation
FEA	Finite Element Analysis
FFF	Fused Filament Fabrication
FIDVC	Fast-Iterative Digital Volume Correlation
MMC	Metal Matrix Composite
NCC	Normalized Cross Correlation
PLA	Polylactic Acid
PMC	Polymer Matrix Composite
ZNCC	Zero Normalized Cross Correlation
$\mu$ -CT	Micro-Computed Tomography



## ix List of Variables

$d$	Diameter
$E$	Youngs Modulus
$f(x_i, y_j)$	reference image greyscale intensity
$F(x_i, y_i, z_k)$	reference volume greyscale intensity
$f_m$	reference image mean greyscale intensity
$F_m$	reference volume mean greyscale intensity
$g(x_i, y_j)$	deformed image greyscale intensity
$G(x_i, y_j, z_k)$	deformed volume greyscale intensity
$g_m$	deformed image mean greyscale intensity
$G_m$	deformed volume mean greyscale intensity
$L$	length
$\varepsilon$	plain strain
$\rho$	Density
$\sigma_{ult}$	ultimate strength
$\tau$	shear strain

# Chapter 1: Introduction

## 1.1 Motivation

With the increasing industry demand for lightweight and high-performance materials, composites have found increased industrial adoption in recent years. According to global forecasts, the market for these materials is expected to reach a size of USD 160.54 billion by 2027[1]. This industry growth is due to manufactures preferring these material to traditional ones for their lightweight, high strength, and material tailorability [2], [3]. A further advantage comes from the wide variety of manufacturing techniques and structures, which provided differing materials and logistical benefits. The most common type of composites are laminates, which are formed by sheets of fibres stacked and impregnated with a matrix material that provides their high strength to weight ratio [2], [4]. Another example are braids which are formed by interlaced fibres which are impregnated into the matrix. Manufacturing through braiding rather than in a stacked laminate structure, provide thru-thickness strength for applications that require this property, such as in aircraft fan structures [5], [6]. The final structure discussed in this thesis are one that have been produced with additive manufacturing (AM) design principles, the most popular of which is fused filament fabrication (FFF). This process combines the material advantages of composites with the quick to-form manufacturing methods of AM[7], [8].

Composite materials and FFF parts contain complex heterogenous micro-structures. The complex microstructures of composites and FFF parts lead to anisotropic material properties. For composite materials, this is due to their multi-material composition, fibre alignment, and interfacial bonding between phases [3]. Additionally, a further layer of complexity is seen in textile and woven composites due to the shifting of fibre tows, which alter the material parameters during loading conditions [3], [9]. For parts produced via FFF beyond the bonding of the reinforcing

material to the base material, regions of high localized porosity and imperfect layer bonding lead to their anisotropic material properties [10], [11].

With the expected growth of the composites and additive manufacturing industries, it has become essential for accurate and detailed quantification of their material properties and behaviour during loading. Traditional methods such as extensometers and strain gauges provide insufficient and inaccurate details about the behaviour of these complex materials as they can only capture the generalized movement in the region they are applied. Digital image correlation (DIC) can circumvent this issue by providing a full field-view of the displacement and strain behaviour on the surface of the materials [12]. However, the 2D DIC method is inherently limited to only an in-plane view of mechanical response as external images are captured using high-resolution digital cameras. 3D DIC utilizes a camera set in a stereo configuration allows for out-of-plane as well as in-plane movement to be captured. However, the 3D DIC method is still limited in its inability to capture thru-thickness deformation. If interactions within the sample and its internal microstructure are to be captured, a new method must be utilized.

With the recent advent of micro-computed tomography ( $\mu$ -CT), a third option has become available for experimental strain analysis [13].  $\mu$ -CT allows for high-resolution images of a material microstructure to be captured volumetrically. By subsequently capturing the microstructure during different loading conditions, the volumetric response of the material can be analyzed. This data can then be utilized as an input for a correlation algorithm known as digital volume correlation (DVC) [14]. DVC addresses the concerns of DIC by providing a full-field volumetric view of the sample's displacement and strain. Measurements are made in this manner to provide a complete view of the sample's mechanical behaviour while helping to provide direct inputs for numerical models.

## **1.2 Thesis Objective**

This thesis utilizes the new DVC approach for strain measurements of complex materials. The overall objective of this thesis was to utilize DVC to capture the deformation and strain behaviour of advanced materials such as FFF composites and tubular braided composites. Since DVC is an emerging technology, the supporting literature is limited. Thus, before the analysis of advanced materials can be performed accurately, an investigation on sample preparation for analysis is a vital initial step. For this requirement, a study on the implementation of artificial speckling methodologies to improve image quality for composite materials was undertaken. By providing a complete assessment of the advantages and errors of the artificial speckling technique, a methodology could be developed to allow for advanced materials to be analyzed accurately via DVC. The creation of these best practices allowed for the ultimate goal of volumetric advanced material analysis. Thus, the methodology was applied to an FFF composite to capture its mechanical response to tensile loading conditions. The application of the speckling methodology gained from the material test of FFF composites will ultimately allow for better DVC technique and material knowledge to had, which can be applied in the future to other materials such as tubular braided composites.

## **1.3 Thesis Scope**

As DVC software in the early phases of development, commercially available software are few and are prohibitively expensive. Additionally, development of a DVC algorithm can prove time-consuming and would be the subject matter of a standalone project. Thus, it was determined that the best option was through the utilization of open-source DVC software. This thesis utilizes a MATLAB based open-source DVC software known as the fast-iterative digital volume correlation algorithm (FIDVC)[15]. To further the objective of developing a methodology for

preparing composite samples for DVC measurement studies were limited to 5 different high-density particles consisting of copper, zirconium oxide, and aluminum nitride impregnated into an epoxy resin. Once sample speckling was understood, this methodology could be applied towards FFF printed tensile coupons containing seeding particles for accurate DVC analysis.

#### **1.4 Thesis outline**

This thesis is organized into five chapters. As a starting point of discussion, Chapter 2 discusses the current state of research on the topics addressed in this thesis. Chapter 2 is divided into three major topics: fundamentals of composite and AM structures, concepts and applications of DIC, and concepts and application of  $\mu$ -CT and DVC. This chapter highlights current gaps in the literature to help establish the motivation for the remaining chapters.

A discussion on the development and implementation of the artificial seeding to enhance the image quality of composites for DVC is detailed in Chapter 3. A full error analysis of the effects of each particle in relation to resulting DVC sample displacement is outlined to determine the most optimal seeding particle. Additionally, this error analysis aided in the determination of DVC parameters that provided the highest accuracy. This chapter finally shows the application of this technique by seeding an epoxy resin with a center hole to analyze the stress and strain behaviour during uniaxial compression.

Chapter 4 utilizes the findings of the previous chapter to provide a full-scale study on FFF materials. FFF composites manufactured from PLA impregnated with copper particles crafted in the form of tensile coupons. Samples were tested in-situ under tensile loading to obtain images of the microstructure under deformation. These images could be analyzed to help understand the bulk changes in the microstructure before being used as an input for DVC. The DVC measurements

allowed for detail full-field 3D displacement and strain results to be calculated and related to the printing parameters which formed the coupon.

A complete summary of the results of this thesis and their implication towards future work is detailed in Chapter 5. This section highlights the critical finding of the artificial seeding technique and the results of the mechanical tests and measurements performed on the copper impregnated PLA FFF samples. A section providing the author's recommendations for performing successful DVC measurements is also included in Chapter 5. The focus of this subsection is to transfer the experimental knowledge gained throughout the author's thesis work to help future researchers perform accurate DVC measurements. Finally, the potential research areas that can be investigated with the aid of the knowledge from this study are provided. The underlying formulation and methodologies for the utilized image segmentation procedures are detail in Appendix A. Appendix B provides the MATLAB software code developed for analysis is these studies along with an explanation of their functionality.

## **1.5 References**

- [1] GWR, "Composites Market Size, Share & Trends Analysis Report by Product (Carbon, Glass), by Resin (Thermosetting, Thermoplastics), by Manufacturing Process, by End Use, and Segment Forecasts, 2020 - 2027e." Grand View Research, 2020.
- [2] I. Daniels and O. Isahi, *Engineering Mechanics of Composite Materials*, Second Edi. New York: Oxford University Press, Inc, 2006.
- [3] A. K. Kaw, *Mechanics of composite materials, second edition*. 2005.
- [4] A. R. A. Hani, M. Mariatti, A. Roslan, R. M. Nazrul, and A. R. Othman, "Influence of woven and cross-ply laminates on mechanical properties of coir epoxy composite," in

- Applied Mechanics and Materials*, 2013, pp. 136–140.
- [5] J. P. Carey, “Introduction to braided composites,” *Handbook of Advances in Braided Composite Materials: Theory, Production, Testing and Applications*, 2016.
- [6] D. Zhang, X. Zheng, Z. Wang, T. Wu, and A. Sohail, “Effects of braiding architectures on damage resistance and damage tolerance behaviors of 3D braided composites,” *Compos. Struct.*, vol. 232, 2020.
- [7] P. S. Ujeniya and N. V. Rachchh, “A review on Manufacturing, Machining, and recycling of 3D printed composite materials,” *IOP Conf. Ser. Mater. Sci. Eng.*, vol. 653, no. 1, 2019.
- [8] S. Hwang, E. I. Reyes, K. sik Moon, R. C. Rumpf, and N. S. Kim, “Thermo-mechanical Characterization of Metal/Polymer Composite Filaments and Printing Parameter Study for Fused Deposition Modeling in the 3D Printing Process,” *J. Electron. Mater.*, vol. 44, no. 3, pp. 771–777, 2015.
- [9] J. P. Carey, G. W. Melenka, A. J. Hunt, and C. Ayranci, “Introduction to braided composite material behavior,” in *Handbook of Advances in Braided Composite Materials: Theory, Production, Testing and Applications*, 2017, pp. 207–237.
- [10] R. J. Zaldivar, D. B. Witkin, T. McLouth, D. N. Patel, K. Schmitt, and J. P. Nokes, “Influence of processing and orientation print effects on the mechanical and thermal behavior of 3D-Printed ULTEM ® 9085 Material,” *Addit. Manuf.*, vol. 13, pp. 71–80, 2017.
- [11] B. Wang, L. Sun, and B. Pan, “Mapping internal deformation fields in 3D printed porous

- structure with digital volume correlation,” *Polym. Test.*, vol. 78, 2019.
- [12] G. W. Melenka and C. Ayranci, “Advanced measurement techniques for braided composite structures: A review of current and upcoming trends,” *Journal of Composite Materials*. 2020.
- [13] S. K. Boyd, “Micro-computed tomography,” in *Advanced Imaging in Biology and Medicine: Technology, Software Environments, Applications*, 2009, pp. 3–25.
- [14] B. K. Bay, T. S. Smith, D. P. Fyhrie, and M. Saad, “Digital volume correlation: Three-dimensional strain mapping using x-ray tomography,” *Exp. Mech.*, vol. 39, no. 3, pp. 217–226, 1999.
- [15] E. Bar-Kochba, J. Toyjanova, E. Andrews, K. S. Kim, and C. Franck, “A Fast Iterative Digital Volume Correlation Algorithm for Large Deformations,” *Exp. Mech.*, vol. 55, no. 1, pp. 261–274, 2015.



## Chapter 2: Literature Review

### 2.1 Introduction

As discussed in the introductory chapter of this thesis the ultimate goal of this work is to develop a methodology from data collection to analysis of strain fields for composites, braided composites, and 3D printed structure via digital volume correlation (DVC). Before discussing the work done to meet this goal, it is necessary to provide a point of reference to the topics discussed in this work. The purpose of this section is to provide a comprehensive review of the literature and the gaps that surround the work currently done in the three major areas of this thesis. In this section, a formal review of the terminology, fundamental principle, and current literature surrounding composites, image acquisition, and image analysis will be provided.

Composites provide a technical advancement over traditional materials such as metals, due to their high strength-to-weight ratio, and tailorability. This makes them particularly desirable in many high-performance industries, such as aerospace. The first section of this chapter will aim to introduce the field of composite materials. A discussion is first made on the fundamentals of composite materials and their classification. Then a more in-depth review of the structure, advantage, and disadvantage of composite laminates, braided composites, and fused-deposited modelling produced composites is presented.

The next section presented is on 2D image analysis and its application towards composite studies. While, have many mechanical advantages over traditional materials, due to their heterogeneous structure, traditional mechanical property measurement technique such as strain gauges are ineffective. A particularly elegant solution to this challenge is provided through the usage of digital image correlation (DIC). Digital image correlation allows for a full-field view of

strain and deformation to be captured rather than a single isolated point making it very useful for capturing the mechanical response of heterogeneous materials. In this section, the guiding principles of DIC, and its application in composite materials by researchers is provided.

The final topic discussed is on the operating principles and application of the relatively new DVC. DVC extends the principles of DIC into the third dimension. DVC addresses the limitations of DIC by allowing for volumetric displacement and strain fields to be captured through the bulk of the sample rather than simply surface strains. This section looks to capture how the image acquisition is performed for DVC through micro-computed tomography. Next, the operating principles of DVC are discussed, before finally, discussing the current applications of DVC for material behaviour measurements.

## **2.2 Composites**

### **2.2.1 Fundamentals of Composites**

Traditional composites are a multiphase material consisting of two or more materials that are bonded macroscopically. These materials fall into one of two phases, the first being the matrix phase, which is continuous and forms the bulk of the material [1]. The second phase, the reinforced phase, is supported by the matrix phase and is typically has a fibrous (continuous or short), particulate or flake structure. A 2D representation of a cross-section of a matrix that is supported by these three phases is shown in Figure 2-1. The macroscopic bonding of these phases provides a material with unique and enhanced mechanical properties. Examples of conventional composites materials are resin-infused carbon fibres and steel-reinforced concrete.

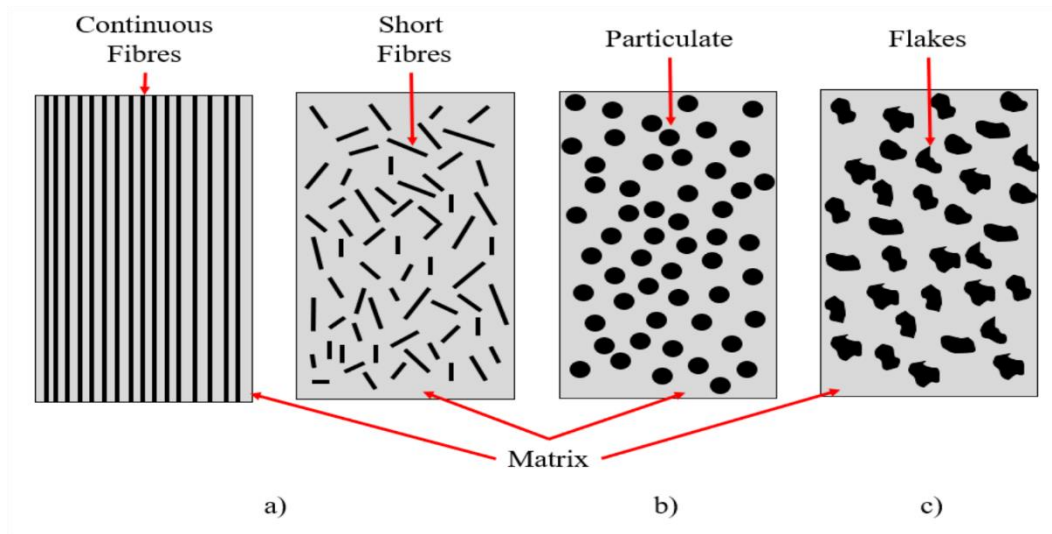


Figure 2-1: Diagram of the three types of reinforcements for composites: a) Continuous and short fibers, b) Particulate, and c) Flakes

High-performance composites have begun to replace traditional materials across several different industries. A few examples of the broad where composites are utilized include use in aircraft fuselages, golf clubs, and bone casts [2]–[4]. The reason for this lies in the mechanical advantage of the material. The mechanical advantage is calculated through the specific modulus and specific strength, which are shown in equations 2.1 and 2.2. Specific modulus is calculated by the ratio of the Young’s modulus ( $E$ ) and the density ( $\rho$ ), while the specific strength is calculated by taking the ultimate strength ( $\sigma_{ult}$ ) and density. For composite materials, both these factors are equivalent to many times higher than traditional engineering materials such as steel. Thus, composites offer a high-performance alternative to traditional materials at a fraction of the weight, which results in less material and energy consumption, additionally, the versatility of the materials that allow them to be tailored to tackle specific design problems.

$$\text{Specific Modulus} = \frac{E}{\rho} \quad (2.1)$$

$$\text{Specific Strength} = \frac{\sigma_{\text{ult}}}{\rho} \quad (2.2)$$

### 2.2.2 Composite Classification

Composites are classified by either the structure of the reinforcement phase or material of the matrix phase. As previously mentioned, there are three types of structures for the reinforcement phase: fibres, particulates and flakes. Their large aspect ratio characterizes fibres compared to the other reinforcement types. The aspect ratio is calculated as the ratio between length (L) and diameter (d), as shown in equation 2.3. Fibres are further classified into short (discontinuous) or long (continuous) fibres based on their aspect ratio. Depending on the degree of alignment, the fibre-reinforced composites can have quasi-isotropic properties for randomly distributed fibres to highly anisotropic properties when aligned [5]. Particulate composites are consisting of small particles that are randomly dispersed and suspended inside the composite matrix. Due to the random dispersion of particles, most particulate composites have isotropic mechanical properties. Finally, flake composites contain a reinforcement phase of flat pieces that are unique because they provide high out-of-plane flexural stiffness.

$$\text{Aspect Ratio} = \frac{L}{d} \quad (2.3)$$

Composites classified by their matrix phase are often put into four categories: 1) polymer matrix composites (PMC), metal matrix composites (MMC), ceramic matrix composites (CMC), and carbon matrix composites. The most common of these is the PMC, which consisted of a resin matrix (e.g. epoxy) with a reinforcement phase [6]. The adoption of PMC in favor of other alternatives is due to their low cost and high strength to weight ratio. However, PMCs are not feasible for use at high operating temperatures due to the degradation of the polymer matrix.

Additionally, the low elastic properties make them unsuitable for loading conditions that require more rigidity.

MMCs have matrix phases that are typically, but not exclusively made from aluminum, magnesium, and titanium. The main advantage of MMC compared to traditional materials is the tailorability of their mechanical properties. For example, a designer can increase the mechanical, while decreasing the thermal expansion. MMCs provide superior mechanical properties to PMC but require much higher processing temperature. Additionally, MMCs are significantly denser than PMCs due to their metal matrix. CMC, as their name suggests, are composites with a ceramic matrix material. CMC offers very high strength, hardness, service temperature and low density, but are susceptible to fracturing under impact or tension through the reinforcement phase does improve these over regular ceramics. Carbon matrix composites, also known as Carbon-Carbon composites, have a carbon matrix that has been reinforced by carbon fibres. Carbon-Carbon composites have high operating temperature ranging, high tensile and compressive strengths and thermal conductivity, but are very costly, have a low shear strength and may oxidate at very high temperatures.

### **2.2.3 Laminate Composites**

In addition to classifying the matrix material and reinforcement phase of a composite, one must define the type of composite [6]. There are several different types of composite, each with their unique properties and distinct advantage and disadvantages. The most commonly used type of composite material is laminate.

The fundamental unit of composite laminates is the lamina. A lamina is a single sheet of either unidirectional or woven fibres that have been embedded into a matrix material. A single lamina is an orthotropic material that is used to build up the individual layers of the laminate. Though

individually, each lamina may have unidirectional fibres, a laminate need not have each ply in alignment, as seen in Figure 2-2. The laminate plies may be perfectly aligned or completely offset to improve mechanical properties in a specific plane or to increase the anisotropy of the material. Though it is most common for each ply in a laminate to consist of the same matrix and reinforcement, it can be advantageous to use different reinforcement material in each layer and occasional in the same layer. Composites with different materials in each layer are known as intra-ply hybrid composites, and ones with various materials in each ply are known as inter-ply composites.

The advantages of laminate lie in their high strength, lightweight, and the tailorability of their material properties [7]. Laminates particularly have high in-plane strength in the direction of their fibres compared to other composite materials [8]. However, there are two significant disadvantages of laminates: their through-thickness strength and damage resistance. The low through-thickness strength is due to no interlayer connectivity between fibres [9]. Indeed, this means that the laminates are particularly weak between laminae. The low damage resistance is also a result of the lack of interlayer connectivity, which makes laminates extremely susceptible to both formation and subsequent propagation of cracks in the laminate layers [10]. This process of crack formation and fracturing along layers is known as delamination.

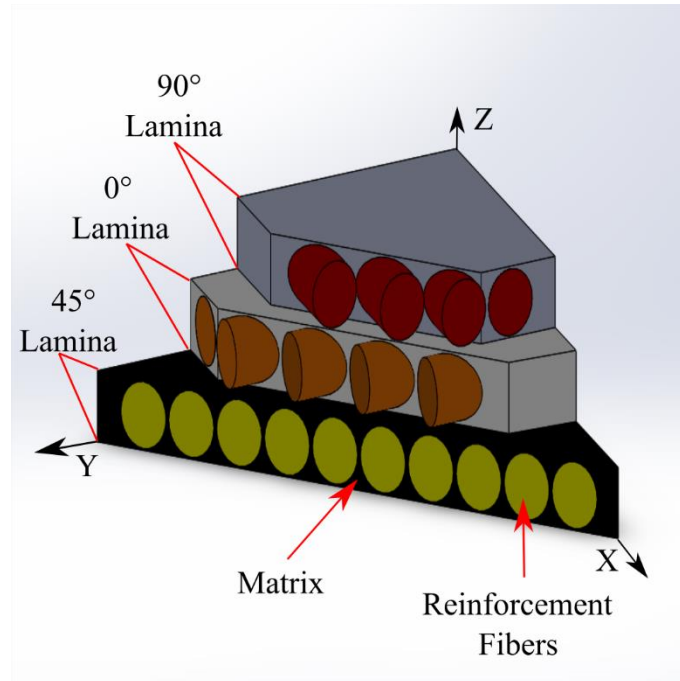


Figure 2-2: Cross-Section of a stacked fibre laminate with layers stacked at:  $0^\circ$ ,  $45^\circ$ , and  $90^\circ$ .

#### 2.2.4 Braided Composites

Braided composites are interwoven composite material that typically consists of two phases: fibres and matrix material. The fibres are elongated elements that are high in strength and light in weight. Braided composites are formed by entwining fibre bundles or yarns at a specific braid angle along the principal axis leading to the name angle-ply composites [9]. The weaving of these braids provides thru-thickness reinforcement and enhanced damage resistance to impacts when compared with traditional laminates [9], [11]. While theoretically, any range of angles can be produced, practically angles are restricted to a range of  $20^\circ$  to  $70^\circ$  [12]. The reason for this is that braids with angles below  $20^\circ$  have insufficient fibre locking and above  $70^\circ$  display extreme fibre damage. This distinguishes them from woven composites which feature orthogonal yarns [4]. The second part, the matrix or resin, adheres to the fibres together while protecting them from external damages [1]. Impregnation of the resin can be performed either before the yarns are weaved

together or after the braid structure is formed. The most commonly used matrix materials are thermoset or thermoplastic polymer [1].

Typically, braided composites are classified as either two-dimensional (2D) or three-dimensional braids (3D). 2D braids, which will be the focus of this study, are characterized by having yarns that are entwined only in a single plane. 2D braided composites can be distinguished by braid type or braid pattern. There are two types of 2D braids: biaxial and triaxial braids [9], [13]. Biaxial braids are distinguished by a two-yarn bias system woven at a chosen angle [13]. Triaxial braids are produced on a three-yarn bias system where the third yarns lay at 0 degrees. Figure 2-3 a) shows a pictorial representation of a biaxial braid. A triaxial braid is shown in Figure 2-3 b) and is easily distinguishable from a biaxial due to the presence of yarns in the direction of the principal axis. Generally speaking, 2D braided composites come in three patterns, each defined by the yarn overlapping: diamond (1/1), regular (2/2), and Hercules (3/3) [9]. The overlapping braid pattern can be seen in Figure 2-4, which shows a unit for each braid pattern.

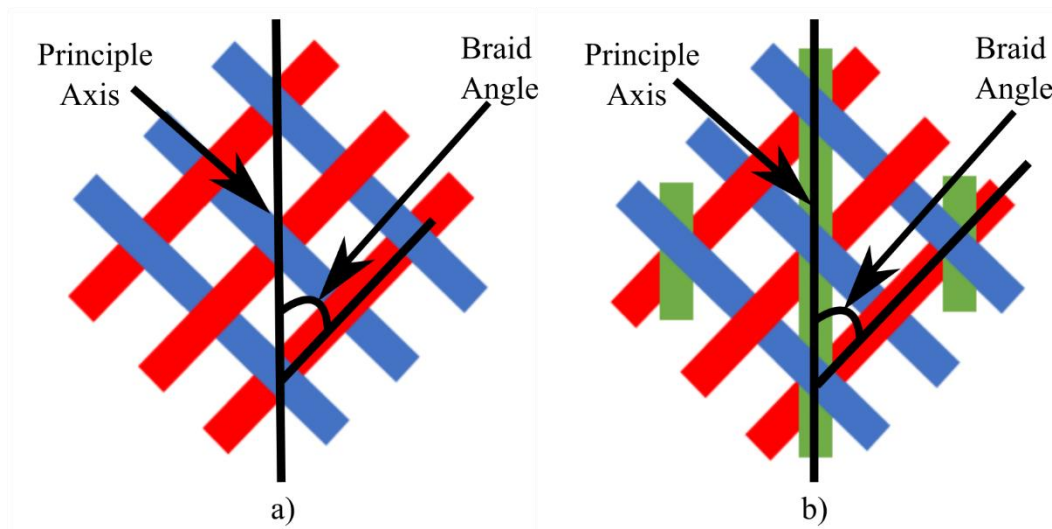


Figure 2-3: Schematics of types of 2D diamond braids: a) biaxial braid, & b) Triaxial braid



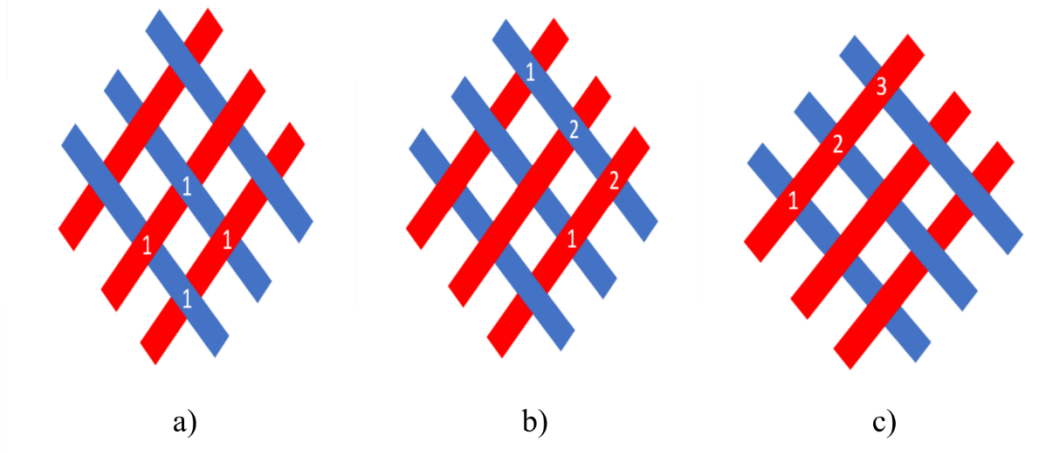


Figure 2-4: Schematic drawings of the three most common braided composite patterns: a) Diamond (1/1), b) Regular (2/2), and c) Hercules (3/3)

The geometry and interlaced structure, which is seen in Figure 2-5, are the primary contributors to the superior properties of braids over traditional laminate composites. There are three key factors geometric components that affect the braided composite strength: the braid pattern, the braid angle, and the mesh spacing. The most important feature is the braid angle, which is the angle the yarns make with the principle axis [1]. Alterations to the braid angle of the braided composite can change the composite's mechanical properties [1]. Generally, the more aligned the yarns are, the stronger the braid will perform under longitudinal loading and, worse under transverse loading, while at  $45^\circ$ , the material is most durable in shear [4]. However, there is a limit to the range of braid angles achievable, known as the jam angle, where adjacent yarns interfere with one another to preventing further shifts in the braid angle. The tendency of the braid angle to shift during loading resulting in a subsequent change in mechanical properties in addition to possible jamming of the braid makes their mechanical properties very difficult to predict. Figure 2-6 shows a braid in an unjammed state compared to that of a braid in a jammed state. It is easily seen that in Figure 2-6 a), the yarns have space to shift when a force is applied, while in Figure

2-6 b) that yarns are in a position such that further movement is not possible. Finally, braids can have an open or closed mesh; the difference between them is easily identifiable and can be seen in Figure 2-7. Open meshed braids, typically have a low fibre volume percentage, perform better in torsion, and have lower flexural rigidity than closed mesh braids [14]–[16].

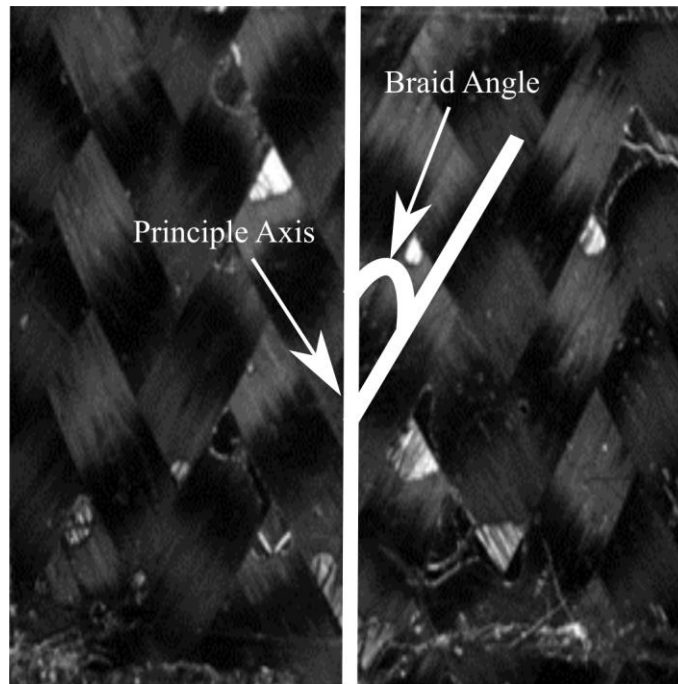


Figure 2-5: Interlaced structure and braid angle of 2D tubular braided composite shown on a true carbon fibre preform with a diamond unit cell.

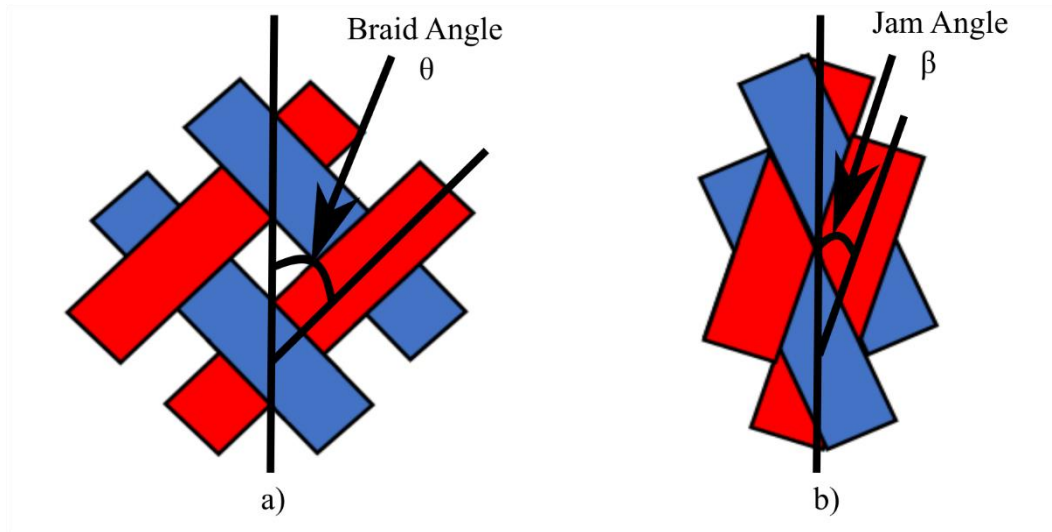


Figure 2-6: Schematic of a diamond braid that has gone from the state a) unjammed to b) jammed.

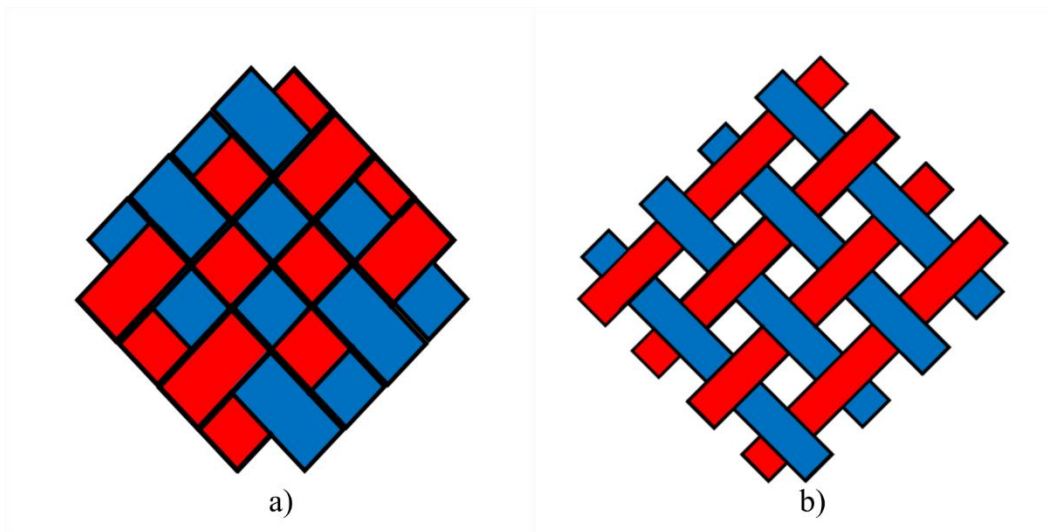


Figure 2-7 Braid coverage for a) closed mesh braid and b) open mesh braid.

### 2.2.5 Injection Moulding Composites

Conventional composites require a complicated manufacturing procedure and can be time-consuming to produce. This has led researchers to investigate methods for crafting composites with a quick production cycle and can be easily implemented into industrial mass production [17]. The following sections will provide an overview of two of the most researched methods for achieving expedited near-net shape composite production. The first procedure discussed is on the

working principles of composite injection molding. The proceeding section will discuss composites produced through additive manufacturing principles.

The injection molding procedure is utilized primarily for the production of PMC [18]. However, it is not solely limited to the fabrication of PMCs as MMCs, and Carbon-Carbon composites are possible to produce via the injection molding procedure [17]. While the end product's constituent materials may differ, generally speaking, the production cycle employs the same general principles. Thus, as PMCs are the most commonly produced composite through injection molding and of particular interest for the work outlined in this thesis, this section will delve into these materials' production cycle.

The first step in fabricating PMCs is to create a feedstock material typically in the form of composite pellets. The feedstock for PMC is generally produced by compounding a thermoplastic resin with reinforcing fibres or particulates. A twin-screw extruder is then utilized to mix the polymer resin and reinforcement phase. Twin Extruders are generally preferred over single screw extruders due to their high throughput and more thorough mixing [18]. Typically, the mixed compound has a reinforcement content of 20-50 wt%. The composite's pellets fabricated from the extruder are then utilized as the injection molding process's input material.

The composite pellets are first loaded into the injection molding machine's hopper, which feeds them into the barrel. A single screw transports the reinforced polymer through the barrel into the mold [18]. As the screw transports the polymeric material, heat generates through the screws shearing motion melt and plasticizes the polymer along with the help of auxiliary heaters'. The reciprocal action of the screw builds up the molten polymer until it is ready to be injected into the mold cavity. To force the polymer into the chamber and account for shrinkage, an external device holds the screw under pressure forcing the polymer mixture into the mold cavity and holding the

part under pressure [17]. The part is then cooled via an external cooling unit's help until it typically reaches a temperature below its glass transition point. The final piece is then ejected from the mold cavity.

While the fast production cycles, near net-shape design, and ease of implementation within mass-manufacturing production, are advantages of the injection molding procedure, there are still some limitations. The first limitation is the amount of filler content that is possible to compound with the polymer. Large amounts of filler result in correspondingly high viscosity, which cannot be transported through the machine [19]. Additionally, the flow fields created in the barrel result in the alignment of the reinforcement phase, making random orientation fibre-reinforced composite difficult to produce [18], [20]. Consequently, this fibre alignment results in material properties that tend to be highly anisotropic, with superior strength in the fibre alignment direction. The development of more complex injection molding machines, such as fluid-assisted injection molding composites, has allowed for the production of more randomly oriented fibre composites [18]. Finally, continuous or long fibre composites are challenging to produce utilizing the traditional injection molding process as the fibres tend to break during the plasticization process [18].

### ***2.2.6 Fused Filament Fabrication (FFF) Composites***

Conventional composites require a complicated manufacturing procedure and can be time-consuming to produce. The advent of additive manufacturing has allowed for the automated production of complex composite structures. Additive manufacturing has made it possible to create to-scale composite parts directly from solid models. One of the most common additive manufacturing methods for producing scale parts is fused filament fabrication (FFF) [21]. Fused

deposit modelling heating material beyond its melting temperature and deposits it upon working bed. This process builds the material layer by layer until the full geometry of the part is realized.

FFF is one of the most commonly utilized additive manufacturing methods due to the vast array of thermoplastics compatible with the procedure and ease of implementation into manufacturing production lines [22]. However, traditional FFF parts are typically only seen in the production of prototypes or simple toys [23]. The reason that FFF parts see limited commercial usage is due to the low mechanical properties of resin material and inconsistent part production from the FFF printers [22]. To improve upon the mechanical strength of FFF parts, researchers have begun to incorporate reinforcing materials, such as graphite, carbon fibre, or metal particles [22], [24]. The addition of this reinforcing phase helps to address this issue by improving mechanical strength to allow for use in functional design parts.

As with all composite material, FFF composites can be manufactured as continuous fiber, short fiber, or particulate based composite materials [25]–[27]. For this literature review, the focus will be placed on particulate FFF composites. Particulate-reinforced composite material offers a low-cost alternative to fibre-reinforced FFF composites [25]. The addition of particles to thermoplastic matrix material offers a vast degree of tailorability and improvements to tensile strength, wear-resistance and dielectric permittivity [25], [28].

When considering particle-reinforced composites, there are many factors, including particle loading, particle size, particle loading, surface treatment, and interfacial adhesion, that can have a significant effect on the mechanical properties of the composite material [25]. Of these factors, particle size, particle adhesion and particle loading all play an essential role in the strength of the materials. It is often challenging to separate the role of these three factors due to their interplay in determining the overall mechanical behaviour [29].

While the speed of production and increased mechanical properties of FFF-composites make them an attractive alternative to traditional materials, there are still many challenges with regards to FFF composites. One of the most glaring challenges when it comes to the analysis of FFF composite is the characterization of their mechanical properties. Due to the previously described interplay between particle size, particle loading, and adhesion, the mechanical properties are often difficult to predict and are not always linear. An example of such can be seen in Hwang et al. where the effects of fill density increase the tensile stress of the material, but had no significant effects on strain other than the 60% infill samples which showed increased ductility [24]. Additionally, not all particles and particle loading conditions are easily achievable. The addition of a high amount of dense filler material can cause a significant increase in viscosity of the filament, making the FFF procedure impossible to achieve without the addition of plasticizers [30].

## ***2.3 Digital Image Correlation***

### ***2.3.1 Image Acquisition for Surface Measurements***

To realize the mechanical properties of complex material, researchers have moved from traditional point measurements to surface measurements. Before discussing the fundamentals and utilization of digital image correlation (DIC), a brief overview of surface imaging will be provided. With the advent of high-quality digital CMOS and CCD cameras, it became possible to capture the full-field images of materials during deformation. Cameras offer a distinct advantage over traditional methods for capturing deformation as the field of view can be altered by merely changing the optics of the system. This modularity of the DIC system allows for both a full sample or localized images of deformation to be captured [31].

When selecting a camera for imaging in DIC experiments, it is essential first to determine the parameters of the experiment. The first parameter that must be determined is the region of interest

(ROI) that will be imaged [32]. It is ideal to select a camera where the ROI fits within the camera's field of view (FOV). Intertwine with the selected FOV of the camera, is the standoff distance (SOD) and depth of field (DOF). These parameters determine the position of the camera and the required depth to ensure the sample remains. While these are the significant parameters affecting camera selection for DIC, one must also be aware of selecting a camera with an appropriate sensor size to capture the FOV, and a low signal-to-noise ratio to capture high-quality images. Finally, it is essential to note that the camera selection and lens selection must be made together due to the interplay between sensor size and lens effects on the scale of the image.

### **2.3.2 Fundamentals of DIC**

The traditional method of analysis for strain fields such as strain gauges and extensometer only provide discrete strain measurement. For full-field strain measurements of materials optical measurement, digital image correlation (DIC) being the most common, has been adopted by researchers [33]. DIC can be broken into two general categories 2D DIC and 3D DIC. 2D DIC utilizes a single camera, which is limited to flat samples, to provide in-plane displacements and strains. For samples where out-of-plane strain fields exist, such as those exhibited in curved samples, 3D DIC is utilized. Nevertheless, the operating principles of both the DIC system can be broken down into three major phases: 1) sample preparation, 2) image acquisition, and 3) digital image processing and numerical computation.

The principles of correlation for DIC require a sufficient speckling pattern, which is achieved by a variation in greyscale patterns. This speckling pattern can be achieved through the natural texture of the material or artificially produced by applying paint to the sample surface [33]. An optimal greyscale pattern is one that is both random and abundant in a wide range of greyscale intensities. Once the samples speckle pattern is determined, a series of images can be recorded for



the reference and deformed data set by the usage of a CCD or CMOS camera. Figure 2-8 shows a standard setup for 2D DIC with a speckled sample is shown laid flat in-plane with a digital camera. A light source is typically used to illuminate the sample and prevent uneven lighting conditions. A second camera can also be used at a stereo-angle with the first, similar to the Figure 2-8 setup. This technique is known as 3D DIC and useful for calculating out-of-plane displacement and strain fields [34].

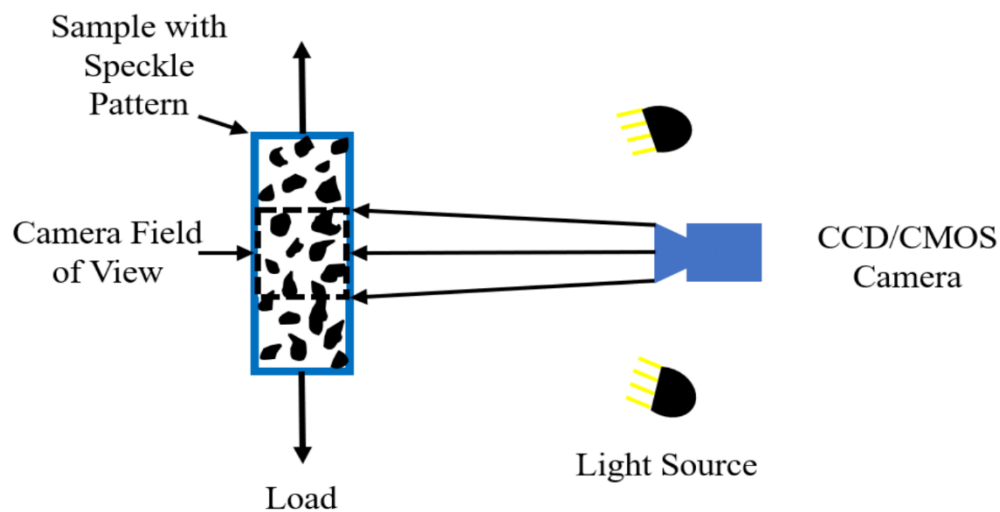


Figure 2-8: Example Schematic of a 2D DIC for a sample under mechanical loading.

The first step toward calculating the displacements is the choice of region of interest to correlate over and a square subset size [33]. Both the reference and deformed data set is then discretized into these subsets where correlation is performed. The displacement of the subset is calculated by tracking the movement of pixels within the subset by matching the grayscale level between reference and displaced dataset. Displayed in Figure 2-9 is an example of a specimen that has been speckled for DIC with a selected ROI. A single representative correlation window is shown, where the particles within are tracked to measure the displacement. To determine the degree of similarity between the subsets, a cross-correlation or the sum-squared difference

criterion is defined. The three most commonly utilized cross-correlation criterion: 1) cross-correlation (CC), 2) normalized cross-correlation (NCC), and 3) zero normalized cross-correlation (ZNCC) are defined in equations 2.4-2.10. In these equations  $f(x_i, y_i)$  and  $g(x'_i, y'_i)$  represents the greyscale intensity in the reference and deformed subsets respectively and  $f_m$  and  $g_m$  are their respective mean greyscale intensity.

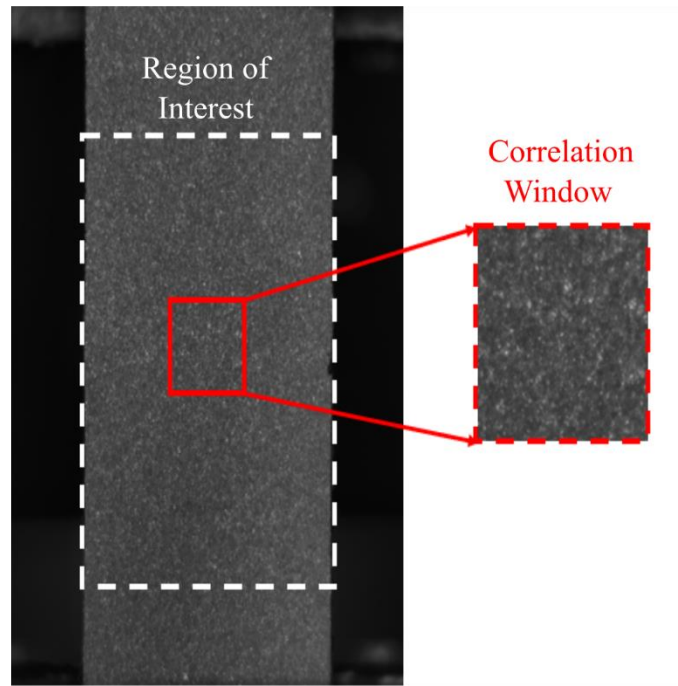


Figure 2-9: Example of a speckled test sample for DIC and representative correlation window

$$CC = \sum_{i=-M}^M \sum_{j=-M}^M [f(x_i, y_j)g(x'_i, y'_j)] \quad (2.4)$$

$$NCC = \sum_{i=-M}^M \sum_{j=-M}^M \left[ \frac{f(x_i, y_j)g(x'_i, y'_j)}{\bar{f}\bar{g}} \right] \quad (2.5)$$

$$\bar{f} = \sqrt{\sum_{i=-M}^M \sum_{j=-M}^M [f(x_i, y_j)]^2} \quad (2.6)$$

$$\bar{g} = \sqrt{\sum_{i=-M}^M \sum_{j=-M}^M [g(x'_i, y'_j)]^2} \quad (2.7)$$

$$ZNCC = \sum_{i=-M}^M \sum_{j=-M}^M \left\{ \frac{[f(x_i, y_j) - \bar{f}_m] \times [g(x'_i, y'_j) - \bar{g}_m]}{\Delta f \Delta g} \right\} \quad (2.8)$$

$$\Delta f = \sqrt{\sum_{i=-M}^M \sum_{j=-M}^M [f(x_i, y_j) - \bar{f}_m]^2} \quad (2.9)$$

$$\Delta g = \sqrt{\sum_{i=-M}^M \sum_{j=-M}^M [g(x'_i, y'_j) - \bar{g}'_m]^2} \quad (2.10)$$

The first step in computing the displacement is to determine the peak of the cross-correlation coefficient. This identifies the location of maximum similarity between the deformed and refer subset. By analyzing the change of the reference subset to form the deformed subset integer level displacements can be computed through the cross-correlation formulation [35]. However, for many application integer displacements are insufficient as deformation may lay between pixels these locations are known as sub-pixels. It is thus, required for applications that a quantification of the sub-pixel displacement be made for an accurate measure of displacement to be had.

To compute sub-pixel displacement values, an interpolation scheme is necessary. Before the degree of similarity is calculated via the cross-correlation coefficient a measure of the intensity of

the reference and deformed image must be calculated with sub-pixel accuracy. An initial guess is made by searching through the image in the spatial or frequency domain [33]. In the spatial domain, this is done by searching pixel by pixel. In contrast, in the frequency domain, this is done through the implementation of a fast Fourier transform (FFT), which is useful for most cases without large deformation or rotation [33]. In these cases, custom algorithms have been developed to obtain a reliable initial guess. After a guess is made for the initial displacement, a sub-pixel displacement algorithm, the most common being the Newton-Raphson method, can be utilized to capture the sub-pixel displacement behavior between the initial and deformed dataset [35].

Strain measurements can be calculated either directly from the displacement results of the Newton-Raphson method or through it on mathematical differentiation. Both methods have their advantages and disadvantages. Generally a direct calculation of strain through the Newton-Raphson is only applicable for strain greater than 0.010 [33]. When using the numerical approach, errors in the displacement data due to noise is reflected and amplified in the strain data [33]. Minimization of these effects is done through different smoothing algorithms that have been developed to improve the displacement data before strain measurements are calculated.

### **2.3.3 DIC for Mechanics of Materials**

DIC has provided an avenue for the analysis of the material properties of complex heterogeneous materials where traditional methods such as strain gauges may fail. DIC also provides valuable experiment data that help in the creation and validation of more accurate numerical models of these complex materials. A 3D textile glass fibre and SC-15 epoxy resin composite was subject to a 1 mm/mm bending load by Zhang *et al.* [36]. During the elastic loading region, the experimental strain results were captured via a Nikon D2 x camera in a DIC experiment. The DIC results show two distinct behaviour when the sample is loaded in the weft direction

compared to the warp direction. When loaded in the weft direction, cracking was exhibited when the tows began to kink on the compressive side. However, when the material was loaded in the warp direction, cracking formed when fibres kinked on the tensile side.

Additionally, the critical load, which corresponds to the kinking of the fibres, occurs at 4.2 mm and 4.7 mm for the warp and weft direction. Using this data, a FEM model was proposed based on the global-local modelling method for the prestress region. This model was able to predict similar peak stress to the experimental DIC data consistently.

Leung *et al.* utilized stereo-DIC to analyze the resultant effects of tensile loading effects on braid angle and radius for a tubular braided composite and how they relate to the material's elastic modulus [37]. To study these effects, a Kevlar composite impregnated in epoxy resin was subject to a tensile load. Images were obtained at three regions each 9 mm apart from each other along the braid with two stereo cameras attach to a stereomicroscope. Under these conditions, an average strain of  $1.64 \pm 0.67\%$  occurred before material failure. A change in radius and braid angle before failure was measured at  $-0.072 \pm 0.095$  mm and  $-0.8^\circ \pm 0.26^\circ$ , respectively. It was shown that the changes in radius during loading caused a resultant change in the area, thus leading to increased stress and modulus. As the axial tension causes the braid angle to decrease, a subsequent increase in longitudinal modulus can be observed. Considering the combined effects of radius change and angle change, a 9.12% increase in longitudinal modulus is observed, illustrating the importance of accurate braid angle and radius measurement for modelling the behaviour of tubular braided composites.

Melenka *et al.* expanded upon the study of tubular braided composite by using stereo-DIC to analyze the effects on braid pattern, braid angle, and load on strain fields and elastic properties [38]. Kevlar braid preforms were prepared in two different patterns: 1) diamond and 2) regular,

which were impregnated into an epoxy resin. A tension and torsion experiment were conducted separately using a universal material test stage. Tension tests were performed at a rate of 0.5 mm/min. Under tension, high regions of strains were visualized at the cross-over points, which lead to these areas to experience matrix failure. For the torsional test, a load was applied at a rate of 0.05 rad/min via a 20 Nm load cell. The torsional tests showed a linear shear stress-strain relation. After the maximum shear stress was reached, there was a continuous decrease in the stress-strain due to torsional buckling.

While the usage of DIC to study complex materials has proved a powerful tool, its adoption for the analysis of additive manufactured parts is limited. Zaldivir *et al.* extended the usage of DIC to investigate the effects of build orientation on the thermal and mechanical properties of the FFF printed parts [39]. The material of choice in this study was Ultem 9085, which was printed into ASTM D638-10 Type 1 tensile coupons. Results of the analysis showed that build orientations that produced a majority of their fibres along the load direction exhibited increased mechanical performance. The effects on the performance of the FFF parts showed a strength of roughly 45-86% of the reported materials values. The DIC measurements showed that the deformation behaviour of the parts was highly anisotropic. Indeed, based on the build orientation, the strain in the sample could develop with minimal irregularities, such is the case for a sample built on its edge, or to perpendicular strain layers for a sample produced upright.

Goodarzi Hosseinabadi *et al.* was one of the first researchers to study the utilization of DIC for the analysis of both FFF and polyjet produced parts [40]. Two honeycomb models were produced one using ABS and FFF technology and another with a photocured resin and the polyjet technology. Analysis of the strain distribution under a compressive load was then measured using a 3D DIC experimental setup. The results of the analysis showed the capability of DIC to resolve

the strain localization in the struts of the 3D printed layers. Comparing the strain data between the polyjet printed and FFF printed parts, the maximum local strains were shown to be much smaller for the polyjet part. This is contributed to the FFF parts rigidity and weld lines in the FFF materials microstructure. Thus, it was concluded that the nozzle based FFF technique was more likely to fail under plastic deformation compared to the polyjet technique.

An extension of Goodarzi Hosseinabadi *et al.* work on FFF produced honeycomb was further investigated to capture the development of shear bands. Samples were again produced with ABS filament, and subject to a compressive and flexural test [41]. Results from the experimental DIC data were then used as a point of comparison for numerical finite element (FE) simulations. The shear strain was shown to develop in three stages for the sample shear band coalescence, shear band expansion, and shear band deformation. Both the FE model and the DIC experiment showed good agreement between the strain contours and strain development.

As just shown, DIC can provide an accurate measure of displacement and strain for complex materials. The data obtained from DIC results is invaluable for analyzing the mechanical response of composites, and additive manufacturing produced parts were traditional techniques may prove unsuitable. However, DIC is not without its limitation, namely that the results are limited to surface-level measurements. In the upcoming sections, a discussion is provided in the advancement of micro-computed tomography ( $\mu$ -CT) and digital volume correlation. With the advent of these two technologies, it has become possible to capture 3D images of a sample deformation and analyze then to capture a full-field view of displacement and strain.

## ***2.4 Volume Measurements and Digital Volume Correlation***

### ***2.4.1 Fundamentals of Micro-Computed Tomography***

Before discussing the fundamentals and uses of DVC, it is important to discuss first how datasets are captured for analysis. The most commonly used method for obtaining 3D-dataset is through  $\mu$ -CT.  $\mu$ -CT is an x-ray based imaging technique in which radiographic images of samples can be taken at sub-millimeter resolutions. The  $\mu$ -CT method works by first passing x-rays produced by an x-ray receptor through the desired material [42]. As the x-ray passes through the sample, the beam is attenuated based on the density of this material [42]. The attenuated x-ray is then acquired by a sensor adjacent to the material, the x-ray receiver, and the intensity is measured as a ratio of the attenuated x-ray intensity to the initial intensity [42]. From these values, a 2D radiographic image can be reconstructed for that individual plane.

By rotating the sample within the  $\mu$ -CT machine, a series of radiographic images can be taken that describe the entire internal structure of the material [42]. This process is shown in Figure 2-10, where x-rays produced by an x-ray receptor are passed through a rotating sample and collected by the x-ray receiver. After the completion of this scan, the 2D radiographs or shadow projections must be reconstructed into a volumetric image [43]. Reconstruction is completed by applying a Fourier slice theorem [43]. The Fourier slice theorem states that Fourier transform of a parallel ray projection at any angle is the same as a line taken at the same angle is a slice of the Fourier transform of the reconstructed image. Thus by performing this over a sufficient amount of projections allows the entire Fourier space can be defined and then reconstructed to give a volumetric view of the object's internal structure [43].



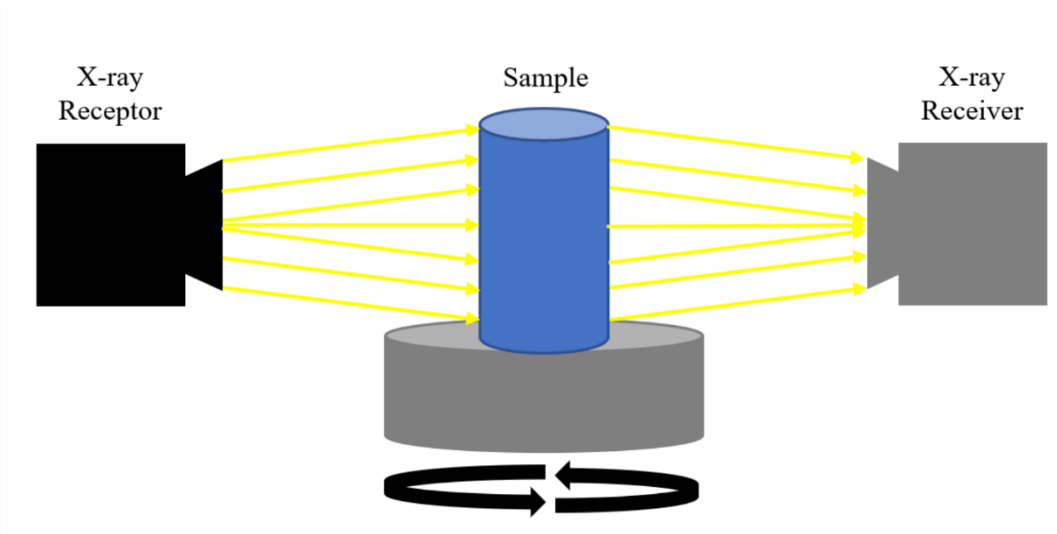


Figure 2-10: Schematic drawing showing the layout and operation of a  $\mu$ -CT machine during the scanning of sample material.

What makes  $\mu$ -CT ideal candidate for imaging composite materials is its high sensitivity to changes in density [42]. This allows for the matrix, yarns, voids and their interfaces within laminate and textile composites to be accurately mapped to a digital image and analyzed. Furthermore, as a load is applied, the response of the composite structure and formation of cracks in the structure can be visualized. By imaging and tracking the response of the structure, measurements of displacement and strain can be measured through the bulk of the sample via image processing techniques that will be discussed in depth later in sections 2.4.3 to 2.4.8.

### ***2.4.2 Micro-Computed Tomography for Composite Analysis***

$\mu$ -CT has found substantial use for the imaging and analysis of composite materials. The sub-millimeter volumetric imaging of composites allows for geometric measurements to be made on the reinforcement and matrix phase. The yarn architecture of textile composite is of particular interest to many researchers. Due to the often low and often similar density of the matrix phases, it is often useful to add contrast-enhancing additives on the particular phase of interest before

imaging. To this end, Djukic *et al.*, provided a detailed starting point for studying contrast enhancement by adding gold, copper, and iodine on carbon fabric yarns both pre and post weaving [44], [45]. Due to the presence of metals within the sample CT artifacts became apparent within the initial images. Particularly appearance of the beam hardening artifact was present. Beam hardening appears as small streaks across the image or bright spots due to the attenuation of low energy x-rays. Additionally, some light ring artifacts became present in a few of the samples which appear due to poor calibration of the sensor. To reduce the presence of these artifacts a correction algorithm during reconstruction. The addition of gold, copper, and iodine all help improved contrast of the samples with gold performing the most optimal. Furthermore, while both methods proved useful, the group was more successful when coating the fibres before weaving, as this led to better image quality and dimension accuracy when visualized.

This technique of adding material to enhance image contrast has been applied to ceramic matrix composite by Bale *et al.*, who used chemical vapour deposition to coat Boron Nitride (BN) on SiC nitride yarns [46]. Chemical vapour deposition allowed for sufficient contrast between tows to be achieved so that the architecture could be mapped and analyzed for defects and irregularity in 3D. Continuing research in this field has shown its potential for mapping composite yarn structures with a high statistical degree of dimensional accuracy in 3D via the  $\mu$ -CT method [47], [48].

Recent research in textile composites has begun to examine the geometrical properties of both 2D and 3D braided composite materials. Melenka *et al.* used the  $\mu$ -CT to examine the yarn pathing for diamond braids [49]. The cross-sections of the tubular braids were acquired for analysis of critical geometrical properties of the braid, such as aspect ratio, braid angle, and undulation utilizing  $\mu$ -CT imaging. An example of a  $\mu$ -CT cross-section of a tubular braided composite with

an 11.1 mm inner diameter (ID) can be seen in Figure 2-11. From the reconstructed cross-section, essential features of the braid architecture can be identified, such as the matrix, fibre tows and void content. An unwrapping algorithm was employed to help automate and simplify the analysis of the braids. This algorithm allowed for the mapping of individual yarns in 3D and for the aspect ratios, braid angle and fibre undulations period to be precisely measured.

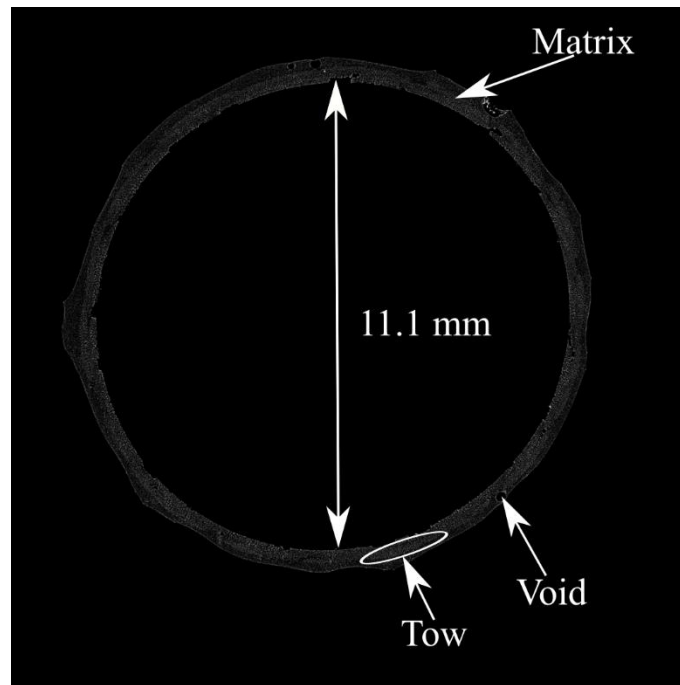


Figure 2-11: Composite architecture (Tow, voids, and matrix) of a reconstructed cross-section of a tubular braided composite with an 11.1 inner diameter (ID) produced from  $\mu$ -CT.

Ya *et al.* utilized the  $\mu$ -CT method to model and analyze the highly complex geometry of 3D full five-directional braided composites (3DF5D) [50]. A tracer yarn was added to the composite to improve image contrast for geometrical analysis. A tracer yarn is yarn of different density than the rest of the bulk of the braid material is added into a composite weave to improve image contrast. In this study, glass fibre was used as a tracer yarn in a carbon fibre composite due to its lower density. This tracer yarn allowed for the path, cross-section, and ellipticity to be calculated. Ellipticity ( $e$ ) is the ratio of the major axis to the minor axis. Equation 2.11 shows the

formulation for ellipticity, where  $a$  represents the polar radius, and  $c$  represents the equatorial radius.

$$e = \sqrt{\frac{a^2 - c^2}{a^2}} \quad (2.11)$$

In addition to making geometric measurements,  $\mu$ -CT is capable of detecting manufacturing defects such as voids and damage. The initial usage of  $\mu$ -CT was for crack and air bubble detection in more traditional materials such as concrete and sandstone. In a study performed by Skarżyński *et al.*, concrete was subject to a quasi-static three-point bend test and later imaged using  $\mu$ -CT [51], [52]. The high resolution provided by the  $\mu$ -CT allowed cracks to be measured and analyzed along the width of the material [53]. Furthermore, the technique has proven to show the minimal difference between experimental and theoretical void content by Cai *et al.* [54]. Cai *et al.* laser sintered an Aluminum powder alloyed with Silicon and magnesium (AlSi10Mg) at four different porosities and calculated the void percentage of each sample using  $\mu$ -CT and Archimedes principle. A 5.338-17.431 percent difference between porosity values from the Archimedes principle and  $\mu$ -CT measurements was found, showing the high-level accuracy of the technique.

More recently, the technique has been seeing utilization for defect and damage detection in laminates and braided composite materials. Initial studies in this area looked at directly quantifying the size, shape, and pore distribution in the matrix phases of composite materials [55]–[57]. In a study by Aratama *et al.*, they employed  $\mu$ -CT to show the connection between voids and crack formation in carbon fibre reinforced plastic (CFRP) laminates [58]. These tests were completed using an in-situ three-point bend test on a CFRP made from several  $0^\circ$  lamina stacked between a few layers of  $90^\circ$  lamina. Some key observations were made upon examination of the tomographs. In the  $90^\circ$  layers, the most significant stress contributor was in-plane transverse stresses.

Additionally, there were many voids (30  $\mu\text{m}$ ) that ran in the width direction and were several micrometres larger in diameter than the fibre (7  $\mu\text{m}$ ). These voids in the matrix acted as areas of high strain concentration and thus was the epicentre of transverse cracking in the laminate under loading.

### **2.4.3 Fundamentals of Digital Volume Correlation (DVC)**

Digital Volume Correlation (DVC) is the volumetric equivalent to the more commonly known digital image correlation (DIC). While DIC can observe the deformation at the surface of a sample, DVC gives a volumetric view. DVC software requires a reference and a deformed 3D image (ex.  $\mu$ -CT) to correlate over. Bay *et al.* first showed this technique for measuring the displacements and strains through a 3D image set.[59]. DVC operates by first discretizing an image into a series of nodes throughout the volume of the image. These nodes represent the center locations at which the displacement and strain between the reference and deformed images will be calculated.

After discretization, a correlation volume size is then defined and created around these nodal points where displacement will be calculated. To first calculate displacements, the degree of similarity between subsets is analogously calculated via 3D cross-correlation coefficient to DIC. For DVC the degree of similarity between subsets is captured through an objective function. Equation 2.12 presents the formulation for the normalized cross coefficient ( $\text{NCC}_{xyz}$ ) for DVC which is one of the most widely utilized objective functions [60]. Within this equation,  $f(x_i, y_j, z_k)$  is the representative greyscale intensity in a correlation volume, while  $g(x'_i, y'_j, z'_k)$  represents the greyscale intensity in the corresponding deformed correlation volume. A representative picture of the displacement principle for DVC is shown in Figure 2-12. For simplicities sake two particles are considered, U and W, which are located in the subset P, the reference subset. When a load is applied, the subset P may translate in x, y, & z or rotate around any axis; this deformation is

represented by  $P'$ . This geometric transformation can be calculated by tracking the movement of  $U$  and  $W$  from  $P$  to  $P'$ . It is important to note that a general recommendation of 27 particles is required for accurate correlation measurements, and two particles are shown only to allow for easy visualization of the process [61].

$$NCC_{xyz} = \frac{\sum_i \sum_j \sum_k F(x_i, y_j, z_k) G(x'_i, y'_j, z'_k)}{\sqrt{\sum_i \sum_j \sum_k F(x_i, y_j, z_k)^2 \sum_i \sum_j \sum_k G(x'_i, y'_j, z'_k)^2}} \quad (2.12)$$

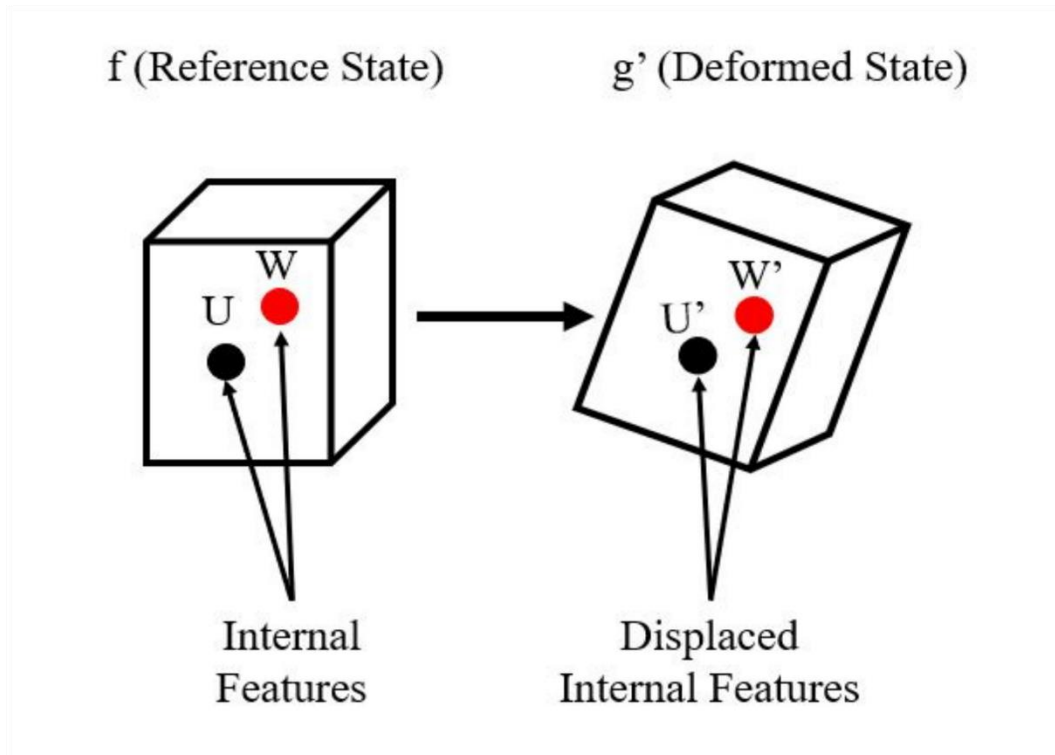


Figure 2-12: Depiction of displaced DVC sub-volume where reference particle  $U$  and  $W$  displace to from the reference state  $f$  to deformed state  $g'$  where they are shown as  $U'$  and  $W'$  respectively.

To map the reference and deformed subset on top of one another for displacement calculation, an objective function is utilized by the DVC software. Variations of the voxel intensity values form the basis of this correlation and by tracking the movement of internal features. This process

of tracking particles in 3D space can be seen in Figure 2-12. These features or “speckles” can be inherent to the material or artificially induced if the inherent contrast is insufficient for correlation. As with DIC it is often that displacement lay between voxels and the displacement must be captured in these non-integer or sub-voxel location. To achieved sub-voxel accuracy, the objective function must be minimized.

Typically, this minimization is done by utilizing using one of three techniques: 1) Levenberg-Marquadt method 2) Broyden–Fletcher–Goldfarb–Shanno, or 3) steepest decent technique [62]. By utilizing a correlation algorithm over these subsets, a highly accurate approximation of the deformation of the structure can be found. These displacements can be further transformed to allow for the observation of the full strain field. The ability to qualitatively estimate the displacement and strain fields based on an internal speckling pattern has proved useful for quantifying the properties of many different materials: bone, wood, metals, and composites.

#### **2.4.4 Open-Source DVC**

As DVC is relatively new, commercial software’s are currently prohibitive due to their high cost. Due to this fact, a few research groups have begun to develop open-source alternatives to commercial DVC software packages. Réthoré *et al.* were one of the first research groups to develop an open-source DVC software which is known as ‘uFreckles’ [63], [64]. The ‘uFreckles’ program utilizes a finite element continuum method in conjunction with a non-linear least-squares error minimization method to calculate displacement. The finite element continuum method gains its name from the fact that common finite element shape functions are utilized to help predict displacement discontinuities of the mesh. Another open-source alternative for DVC was developed by Bar-Konchba *et al* [65]. FIDVC and its software extensions were developed utilizing the MATLAB programing language for the analysis of cell-induced material formations [65], [66].

The code utilizes an iterative deformation method where subsequent passes decrease the window size to improve the resolution of sample deformation. The final open-source DVC software discussed is by Tudisco *et al.* provided a python-based DVC software known as TomoWarp 2 [67]. TomoWarp 2 was made to study the deformation of geological materials. Displacement vectors and strain vectors are calculated utilizing a local approach, where the best mapping of displacement is calculated between local correlation windows of reference and deformed datasets.

#### **2.4.5 DVC Contrast Enhancement**

Before discussing the various works in which DVC has put into practice, it is important to preface this with a discussion on image quality. For an accurate correlation to be obtained image datasets for DVC must have an internal random contrast pattern similar to the speckle patterns discussed for DIC. Despite this requirement, relatively few studies have discussed the nature of contrast regarding DVC. Croom *et al.* [61] were one of the first groups to study natural contrast patterns i.e. contrast pattern intrinsic to the material. Within Croom's study, elastic foams were crafted at different volume fractions to mimic a natural contrast pattern. These foams were then compressed to analyze the effects of deterioration of natural contrast patterns under deformation. Results showed that before 30%-40% of the speckle pattern had deteriorated within these DVC results were highly accurate. However, after this threshold, noise in the sample made displacement and strain measurement highly inaccurate.

Currently, most work focuses on samples which contain natural greyscale contrast and variation. Gonzalez *et al.* began to investigate the effects of artificial contrast enhancement [68]. This process of adding external particles to increase the contrast of the microstructure for the purpose of imaging and correlation is known as artificial speckling. To investigate this PVDF and PDMS samples were seeded various sized  $ZrO_2$  and  $SiO_2$  marker particles. Each sample was then



compressed to a certain amount of rigid-body displacement and correlated to match said displacement. A 41 x 41 x 41 voxel correlation window was utilized to calculate these displacements within each dataset. This study described most artificial speckling materials to provide a displacement accuracy of less than 5.3 % error. The selected material and seeding particle that provided the highest accuracy was 35  $\mu\text{m}$   $\text{SiO}_2$  mixed at 10% with a PDMS base..

#### **2.4.6 DVC of Trabecular Bone**

The first practical application of DVC was for the analysis of the trabecular bone of animals. A significant portion of the research in this area was performed to analyze the precision of the DVC measurement technique when applied to trabecular bone. The trabecular bone was first analyzed in Bay *et al.*, initial DVC study to emphasize the usage of the measurement technique in obtaining full-field strain values [59]. To illustrate the strain behaviour of the bone, two samples were tested: one loaded within the elastic region at a nominal strain 0.004 and 0.008, and one loaded beyond the bones yield at a nominal strain of 0.006 and 0.018. Strain measurement in the elastic sample showed pockets of considerable strain within the high-density regions of the bone. For the sample brought to yield principle, the strain begins to develop in the lower part of the sample until it reaches failure, after which high levels of local strain forms. Measurements for both samples showed the development of local strains before nominal strains, which is a behaviour that can't be observed from standard material test procedures.

In a later study, Zauel *et al.* performed a compression test on a trabecular bone and compared against the results against a FEM model [69]. Using linear regression, the two models predicted similar displacements in the loading direction resulting in an  $R^2$  value of 0.970 for a femoral sample. In contrast, results within the transverse direction proved less accurate. The vertebral results performed similarly, with slightly lower coefficients due to the sample's lower density.

Strain results were only showed a similarity when comparing strains from the average displacement of the FEM model with the DVC results. However, with the bottleneck from  $\mu$ -CT machines at the time of the study, the unaveraged strain was not directly comparable.

While most studies at this point simply focused on 1-2 specimens, Liu *et al.* studied the accuracy and precision of the measurements against both the DVC correlation method and trabecular structure [70]. Across the five different trabecular bones, the maximum likelihood estimation implemented showed the most accurate and precise results for both displacement and strain rather than the cross-correlation or normalized cross-correlation technique. Utilizing the MLE technique displacements precision across all five bone types, precision ranged between 1.86-3.39  $\mu\text{m}$  within a 40-voxel subset. The error in strain within a subset of the same size was between 345-794  $\mu\epsilon$ . These results suggested that trabecular bone DVC measurement will provide its most accurate results when analyzing bone in the yield or post-yield regimes.

Gillard *et al.* looked to study the compression behaviour of porcine trabecular bone [71]. The main aim of the study was to utilize DVC to quantify strain behaviour, bone failure, and the Poisson ratio of the trabecular bone. Results from the analysis showed strain value ranging -0.03 to 0.002, located at different edges of the material, indicating non-axial compression. As expected, as the compressive force increased strain also increased. At the maximum load step, however, layers of the sample began to crush, providing a significant source of unreliable results. Using the strain data from properly correlated regions of the sample, the Poisson ratio was able to be calculated. The results showed as compression increased, there was a decrease in the Poisson's ratio from 0.32-0.21. This showed the viability of DVC to provide accurate strain and Poisson's ratio measure as there was good agreeability between experimental results and other literature on trabecular bone.

To obtain accurate strain measurement at a tissue level, Pena Fernandez *et al.* looked to optimize imaging, post-processing and DVC setting to study bone tissue [72]. To obtain images for a localized DVC approach, image quality needed to be reduced by decreasing exposure time of the synchrotron radiation x-ray to prevent radiation damage to the tissue. To provide to allow for better segmentation of the bone and biomaterial, a local median filter and non-local mean filter were applied to the sample. By applying these methods, it became possible to investigate the full-field displacement and strain on the sample on a tissue level.

#### **2.4.7 DVC of Traditional Materials**

Tran *et al.* utilized  $\mu$ CT alongside DVC to analyze the material response of wood and polyester fibres to a compressive load [73]. The compression test was done by applying a compressive load at seven steps to compress the sample by 0 to 31% of its initial size. The DVC results showed that the movement of the fibre was solely along the axial direction, and the transverse and shear deformation negligible. The local strain showed a non-linear relation with local porosity, which compared favourably with theoretical results. Furthermore, by plotting the mean strain against the solid phase volume fraction shows a linear trend. These results showed that the material porosity could closely approximate the strain behaviour of these materials. Furthermore, verifying the applicability of DVC at estimating the strain behaviour of multiphase fibrous materials.

Along with traditional metal, some researchers have adopted the DVC technique for their alloys. Morgeneyer *et al.* conducted a feasibility analysis on the usage of DVC paired with synchrotron radiation computed laminography (SRCL) for understanding the crack behaviour of a 2XXX series of aluminum alloy [74]. Laminography was preferential in this study for capturing the ductile crack propagation in a thin sheet of alloy. A 0.15 mm radius notch was imbedded into

the aluminum surface. Using an in-situ material loading and scanning setup, the crack was scanned at a reference state and three different displacements: 0.5 mm, 0.75 mm, and 1 mm. The correlation was supported using the internal porosity and metallic particles natural present in the alloy. From the DVC study, the correlation residuals, displacements, and strain. A principle interest for this feasibility of were the correlation residuals. As the correlation residual matched to within  $4.2 \pm 0.3\%$  between the loaded states and unloaded states giving validation to the feasibility of this method.

Additionally, strain and displacement behaviour agree with that expected from the loading configuration. A follow-up study was then conducted on an Al-Cu-Li sheet using similar techniques to observe strain localization behaviour [75]. DVC results were able to capture the development in strain bands along the fracture surface. The development of strain can capture much before surface fractures to mechanical loading.

While some researcher continues to look at the feasibility of DVC at accurately capturing displacements and strains within metals, some have moved towards the implementation stage. Mostafavi *et al.* analyzed the yield behaviour around the indentation induced from a Vickers hardness test on a magnesium alloy and aluminum-silicon carbide composite [76]. Traditional hardness tests only examine the surface of the impacted structure. Still, the deformation processes such as strain hardening happen due to changes in the microstructure of the material, which can be seen through DVC. While correlation failed directly at the surface of indentation were plastic deformation caused a change, in contrast, radial and axial displacement showed good agreement between with finite element method (FEM) simulation. Additionally, it was shown that the displacement field could be utilized as a modelling input to help refine the FEM models allowing for the extrapolation of material properties..

#### **2.4.8 DVC of Composite and Non-Traditional Materials**

Brault *et al.* were one of the first to introduce the DVC technique to a composite material, by performing a 3-point bend test conducted at five load states up to 3.7 KN on a composite laminate [77]. The laminate used was composed of carbon fibres and epoxy resin with imbedded copper particles associated with the DVC subset size to help increase the resolution and improve the correlation. The results showed a low level of shear strain and displacement in a longitudinal direction, while the bending direction showed a displacement gradient with accuracy up to 0.2 voxels. Indeed, the copper may have affected the mechanical properties, but the low seed percentage shows only a result of the experimentation showed an uncertainty of 0.04 voxels.

Instead of looking at the bulk strains and displacement, Lecomte-Grosbras *et al.* applied both the DIC and DVC technique on laminate composites to understand free-edge effects [78]. A glass fibre reinforced polymer (GFRP) was subject to several loading steps from 0 N, the reference state to 8000 N when material failure occurred. The 2D DIC and DVC in this study both validate one another and show similar trends in the material with the DVC analysis allowing the evolution of displacement and its discontinuity to be measure through the depth. Three significant trends were shown about the free edge effects of the samples: residual displacement localized at the edges when the load is increased so too is the residual displacement, and as the load increases, an observable enlargement in the region of residual displacement can be observed.

For more complex composite materials, Mendoza *et al.* utilized DVC techniques for comparing 3D woven textile composites [79]. Employment of the DVC technique was used for the assessment of the yarn displacement, and differences in the material topology. To study the yarn displacement, a scan of two textiles that were manufactured in the same manner were scan via  $\mu$ -CT and compared. The displacement measurements were converted to strain and overlapped

onto the textile model. The results of these measurements showed the development of two localized strain behaviour: 1) compression of the yarns, and 2) shearing between yarn layers. To assess the capability of measuring the topological difference, Mendoza *et al.* manufacture samples with intentional defects. It was shown here that by observing the image residuals missing yarn can be identified through highly negative residuals and additional yarns can be identified through highly positive residuals.

Melenka provided a preliminary study on the utilization of DVC in combination with  $\mu$ -CT for tubular braided composites [80]. A  $45^\circ$  regular braid was made from cellulose fibres impregnated with a bio-based resin. Images of the braid were obtained utilizing  $\mu$ -CT (SkyScan 1272, Bruker, Belgium) equipped with an integrated material test stage (400 N Integrated Test Stage, MTS2, Bruker, Belgium). A reference scan was taken before applying a 244.6 N compressive load to the sample and taking the deformed scan. DVC was done with open-source python code (TomoWarp2) to examine the 3D displacement and strain fields [67]. Both 3D dimensional displacement fields and shear stress were able to visualize, showing to the potential of the technique for full-field analysis of braided composites under different loading conditions.

As a first look at the capability of mapping internal displacement fields for additive manufactured parts, Wang *et al.* created a porous polymeric structure [81]. The porous structure was then built subject to uniaxial compression tests, with compressive strains increasing stepwise from 4%-20%. The resolution of the six Cauchy strain field showed a high degree of strain that are localized periodically on the porous unit cells of the material. As the applied load increased, results showed that not only was there a significant increase in strain but its localization as well. By then extending the analysis to the calculation of principles strains on a unit cell level, it was

shown possible to predict specific damage forms and possible damage mechanisms present in the material.

With DVC being a new field, it is essential to summarize the critical inputs for image acquisition and correlation so they may be used as a building point for new and emerging research. Table 2-1 provides a recap on the five significant inputs for the  $\mu$ -CT image used in the studies previously discussed. It is vital to notice that these settings are highly dependent on the material used and resolution required for visualization of the microstructure. Additionally, Table 2-2 provides a summary of the DVC setting used in prior research specifically, the correlation window size and step size, which defines the correlation window overlap, has been provided. These two parameter play a important role in determining the amount of information within each correlation window and the overall spatial resolution of the displacement fields both of which effect displacement accuracy [82], [83]. It can be seen that a wide range of correlation window sizes and step sizes are used for each experiment. These settings are influenced by three major factors, which is the degree of deformation, the size of features in the microstructure, and greyscale distribution in each subset.

Table 2-1: Summary of inputs used in micro-CT for DVC experiments

Material	CT Information			
	Voltage	Current	Resolution	Voxel Size ( $\mu\text{m}/\text{voxel}$ )
Trabecular Bone [66]	105 kV	-	-	24.6
Femur Condyles (sheep)[67]	5-35 keV		2560x2160	2.6
Magnesium Elektron WE43 Alloy [71]	90 kV	80 $\mu\text{A}$	1015x512	3.95
Al616061 Alloy Matrix Composite with SiC Particles [71]	53 keV		4008x2672	0.9
AA2139 Aluminum Alloy [69]	25 keV		2040x2040x2040	0.7
AA2128 Al-Cu-Li Alloy [70]	25 keV		2040x2040x2040	0.7
Wood-Based Fiber Board [68]	65 kV	240 $\mu\text{A}$	1024x10240	6
Carbon Fiber Laminate with 150 $\mu\text{m}$ Copper Particles [72]	100	833	961x384	52
E-glass and M9 Epoxy Laminate [73]	60 kV	-	1920x1536	4.5
Cellulose Braid and Bio Resin [75]	40	200	4904x3280	3
Porous 3D Printed Structure [76]	140 kV	0.62 mA	1000x1024	55.3



Table 2-2: Summary of input parameters for DVC software

Material	Correlation Window (voxel x voxel x voxel)	Step Size (voxel)
Trabecular Bone [66]	64x64x64	32
Femur Condyles (sheep)[67]	112x112x112, 96x96x96, 80x80x80, 64x64x64, and 48x48x48	16
Magnesium Elektron WE43 Alloy [71]	128x128x128	64
	32x32x32	24
	16x16x16	8
A1616061 Alloy Matrix Composite with SiC Particles [71]	256x256x256 64x64x64	128 32
AA2139 Aluminum Alloy [69]	16x16x16	-
AA2128 Al-Cu-Li Alloy [70]	32x32x32	-
Wood-Based Fiber Board [68]	90x90x90	20
Carbon Fiber Laminate with 150 $\mu$ m Copper Particles [72]	31x31x31	-
E-glass and M9 Epoxy Laminate [73]	64x64x64 to 6x6x6 (at center), and 8x8x8 at (edge)	-
Cellulose Braid and Bio Resin [75]	10x10x10	5
Porous 3D Printed Structure [76]	21x21x21 to 61x61x61	10

#### 2.4.9 Gaps in Literature

As DVC is relatively new, there are many areas of study that have yet to be thoroughly investigated. As previously shown, much of the DVC researcher has been focused on the application toward materials with natural contrast patterns such as trabecular bone. However, materials that lack a sufficient natural contrast pattern such as PMC have been studied to a much lesser degree. Gonzalez *et al.* were one of the first researchers to provide a generalized outlook on the particle seeding technique, which helps to provide contrast to materials that don't have a natural contrast [68]. However, as this was one of the only studies in this area there is still many area's must be investigated before the technique can be implemented with full confidence to provide

accurate DVC results for material such as polymer matrix composite. These include investigation of different seeding particle i.e. metals and ceramics, decoupling the analysis from the MTS stage, and understanding the effects of reducing of artificially seeded datasets to help lessen computation burden. Better understanding the particle seeding technique will provide a avenue for which later implementation into complex composite materials such as braided composites and AM parts can be analyzed via DVC.

Concerning material analysis, there is still a wealth of information to be gained from DVC. The current literature only taps into a smaller portion of the material analysis that can be provided for the DVC technique. Complex materials such as composites have only been investigated to a limited degree regarding material composition and loading profile. This is no more evident than in relation to additively manufactured parts, either single-phase or composite, and braided composite materials. To this author's best knowledge, Wang *et al.* study on compressive loading of stereolithography produced porous structure is the only in the field of AM, while Melenka preliminary study on DVC is the only to examine braided composite materials [80], [81]. Thus, there is still a plethora of research to be conducted on material testing and DVC of both traditional and composite. As previously mentioned by first establishing a technique for which to provide sufficient dataset for DVC both traditionally produced, and AM produced composites can then be analyzed to provide a volumetric view of both displacement, and strain.

## **2.5 Conclusion**

The continued advancements and usage of composite materials in the industry have resulted in an increasing need for a true understanding of their material behaviour. Due to their complexity, the heterogeneous nature of composite materials, traditional material testing methods do not provide adequate information on these materials. Researchers have thus developed different testing

techniques based on the principles of capturing images of the sample during deformation and correlating over said images digitally for material data. Traditionally this is done by utilizing cameras to image the surfaces and DIC to capture the surface behaviour of these materials. However, recent research has allowed for the acquisition of 3D data via  $\mu$ -CT and correlation through DVC. The research previously discussed provides an outlook on the current data available in this field. Continued research in this area is an essential step in providing a comprehensive understanding of advanced materials like composites and additive manufactured components. This thesis looks to address the gaps present in current literature, by analyzing contrast enhancement technique with a outlook on future usage in braided composites materials. Then utilizing these findings to provide a analysis on FFF composite materials.

## 2.6 References

- [1] A. K. Kaw, *Mechanics of composite materials, second edition*. 2005.
- [2] A. P. Mouritz, *Introduction to aerospace materials*. 2012.
- [3] B. E. Spencer, “Composites in the Sporting Goods Industry,” in *Handbook of Composites*, 1998.
- [4] J. P. Carey, G. W. Melenka, A. J. Hunt, and C. Ayranci, “Introduction to braided composite material behavior,” in *Handbook of Advances in Braided Composite Materials: Theory, Production, Testing and Applications*, 2017, pp. 207–237.
- [5] J. William D. Callister, *Materials Science and Engineering 7th Ed. : An Introduction*. 2007.
- [6] I. Daniels and O. Isahi, *Engineering Mechanics of Composite Materials*, Second Edi. New York: Oxford University Press, Inc, 2006.

- [7] S. Abrate, "Impact on laminated composite materials," *Appl. Mech. Rev.*, vol. 44, no. 4, pp. 155–190, 1991.
- [8] A. R. A. Hani, M. Mariatti, A. Roslan, R. M. Nazrul, and A. R. Othman, "Influence of woven and cross-ply laminates on mechanical properties of coir epoxy composite," in *Applied Mechanics and Materials*, 2013, pp. 136–140.
- [9] J. P. Carey, "Introduction to braided composites," *Handbook of Advances in Braided Composite Materials: Theory, Production, Testing and Applications*, 2016.
- [10] J. K. Kim and M. L. Sham, "Impact and delamination failure of woven-fabric composites," *Compos. Sci. Technol.*, vol. 60, no. 5, pp. 745–761, 2000.
- [11] D. Zhang, X. Zheng, Z. Wang, T. Wu, and A. Sohail, "Effects of braiding architectures on damage resistance and damage tolerance behaviors of 3D braided composites," *Compos. Struct.*, vol. 232, 2020.
- [12] G. W. Melenka *et al.*, "Manufacturing processes for braided composite materials," in *Handbook of Advances in Braided Composite Materials: Theory, Production, Testing and Applications*, 2017, pp. 47–153.
- [13] K. Birkefeld, M. Röder, T. Von Reden, M. Bulat, and K. Drechsler, "Characterization of biaxial and triaxial braids: Fiber architecture and mechanical properties," *Appl. Compos. Mater.*, vol. 19, no. 3–4, pp. 259–273, 2012.
- [14] J. Carey, M. Munro, and A. Fahim, "Regression-based model for elastic constants of 2D braided/woven open mesh angle-ply composites," *Polym. Compos.*, vol. 26, no. 2, pp. 152–164, 2005.

- [15] C. Ayranci and J. P. Carey, “Experimental validation of a regression-based predictive model for elastic constants of open mesh tubular diamond-braid composites,” *Polym. Compos.*, vol. 32, no. 2, pp. 243–251, 2011.
- [16] J. Carey, A. Fahim, and M. Munro, “Design of braided composite cardiovascular catheters based on required axial, flexural, and torsional rigidities,” *J. Biomed. Mater. Res. - Part B Appl. Biomater.*, vol. 70, no. 1, pp. 73–81, 2004.
- [17] H. Fu *et al.*, “Overview of Injection Molding Technology for Processing Polymers and Their Composites,” *ES Mater. Manuf.*, vol. 8, pp. 3–23, 2020.
- [18] S.-J. Liu, “Injection molding in polymer matrix composites,” in *Manufacturing Techniques for Polymer Matrix Composites (PMCs)*, 2012.
- [19] J. Andrzejewski, M. Barczewski, and M. Szostak, “Injection molding of highly filled polypropylene-based biocomposites. Buckwheat husk and wood flour filler: A comparison of agricultural and wood industry waste utilization,” *Polymers (Basel)*, vol. 11, no. 11, 2019.
- [20] D. Shi, X. Xiao, W. Lee, and I. M. Jaisuk, “Fiber Orientation Measurement of Injection Molded Long-Glass-Fiber Reinforced Thermoplastics,” in *28th Annual Technical Conference of the American Society for Composites*, 2013.
- [21] A. Dey and N. Yodo, “A systematic survey of FDM process parameter optimization and their influence on part characteristics,” *Journal of Manufacturing and Materials Processing*. 2019.
- [22] P. S. Ujeniya and N. V. Rachchh, “A review on Manufacturing, Machining, and recycling

- of 3D printed composite materials.,” *IOP Conf. Ser. Mater. Sci. Eng.*, vol. 653, no. 1, 2019.
- [23] Y. Sano, R. Matsuzaki, M. Ueda, A. Todoroki, and Y. Hirano, “3D printing of discontinuous and continuous fibre composites using stereolithography,” *Addit. Manuf.*, vol. 24, pp. 521–527, 2018.
- [24] S. Hwang, E. I. Reyes, K. sik Moon, R. C. Rumpf, and N. S. Kim, “Thermo-mechanical Characterization of Metal/Polymer Composite Filaments and Printing Parameter Study for Fused Deposition Modeling in the 3D Printing Process,” *J. Electron. Mater.*, vol. 44, no. 3, pp. 771–777, 2015.
- [25] I. Blanco, “The Use of Composite Materials in 3D Printing,” *J. Compos. Sci.*, vol. 4, no. 42, 2020.
- [26] G. W. Melenka, B. K. O. Cheung, J. S. Schofield, M. R. Dawson, and J. P. Carey, “Evaluation and prediction of the tensile properties of continuous fiber-reinforced 3D printed structures,” *Compos. Struct.*, 2016.
- [27] R. T. L. Ferreira, I. C. Amatte, T. A. Dutra, and D. Bürger, “Experimental characterization and micrography of 3D printed PLA and PLA reinforced with short carbon fibers,” *Compos. Part B Eng.*, 2017.
- [28] N. Shahrubudin, T. C. Lee, and R. Ramlan, “An overview on 3D printing technology: Technological, materials, and applications,” *Procedia Manuf.*, vol. 35, pp. 1286–1296, 2019.
- [29] S. Y. Fu, X. Q. Feng, B. Lauke, and Y. W. Mai, “Effects of particle size, particle/matrix

- interface adhesion and particle loading on mechanical properties of particulate-polymer composites,” *Compos. Part B Eng.*, vol. 39, no. 6, pp. 933–961, 2008.
- [30] M. Nikzad, S. H. Masood, and I. Sbarski, “Thermo-mechanical properties of a highly filled polymeric composites for Fused Deposition Modeling,” *Mater. Des.*, vol. 32, no. 6, pp. 3448–3456, 2011.
- [31] G. W. Melenka and C. Ayranci, “Advanced measurement techniques for braided composite structures: A review of current and upcoming trends,” *Journal of Composite Materials*. 2020.
- [32] R. Bigger *et al.*, “A Good Practices Guide for Digital Image Correlation,” *Int. Digit. Image Correl. Soc.*, vol. 94, 2018.
- [33] B. Pan, K. Qian, H. Xie, and A. Asundi, “Two-dimensional digital image correlation for in-plane displacement and strain measurement: A review,” *Meas. Sci. Technol.*, vol. 20, no. 6, 2009.
- [34] J. J. Orteu, “3-D computer vision in experimental mechanics,” *Opt. Lasers Eng.*, vol. 47, no. 3–4, pp. 282–291, 2009.
- [35] B. Pan, H. M. Xie, B. Q. Xu, and F. L. Dai, “Performance of sub-pixel registration algorithms in digital image correlation,” in *Measurement Science and Technology*, 2006.
- [36] D. Zhang, A. M. Waas, M. Pankow, C. F. Yen, and S. Ghiorse, “Flexural behavior of a layer-to-layer orthogonal interlocked three-dimensional textile composite,” *J. Eng. Mater. Technol. Trans. ASME*, vol. 134, no. 3, pp. 031009–031017, 2012.
- [37] C. K. Leung, G. W. Melenka, D. S. Nobes, and J. P. Carey, “The effect on elastic modulus

- of rigid-matrix tubular composite braid radius and braid angle change under tensile loading,” *Compos. Struct.*, vol. 100, pp. 135–143, Jun. 2013.
- [38] G. W. Melenka and J. P. Carey, “Experimental analysis of diamond and regular tubular braided composites using three-dimensional digital image correlation,” *J. Compos. Mater.*, vol. 51, no. 28, pp. 3887–3907, 2017.
- [39] R. J. Zaldivar, D. B. Witkin, T. McLouth, D. N. Patel, K. Schmitt, and J. P. Nokes, “Influence of processing and orientation print effects on the mechanical and thermal behavior of 3D-Printed ULTEM ® 9085 Material,” *Addit. Manuf.*, vol. 13, pp. 71–80, 2017.
- [40] H. Goodarzi Hosseinabadi, R. Bagheri, L. Avila Gray, V. Altstädt, and K. Drechsler, “Plasticity in polymeric honeycombs made by photo-polymerization and nozzle based 3D-printing,” *Polym. Test.*, vol. 63, pp. 163–167, 2017.
- [41] H. Goodarzi Hosseinabadi, R. Bagheri, and V. Altstädt, “Shear band propagation in honeycombs: numerical and experimental,” *Rapid Prototyp. J.*, vol. 24, no. 2, pp. 477–484, 2018.
- [42] S. K. Boyd, “Micro-computed tomography,” in *Advanced Imaging in Biology and Medicine: Technology, Software Environments, Applications*, 2009, pp. 3–25.
- [43] M. J. Paulus, S. S. Gleason, S. J. Kennel, P. R. Hunsicker, and D. K. Johnson, “High Resolution X-ray Computed Tomography: An Emerging Tool for Small Animal Cancer Research,” *Neoplasia*, vol. 2, no. 1–2, 2000.
- [44] L. P. Djukic, I. Herszberg, W. R. Walsh, G. A. Schoepner, and B. Gangadhara Prusty,



- “Contrast enhancement in visualisation of woven composite architecture using a MicroCT Scanner. Part 2: Tow and preform coatings,” *Compos. Part A Appl. Sci. Manuf.*, vol. 42, no. 12, pp. 1870–1879, 2009.
- [45] L. P. Djukic, I. Herszberg, W. R. Walsh, G. A. Schoeppner, B. Gangadhara Prusty, and D. W. Kelly, “Contrast enhancement in visualisation of woven composite tow architecture using a MicroCT Scanner. Part 1: Fabric coating and resin additives,” *Compos. Part A Appl. Sci. Manuf.*, vol. 40, no. 5, pp. 553–565, 2009.
- [46] H. Bale, M. Blacklock, M. R. Begley, D. B. Marshall, B. N. Cox, and R. O. Ritchie, “Characterizing three-dimensional textile ceramic composites using synchrotron x-ray micro-computed-tomography,” *J. Am. Ceram. Soc.*, vol. 95, no. 1, pp. 392–402, 2012.
- [47] Y. Liu, I. Straumit, D. Vasiukov, S. V. Lomov, and S. Panier, “Prediction of linear and non-linear behavior of 3D woven composite using mesoscopic voxel models reconstructed from X-ray micro-tomography,” *Compos. Struct.*, vol. 179, pp. 568–579, 2017.
- [48] F. Desplentere, S. V. Lomov, D. L. Woerdeman, I. Verpoest, M. Wevers, and A. Bogdanovich, “Micro-CT characterization of variability in 3D textile architecture,” *Compos. Sci. Technol.*, vol. 65, no. 13, pp. 1920–1930, 2005.
- [49] G. W. Melenka, E. Lepp, B. K. O. Cheung, and J. P. Carey, “Micro-computed tomography analysis of tubular braided composites,” *Compos. Struct.*, vol. 131, pp. 384–396, 2015.
- [50] J. Ya, Z. Liu, and Y. Wang, “Micro-CT Characterization on the Meso-Structure of Three-Dimensional Full Five-Directional Braided Composite,” *Appl. Compos. Mater.*, vol. 24, no. 3, pp. 593–610, 2017.

- [51] V. Cnudde, A. Cwirzen, B. Masschaele, and P. J. S. Jacobs, "Porosity and microstructure characterization of building stones and concretes," *Eng. Geol.*, vol. 103, no. 3–4, pp. 76–83, 2009.
- [52] V. Cnudde, M. Boone, J. Dewanckele, M. Dierick, L. Van Hoorebeke, and P. Jacobs, "3D characterization of sandstone by means of X-ray computed tomography," *Geosphere*, vol. 7, no. 1, pp. 54–61, 2011.
- [53] Skarzyński and J. Tejchman, "Experimental investigations of fracture process in concrete by means of X-ray micro-computed tomography," *Strain*, vol. 52, no. 1, pp. 26–45, 2016.
- [54] X. Cai, A. A. Malcolm, B. S. Wong, and Z. Fan, "Measurement and characterization of porosity in aluminium selective laser melting parts using X-ray CT," *Virtual Phys. Prototyp.*, vol. 10, no. 4, pp. 195–206, 2015.
- [55] S. M. Sisodia, S. C. Garcea, A. R. George, D. T. Fullwood, S. M. Spearing, and E. K. Gamstedt, "High-resolution computed tomography in resin infused woven carbon fibre composites with voids," *Compos. Sci. Technol.*, vol. 131, pp. 12–21, 2016.
- [56] M. Mehdikhani, I. Straumit, L. Gorbatiikh, and S. V. Lomov, "Detailed characterization of voids in multidirectional carbon fiber/epoxy composite laminates using X-ray micro-computed tomography," *Compos. Part A Appl. Sci. Manuf.*, vol. 125, 2019.
- [57] M. John and R. V. Prakash, "Void content measurement in fiber reinforced plastic composites by X-ray computed tomography," *Mater. Sci. Forum*, vol. 928, pp. 38–44, 2018.
- [58] S. Aratama, R. Hashizume, Y. Tsumura, M. Nishikawa, and M. Hojo, "Influence of voids

- on transverse crack onset location in CFRP laminates using x-ray computed tomography,” in *ICCM International Conferences on Composite Materials*, 2015.
- [59] B. K. Bay, T. S. Smith, D. P. Fyhrie, and M. Saad, “Digital volume correlation: Three-dimensional strain mapping using x-ray tomography,” *Exp. Mech.*, vol. 39, no. 3, pp. 217–226, 1999.
- [60] F. Scarano, “Tomographic PIV: Principles and practice,” *Measurement Science and Technology*. 2013.
- [61] B. P. Croom, H. Jin, B. Mills, and X. Li, “Effect of Fragile Speckle Patterns on Accuracy of Digital Volume Correlation,” *Exp. Mech.*, vol. 49, no. 7, pp. 991–1005, 2019.
- [62] B. C. Roberts, E. Perilli, and K. J. Reynolds, “Application of the digital volume correlation technique for the measurement of displacement and strain fields in bone: A literature review,” *J. Biomech.*, vol. 47, no. 5, pp. 923–934, 2014.
- [63] W. Hilth, D. Ryckelynck, and C. Menet, “Data Pruning of Tomographic Data for the Calibration of Strain Localization Models,” *Math. Comput. Appl.*, 2019.
- [64] J. Réthoré, S. Roux, and F. Hild, “From pictures to extended finite elements: extended digital image correlation (X-DIC),” *Comptes Rendus - Mec.*, 2007.
- [65] E. Bar-Kochba, J. Toyjanova, E. Andrews, K. S. Kim, and C. Franck, “A Fast Iterative Digital Volume Correlation Algorithm for Large Deformations,” *Exp. Mech.*, vol. 55, no. 1, pp. 261–274, 2015.
- [66] J. Toyjanova, E. Bar-Kochba, C. López-Fagundo, J. Reichner, D. Hoffman-Kim, and C. Franck, “High resolution, large deformation 3D traction force microscopy,” *PLoS One*,

vol. 9, no. 4, 2014.

- [67] E. Tudisco, E. Andò, R. Cailletaud, and S. A. Hall, “TomoWarp2: A local digital volume correlation code,” *SoftwareX*, 2017.
- [68] J. Gonzalez and J. Lambros, “A Parametric Study on the Influence of Internal Speckle Patterning for Digital Volume Correlation in X-Ray Tomography Applications,” *Exp. Tech.*, vol. 40, no. 5, pp. 1447–1459, 2016.
- [69] R. Zael, “Comparison of the Linear Finite Element Prediction of Deformation and Strain of Human Cancellous Bone to 3D Digital Volume Correlation Measurements,” *J. Biomech. Eng.*, vol. 128, no. 1, pp. 1–6, 2006.
- [70] L. Liu and E. F. Morgan, “Accuracy and precision of digital volume correlation in quantifying displacements and strains in trabecular bone,” *J. Biomech.*, vol. 40, no. 15, pp. 3516–3520, 2007.
- [71] F. Gillard *et al.*, “The application of digital volume correlation (DVC) to study the microstructural behaviour of trabecular bone during compression,” *J. Mech. Behav. Biomed. Mater.*, vol. 29, pp. 480–499, 2014.
- [72] M. Peña Fernández, A. H. Barber, G. W. Blunn, and G. Tozzi, “Optimization of digital volume correlation computation in SR-microCT images of trabecular bone and bone-biomaterial systems,” *J. Microsc.*, vol. 272, no. 3, pp. 213–228, 2018.
- [73] H. Tran, P. Doumalin, C. Delisee, J. C. Dupre, J. Malvestio, and A. Germaneau, “3D mechanical analysis of low-density wood-based fiberboards by X-ray microcomputed tomography and Digital Volume Correlation,” *J. Mater. Sci.*, vol. 48, no. 8, pp. 3198–

3212, 2013.

- [74] T. F. Morgeneyer, L. Helfen, H. Mubarak, and F. Hild, “3D Digital Volume Correlation of Synchrotron Radiation Laminography Images of Ductile Crack Initiation: An Initial Feasibility Study,” *Exp. Mech.*, vol. 53, pp. 543–556, 2013.
- [75] T. F. Morgeneyer *et al.*, “In situ 3-D observation of early strain localization during failure of thin Al alloy (2198) sheet,” *Acta Mater.*, vol. 69, pp. 78–91, 2014.
- [76] M. Mostafavi *et al.*, “Yield behavior beneath hardness indentations in ductile metals, measured by three-dimensional computed X-ray tomography and digital volume correlation,” *Acta Mater.*, vol. 82, pp. 468–482, 2015.
- [77] R. Brault, A. Germaneau, J. C. Dupré, P. Doumalin, S. Mistou, and M. Fazzini, “In-situ Analysis of Laminated Composite Materials by X-ray Micro-Computed Tomography and Digital Volume Correlation,” *Exp. Mech.*, vol. 53, no. 7, pp. 1143–1151, 2013.
- [78] P. Lecomte-Grosbras, J. Réthoré, N. Limodin, J. F. Witz, and M. Brieu, “Three-Dimensional Investigation of Free-Edge Effects in Laminate Composites Using X-ray Tomography and Digital Volume Correlation,” *Exp. Mech.*, vol. 55, no. 1, pp. 301–311, 2015.
- [79] A. Mendoza, J. Schneider, E. Parra, E. Obert, and S. Roux, “Differentiating 3D textile composites: A novel field of application for Digital Volume Correlation,” *Compos. Struct.*, vol. 208, pp. 735–743, 2019.
- [80] G. W. Melenka, “Digital volume correlation analysis of braided composites,” in *Digital Volume Correlation Analysis of Braided Composites*, 2018.

- [81] B. Wang, L. Sun, and B. Pan, "Mapping internal deformation fields in 3D printed porous structure with digital volume correlation," *Polym. Test.*, vol. 78, 2019.
- [82] H. Haddadi and S. Belhabib, "Use of rigid-body motion for the investigation and estimation of the measurement errors related to digital image correlation technique," *Opt. Lasers Eng.*, vol. 46, no. 2, pp. 185–196, 2008.
- [83] J. L. W. Carter, M. D. Uchic, and M. J. Mills, "Impact of Speckle Pattern Parameters on DIC Strain Resolution Calculated from In-situ SEM Experiments," in *Conference Proceedings of the Society for Experimental Mechanics Series*, 2015.

## Chapter 3: Artificial Seeding for Micro-Computed Tomography Image Contrast Enhancement for Digital Volume Correlation

### 3.1 Introduction

Composite materials are a multi-phase material composed of a reinforcing phase that has been impregnated into a material matrix [1]. Comparatively to their traditional material counterparts, composites display a high strength to weight ratio. This overall reduction in mass results in less material needed to manufacture a part and energy saving (ex. fuel savings) than an equivalent part made from traditional engineer part. These properties have led many industries, such as aerospace, sporting equipment, and biomedical materials, to manufacture their goods using composite alternatives. While many industries have begun to utilize composites, there are still many challenges that prevent these materials from widespread adoption. One of the most pressing challenges with composite materials is the assessment of mechanical properties. Due to the complex multi-phase structure of composites, the material properties are typically non-isotropic, and displacement fields non-homogenous making them challenging to analyze using traditional methods such as strain gauges. Currently, one of the common ways to obtain full-field displacement and strain measurement is via two dimensional (2D) and three dimensional (3D) digital image correlation (DIC) [2]–[8]. While, these measurements are able to capture the non-homogenous deformation field they are restrictive as they only provide information along the surface of the material [3]. Thus, for composite behaviour to fully be understood a method in which the deformation throughout the bulk of the material can be analyzed is crucial.

Micro-computed tomography ( $\mu$ -CT) is a radiographic imaging technique that allows for the non-destructive analysis of materials in 3D. The  $\mu$ -CT approach can be used to image the internal microstructure of composites [9].  $\mu$ -CT operates by emitting X-rays through a material to capture

the internal structure of the sample [9]. As the X-ray passes through a sample, the beam attenuates with the density of the material [9]. By measuring the ratio of the attenuated beam to the original beam, a shadow projection is formed, which can be reconstructed into cross-sections of the internal micro-structure [9].  $\mu$ -CT has proven itself a powerful tool for the analysis of the geometry of textile and braided composite materials [10],[11]. Additionally, its ability to resolve internal features on the microscale has proven useful for the identification of voids and irregularities within braided structures [10].

Analysis of 3D full-field deformation of a material can be done by combining the image data from  $\mu$ -CT with a measurement method known as Digital volume correlation (DVC). DVC is the three-dimensional (3D) volumetric counterpart to digital image correlation (DIC). DIC is commonly utilized for measuring displacement and strains of complex materials such as braided composites, wood, metals and biological materials [2]–[4], [7], [8], [12]. However, DVC has a distinct advantage over DIC since it is a volumetric technique rather than a surface measurement technique, thus allowing for full internal 3D volumetric displacement and strain fields to be visualized. The principles of DVC were first described by Bay *et al.* [13]. DVC operates by first discretizing a reference and deformed 3D datasets into a series of nodes [13]. By defining a subset size which is placed at the center of each node, an objective function is used to map the deformed dataset to the reference [13]. For a successful correlation, there must be variation in greyscale intensity throughout the micro-structure [13]. The full-field volumetric view of the displacement and strain behaviour has proved particularly useful for the analysis of various complex material [14]–[19].



The usage of DVC in its early stages had primarily been focused on obtaining strain fields of trabecular bone [20], [21]. As the technique further developed, researchers began to utilize this for more typical engineering material such as wood and metals [15], [16]. More recent studies have adopted this method for strain field analysis of composite structures, such as composite laminates and textiles [17], [19], [22]–[25]. However, DVC measurements are still an emerging area and are computationally intensive due to the large datasets required as inputs. As a result, limited studies have been performed for composites structures.

While the application of DVC for various material has been the primary focus of current research, there are relatively few studies that focus on the preparation of samples, and analysis of sample adequacy for a DVC measurement such as that which has been provided for DIC by Haddadi *et al.* [26]. Gonzalez *et al.* were one of the first to analyze the effects of adding ZrO<sub>2</sub> and SiO<sub>2</sub> marker particles to PDMS and PVDF samples [27]. In this study, samples were mechanical compressed, and the accuracy of the DVC to match the displacement from the compression was measured. From this analysis, the 35 μm SiO<sub>2</sub> was selected for use in a uniaxial compression test to measure displacement and strain. Croom *et al.* focused their work on the analysis of natural contrast patterns by creating foams with various void contents. The foams were then compressed, and DVC measurements were done to measure both the displacement and strain accuracy for the different void content and compression states.

While these studies provide an initial basis for the analysis of different datasets for DVC, there are still many unanswered questions that need to be addressed for DVC to meet its full potential for composite analysis. For studies focused on artificial speckling, the measure of accuracy has been previously tied to displacement provided by the material test stage (MTS). As such, any lack of rigidity, error in the load cell, or movement of the sample can introduce sources of error to the

data. Additionally, to adequately address how to handle large datasets leading to the long processing time and intensive computations has not been discussed. Finally, in the analysis of artificial speckling, to the best of the author's knowledge, no studies have investigated the displacement and strain behaviour around a samples that contain features such as a hole or notch.

The focus of this work is to outline the usage of artificial seeding for obtaining high-quality tomographs for DVC studies with a focus for later use in composite materials. Specifically, this study will examine the effects provided by seeding different sized metal and ceramic particles in a polymer matrix phase to provide images that are suitable for DVC analysis. To examine the effect of artificial seeding, epoxy resin was chosen as a polymer base for which copper, zirconium (IV) oxide, and aluminium nitride particles were seeded. After seeding these samples, datasets to analyses the seeding effectiveness for DVC were captured via a desktop  $\mu$ -CT.

The DVC measurement technique relies on a random image contrast for accurate deformation and strain measurement to captured. This contrast pattern can be formed naturally or can be artificially produced (the focus of this study) [27], [28]. When evaluating sample contrast, it is necessary to have a sufficient grayscale distribution within the image dataset. The greyscale distribution for images obtained through  $\mu$ -CT relates to the density of different phases in the microstructure of the material. The usage of an artificial seeding technique to improve image contrast was explored in this work through an error assessment made by artificially displacing the  $\mu$ -CT data by 35  $\mu\text{m}$ , thus eliminating any errors present from displacing the samples mechanically. An open-source MATLAB based DVC software, fast-iterative digital volume correlation (FIDVC), was then used to determine how accurately this movement could be captured for each seeding particle, and the effect of DVC inputs[29]. The FIDVC software operates by performing multiple iterations, each with subsequently smaller subsets to improve displacement

accuracy. It is important to note that this software and its extension module LD-3D-TFM were initially programmed to capture large deformations and strain, and traction force measurement for cell material but it has been repurposed for determining the optimal seeding particles required for material analysis in this study [30].

Once the optimal seeding particle and DVC parameters were determined, a DVC measurement was conducted on an epoxy sample subjected to compressive loading. A hole was introduced in the test sample to create a stress concentration and to allow for analysis of the resulting volumetric displacement and strain fields. Two views of deformation were captured one with a large volume of interest (VOI), but reduced resolution to decrease computation time, and one at a full resolution to accurately capture deformation around the center hole of the sample. This allowed for the 3D displacement and 3D equivalent strain fields to be captured throughout the sample. The methods utilized in this study provide a framework for acquiring high contrast images for the DVC analysis. This methodology can be later adopted for the analysis of strain fields within advanced composite structures such as braided composites, laminated composites, textile composites, or 3D printed composite structures.

## **3.2 Methodology**

### **3.2.1 Sample Preparation**

The test samples were prepared from a two-part epoxy made from resin (#2000 epoxy resin, Fibre Glast, Brookville, OH), and hardener (#2020 epoxy hardener, Fibre Glast, Brookville, OH). The resin and hardener were mixed at a ratio of 100:27 wt%. Within the epoxy, different size and density seeding particles were embedded and mixed, which are shown in Table 3-1. The difference between the epoxy and the denser seeding particles, is of particular importance as this will result in two distinct phases appearing in the  $\mu$ -CT tomographs. These particles were manually mixed

into the epoxy mixture with a weight percentage of 5%. The samples were cured in cylindrical Pyrex test tubes with a 10mm outer diameter and 8.5 mm inner diameter. Each test tube was placed inside an oven (5851 vacuum oven, Napco, Winchester, VA) at 66 °C (150 °F) for 6 hrs to expedite curing time. The resulting cured sample had an 8.5 mm in diameter and 11.5 mm in length.

For the loading test, a 2 mm hole was drilled through the centre of the sample to introduce a stress concentration. The manufactured test sample and testing fixture are shown in Figure 3-1 a). These final dimensions are shown to coincide with the inner diameter of the test tube and drill bit size used to create the center hole. The epoxy test sample contained with the material testing stage used to load the sample in this study is shown in Figure 3-1 b). The testing fixture consists of single static platen which the top or static face of the sample is placed against and a movable platen to provide compression and load cell force measurements. The load cell of this material test stage adapts with the  $\mu$ -CT to allow for imaging with in-situ deformation measurements.

Table 3-1: Size and density of particles used for epoxy seeding

Particle	Particle Size ( $\mu\text{m}$ )	Density ( $\text{kg}/\text{m}^3$ )
Copper (200 micron purity 100%, Copper powder coarse, Goodfellow, England)	200	8960
Copper (50 micron purity 100%, Copper powder coarse, Goodfellow, England)	50	8960
Copper (14-25 micron purity 99.8%, Copper powder, Sigma Aldrich, Canada)	14-25	8960
Zirconium (IV) Oxide (50 micron purity Zirconium (IV) oxide, Sigma Aldrich, Canada)	50	5680
Aluminum Nitride (10 micron Aluminium nitride, Sigma Aldrich, Canada)	10	3950
Epoxy Resin	Mixture Ratio (resin/hardener)	Density ( $\text{kg}/\text{m}^3$ )
Fiberglast 2000 Series Epoxy	100:27%	1134.89

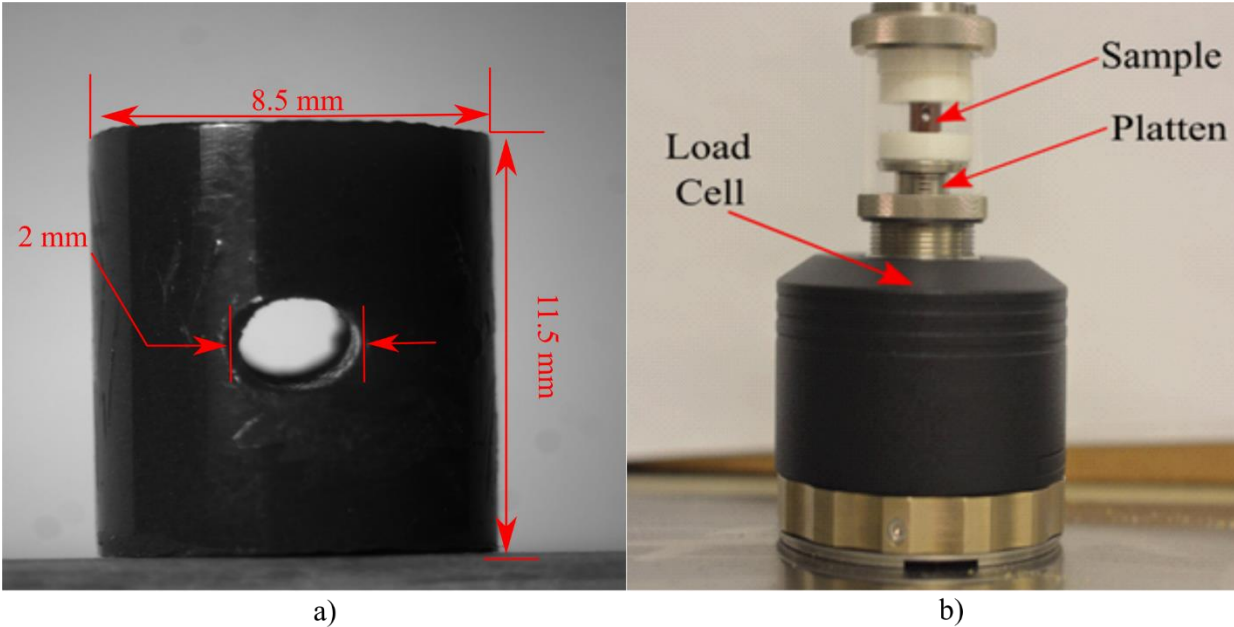


Figure 3-1: Test epoxy sample for DVC analysis: (a) Final cured sample of the epoxy-copper sample, (b) Epoxy sample within the material test stage. The material test stage is placed within the  $\mu$ -CT scanner for in-situ mechanical testing

### 3.2.2 Computed Tomography

Sample x-ray imaging was performed using a desktop  $\mu$ -CT (Skyscan 1272  $\mu$ -CT scanner, Bruker, Belgium) to obtain 3D datasets. Datasets were collected for all epoxy samples seeded with the particles outlined in Table 3-1. Table 3-2 shows the scanning parameters utilized to image each sample of seeded epoxy. The  $\mu$ -CT settings for these scans were based on the procedures and recommendation for obtaining a high-quality scan by the manufacturers of the  $\mu$ -CT. For this study, the scanning parameters were kept constant, and thus, the voltage and current were chosen to ensure all particles could be visualized. As a result of the selected voltage, a 0.5 mm aluminium filter was selected based on manufacturer recommendations to ensure high contrast images and minimize X-ray artefacts. The resolution of the scan was set to 4904 pixels by 3280 pixels with a pixel size of 3.5  $\mu\text{m}/\text{px}$ , capturing a volume of 3.47  $\text{cm}^3$ . These settings allowed for the entire sample volume (2.61  $\text{mm}^3$ ) to be in the VOI while still being able to resolve the smallest particles (10  $\mu\text{m}$  aluminium oxide) within the epoxy sample. A 0.1° rotation step was chosen to provide a

good signal to noise ratio on the scan and ensure all particles are adequately defined. To reduce scan time due to the general symmetry of a 180° scan was performed rather than a 360° scan. These scanning parameters resulted in 1920 X-ray shadow projections. These shadow projections were then converted into 2D bit maps through the use of a reconstruction software (NRecon version 1.7.1.0, Bruker, Belgium). Each dataset was then used to determine the optimal seeding particles based on contrast, particle distribution, and their overall cross-correlation coefficient.

Table 3-2: Scanning parameters utilized for acquiring tomographs of seeded epoxy

Scan Parameter	Setting
Source Voltage	70 kV
Source Current	142 $\mu$ A
Resolution	4904 pixels by 3280 pixels
Pixel Size	3.5 $\mu$ m/pixels
Filter	0.5 mm aluminium filter
Rotation Step	0.1°

After the optimal seeding particle size was determined, a deformed data set was captured to analyze the deformation and strain behaviour epoxy sample through DVC. A compressive load was applied by utilizing the  $\mu$ -CT's corresponding integrated MTS (440 N integrated test stage, Bruker Belgium) on the sample with the 2 mm drilled hole. The same scanning parameters previously discussed used for the compressive testing and DVC analysis as well. A custom platen was 3D printed to aid in sample alignment within the MTS during compression. Scans were performed on the sample at two different load steps: 1) 100 N, and 2) 300 N. Between each load step, the sample was stabilized at each force for 5 minutes before scanning.

After scanning at each load step, the image x-ray projections were reconstructed into a series of 2D perpendicular cross-sectional images that span the volume of the scanned sample. Reconstruction was performed utilizing a reconstruction software package (NRecon version

1.7.1.0, Bruker, Belgium) and reconstruction engine (InstaRecon version 2.3.0.7, Bruker Belgium). For reconstruction, a threshold of greyscale values must be selected that fully capture all features within the image microstructure. The reconstruction software manufacturers recommends that the lower limit be set to attenuation of 0 (-1000 HU), and the upper limit be set to a 10-20% higher than the maximum variation in greyscale [31]. An example X-ray projection of the epoxy sample is shown in Figure 3-2 a). A reconstructed cross-section along the A-A plane of the particle impregnated epoxy is shown in Figure 3-2 b). Observing the A-A plane, the contrast between the epoxy and particles are easily identifiable from one another due to their different greyscale values associated with their density. Additionally, the center hole can be seen represented by the black pixel streak bisecting each half of the epoxy. The resulting reconstruction process leads to 2940 images with a resolution of 4904 px by 4904 px.

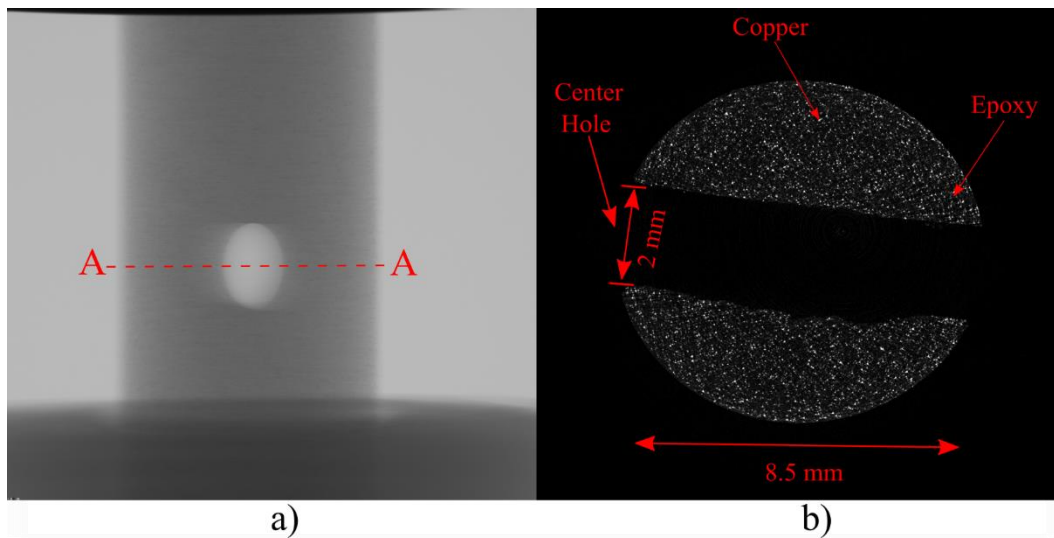


Figure 3-2: Example images from CT scan of copper impregnated epoxy sample: a) X-ray shadow projection showing the sample with central hole and b) reconstructed cross-section across the A-A plane (contrast-enhanced where the copper particles and epoxy can be seen)

### **3.2.3 Pre-Processing for Digital Volume Correlation**

Due to the computational load that is required to perform a DVC measurement, the images were cropped to lessen the burden. Images were cropped to different sizes based on the analysis (Belgium). For reconstruction, a threshold of greyscale values must be selected that fully capture the data being performed. The associated crop size and corresponding analysis are listed in Table 3-3. For the greyscale and particle quantification and distribution analysis, the data for each sample was cropped down to a size of 128 x 128 x 128 voxels or a physical volume of 0.09 mm<sup>3</sup>, which corresponds to the maximum correlation window size from FIDVC. While, it is expected and indeed desired for there to be some variation in greyscale intensity and particle distribution, as long as there is not any observable agglomeration of particle a single correlation window is sufficient for a preliminary assessment of image quality and general trends. Additionally, in the next test a larger volume of interest is considered which in doing so will capture the effect of variation in greyscale and particle distribution.

For the numerical translation error analysis, the data was cropped down to a size of 832 x 832 x 832 (6.5 correlation window size). The full resolution analysis was cropped to a size of 898 x 898 x 768 voxels to allow for the entire region surrounding the hole to be analyzed. For the reduced resolution dataset, the crop x-resolution and y-resolution were kept the same as the first full resolution dataset analysis. However, to increase the size of the volume of interest the data was



first resized by 1/3 utilizing an image segmentation and visualization software package (CTAn, 1.16.90, Bruker, Belgium).

Table 3-3: Image sizes utilized for DVC measurements

DVC Measurement	Data Size (voxel x voxel x voxel)
Greyscale and Particle Measure	128 x 128 x 128
Numerical Translation	832 x 832 x 832
Full Resolution Epoxy with Embedded Hole	898 x 898 x 768
Reduced Resolution Epoxy with Embedded Hole	898 x 898 x 980

### ***3.2.4 Contrast, Particle Distribution and Cross-Correlation Measurement***

To determine the optimal particle size and material for DVC analysis, the contrast and distribution of particles throughout the sample must be first quantified. To quantify the contrast and particle distribution, a single subset was selected from the center of the sample with a size of 128 x 128 x 128 voxels, corresponding to the maximum correlation window size. The contrast can be quantitatively measured by comparing the greyscale counts for a single correlation window for each sample. Then to quantify the particle distribution on a subset level, the same subset was segmented through a commercial CT segmentation software (CTAn, 1.16.90, Bruker, Belgium). This allowed distinct greyscale features (particles) within the subset to be located and quantified.

For examination of the distribution of particles within a single correlation window, particles were segmented from the epoxy and then counted digitally. To analyze the segmented particles, the data set was first converted to a binary image. Table 3-4 shows the threshold values for each dataset. Due to the aluminium oxide greyscale pattern it was difficult to distinguish the particles from the epoxy resin and were not possible to segment out of the image; thus, the particle distribution study was not conducted for this dataset. The particles within each sample and the

position of their centroids were then calculated within the correlation window via the 3D image analysis function of the utilized segmentation software.

Table 3-4: Greyscale thresholds utilized for particle segmentation

Particle	Greyscale Threshold
200 $\mu\text{m}$ Copper	33-255
50 $\mu\text{m}$ Copper	33-255
25 $\mu\text{m}$ Copper	33-255
50 $\mu\text{m}$ Zirconium (IV) Oxide	35-255

To validate this analysis for a DVC study, it is vital to gauge the degree of similarity between a reference and a deformed dataset. The zero normalized cross-correlation coefficient ( $\text{ZNCC}_{ijk}$ ) provides a measure of similarity between two subsets on a scale of 0-1 [3]. Equation 3.1 presents the formula for the  $\text{ZNCC}_{ijk}$  where the greyscale intensity at a point in the undeformed subset and deformed subsets are represented by  $F(x_i, y_j, z_k)$  and  $G(x_i^*, y_j^*, z_k^*)$  respectively. In this equation,  $F_m$  and  $G_m$  represent the mean greyscale value of the undeformed and deformed subsets. To get an accurate measure of the effects of each particle on the  $\text{ZNCC}_{ijk}$ , a deformed dataset was created by artificially displacing each subset by the same amount. Utilizing the aforementioned segmentation software, each  $128 \times 128 \times 128$  subset was artificial displaced 10 voxels (35  $\mu\text{m}$ ) in the x-direction through the utilization of a geometrical transformation. This displacement was chosen based on a similar study for 2D DIC and as it is of the same magnitude of displacement that the compressed epoxy coupon is expected to experience [26]. The  $\text{ZNCC}_{ijk}$  between this artificially displaced data set and reference data set was then calculated through an open-source MATLAB based code [32].

$$\text{ZNCC}_{ijk} = \frac{\sum_i \sum_j \sum_k \{F(x_i, y_j, z_k) - F_m\} \{g(x_i^*, y_j^*, z_k^*) - G_m\}}{\sqrt{\sum_i \sum_j \sum_k \{F(x_i, y_j, z_k) - F_m\}^2 \sum_i \sum_j \sum_k \{f(x_i^*, y_j^*, z_k^*) - G_m\}^2}} \quad (3.1)$$

### **3.2.5 Digital Volume Correlation**

A MATLAB based DVC software package (FIDVC, version 1.2.4) was utilized to calculate the in-situ 3D deformation [29]. The software discretizes a 3D volume into a series of user-defined square subsets. Correlation is performed within these subsets between the reference and displaced image datasets to determine the relative change between them. To improve the resolution on the displacement, FIDVC utilizes an iterative approach where the subsets, or correlation window, become smaller between iterations. In addition to the subset size, the subset spacing between the centers of adjacent subsets must be chosen to determine the overlap. It is thus critical to select an initial subset size and node spacing to allow for the best accuracy for displacement and strain.

### **3.2.6 Artificial Displacement Error Calculations**

To determine seeding particle that provides the highest degree of accuracy, a full resolution subvolume of the sample equal to  $832 \times 832 \times 832$  voxels was artificially displaced by 10 voxels in the x-direction. The undeformed and artificially displaced datasets were then input into the DVC software and correlated to determine both the optimal input parameters and seeding particle. This was done in two stages. First, the effects of subset size (correlation window) were taken into consideration. Each particle was correlated at 3 different subset sizes  $32 \times 32 \times 32$  voxels,  $64 \times 64 \times 64$  voxels, and  $128 \times 128 \times 128$  voxels. Due to the iterative nature of the software, each pass would reduce the size of the subset and thus not give a true measure of the displacement at that correlation window size. This was circumvented by setting the max iteration to 2, which forces the software to only pass through the data once. The mesh spacing was set to 50% of the subset size as recommended for the software, of note this was later tested to ensure 50% was optimal for the particles utilized in this study [29]. The remaining correlation parameters were left to the recommended default values of the software and are shown in Table 3-5. After correlation, the

results were compared with the digital displacement to measure the accuracy at replicating the 10 voxel displacement.

Table 3-5: Correlation parameters used with FIDVC for subset and artificial displacement accuracy test

Correlation Parameter	Value		
Subset Size	128 x 128 x 128	64 x 64 x 64	32 x 32 x 32
Mesh Spacing	64	32	16
Max Iteration	2		
Overlap	50%		
Convergence Criteria	0.25,0.5,0.0625		
Cross-Correlation Threshold	0.0001		

After measuring the error results produced from the subset test, the effects of overlap on accuracy was determined. To measure the overlap error, both the subset and particle that provided the most accurate measure of displaced from the first stage were held constant while varying the overlap. It is important to note that the subset selection process was based upon the relatively small and simple deformation expected to see within our epoxy resin. This same reason is used for selection of the sample overlap. For these measurements, overlaps of 25%, 50%, and 75% were utilized. The remaining correlation parameters are left to their defaults, are shown in Table 3-6.

Table 3-6: DVC parameters utilized to determine optimal overlap between subsets

Correlation Parameter	Value		
Subset Size	128 x 128 x 128		
Mesh Spacing	64		
Max Iteration	2		
Overlap	25%	50%	75%
Convergence Criteria	0.25,0.5,0.0625		
Cross-Correlation Threshold	0.0001		

### **3.2.7 Effects of Data Downsampling**

To address one of the significant challenges with DVC, large data sets leading to an intensive computational burden, the effects of downsampling were studied. The data chosen for this test was the 25  $\mu\text{m}$  copper particles, which was demonstrated as the most accurate from the previous two experiments. To replicate the effects of the procedure that would be utilized for DVC experimental measurement, the  $\mu\text{-CT}$  data was first shifted at full-resolution by 35  $\mu\text{m}$  (10 voxels) in the positive x-direction. Samples were then downsampled by 1/3 their full resolution utilizing the previously mentioned CT image segmentation and visual analysis software (CTAn, 1.16.90, Bruker, Belgium). The samples were then cropped to a size of 832 x 832 x 832 so that a direct comparison could be made with the results from the full-resolution artificial displacement tests. Samples were correlated according to the same setting shown in Table 3-5, so that a direct comparison of results could be made.

### **3.2.8 DVC Displacement and Strain**

After determining the optimal correlation parameters, the epoxy sample with the embedded hole was mechanically compressed, and the displacement field and strain fields for the sample were calculated at both full and downsampled resolutions. The displacement and correlation strength are calculated through Fast Fourier Transform (FFT) approach which performs the cross-correlation and track the movement of the imbedded copper particles from the reference. Full-field Lagrangian strain measurements were then calculated from the displacement fields using a software extension (LD-3D-TFM, version 1.1) [30]. The formulation for the lagrangian strain measurement is shown in equation 3.2. In conjunction with the cross-correlation and iterative deformation, the method is used to improve the accuracy of the displacement.

Correlation for the mechanical tests was done according to the parameter listed in Table 3-7. The parameters here were chosen based on the optimal setting from the artificial displacement test. Of note for the epoxy coupon, the maximum iterations were set to 5, to take advantage of added accuracy provided from the iterative nature of the software, while ensuring the final subset was set to 32 x 32 x 32. Additionally, the mesh spacing was set to 16 voxels, which is 50 % of the final subset size to ensure there is no super-sampling or sub-sampling of the data.

The DVC measurement was performed by first saving the image stacks as a 3D matrix with the MAT file extension. Correlation for the four displacement fields calculated: displacement in x, y, z, and displacement magnitude, are then calculated via the FIDVC software. Displacement fields were then uploaded into the strain software package to calculate the 3D strain fields. Six unique values of strain are measured from this procedure: three normal strain and three shear strain according to the 3D strain matrix seen in equation 3.3. The equivalent strain field was then converted into equivalent Von-Mises strain according to equation 3.4 [33]. The Von-Mises strain was utilized since this will provide a strain measure that is independent of the sample coordinate system. Displacement and strain were calculated through the volume of the material and then displayed in three planes, according to Figure 3-3. Computation was performed on a computer (Precision T5600, Dell, Round Rock, Texas) equipped with 112 gigabytes of RAM. Results were visualized utilizing open-source visualization software (ParaView) [34].

$$E_{ij} = \frac{1}{2} \left( \frac{\partial u_i}{\partial x_j} + \frac{\partial u_j}{\partial x_i} \right) \quad i = 1,2,3 \quad j = 1,2,3 \quad (3.2)$$

$$\varepsilon = \begin{bmatrix} \varepsilon_{xx} & \tau_{xy} & \tau_{xz} \\ \tau_{yx} & \varepsilon_{yy} & \tau_{yz} \\ \tau_{zx} & \tau_{zy} & \varepsilon_{zz} \end{bmatrix} \quad (3.3)$$

$$\epsilon_{eq} = \frac{2}{3} \sqrt{\frac{3(\epsilon_{xx}^2 + \epsilon_{yy}^2 + \epsilon_{zz}^2)}{2} + \frac{3(\tau_{xy}^2 + \tau_{yz}^2 + \tau_{zx}^2)}{4}} \quad (3.4)$$

Table 3-7 Correlation parameters used for the compression test on the cylindrical epoxy coupon

Correlation Parameter	Value
Subset Size	128 x 128 x 128
Mesh Spacing	16
Max Iteration	5
Overlap	50%
Convergence Criteria	0.25,0.5,0.0625
Cross-Correlation Threshold	0.0001

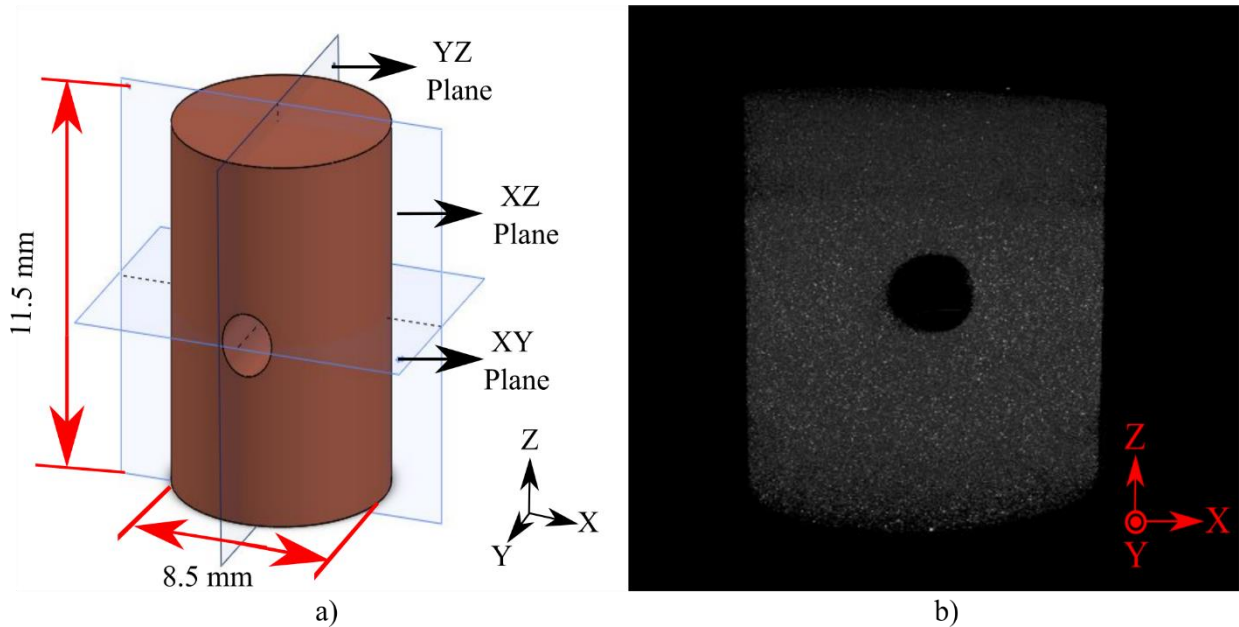


Figure 3-3: 3D Model of the copper impregnated sample: a) Geometrical solid model showing the coordinate planes: i) XY plane, ii) XY plane, & iii) YZ plane, and b) 3D reconstruction of the sample geometry from  $\mu$ -CT tomographs

### 3.3 Results and Discussion

#### 3.3.1 Particle Selection

As previously discussed, the two factors that need to be considered for DVC analysis are the image contrast and the distribution of particles throughout the sample. The greyscale values were measured against the greyscale count on a log scale and shown in Figure 3-4. Across from each histogram is a representative slice from the corresponding dataset. It is important to note here that the tomographic images were intentionally left dark as this represents their true greyscale pattern. This greyscale contrast pattern is what is shown in the second column of Figure 3-4. Thus, the contrast was not enhanced for the tomographs to avoid confusions that may arise when comparing the greyscale patterns to the tomographic image.

To access the contrast pattern, the greyscale count and greyscale value needs to be considered. As can be seen in Figure 3-4, there are two distinct profiles for the greyscale histograms. The first profile is for the aluminium nitride, which represents the closest tomographs to a natural contrast pattern due to its emulsification of the material in the epoxy. The profile for the aluminium nitride shows a classic unimodal greyscale histogram. This profile has been well reported in literature and is shown to generally perform well for 2D DIC and DVC experiments [27], [35], [36]. The copper particles and zirconium (IV) oxide particles show a distinctly different profile. While this profile is not the standard unimodal profile, this has been previously been seen by Pan *et al.* [37]. Pan *et al.* investigated artificially created spackled samples for 2D DIC experiment which had a similar downward sloping greyscale histogram. In these experiments this profile proved to provide a high degree of accuracy. Considering these features each sample contains a sufficient enough greyscale profile that DVC displacement measurements can be conducted between each sample to analyze their accuracy. However, before this can be done the particle distribution should be quantified as this will aid in the underlying displacement accuracy between each sample.



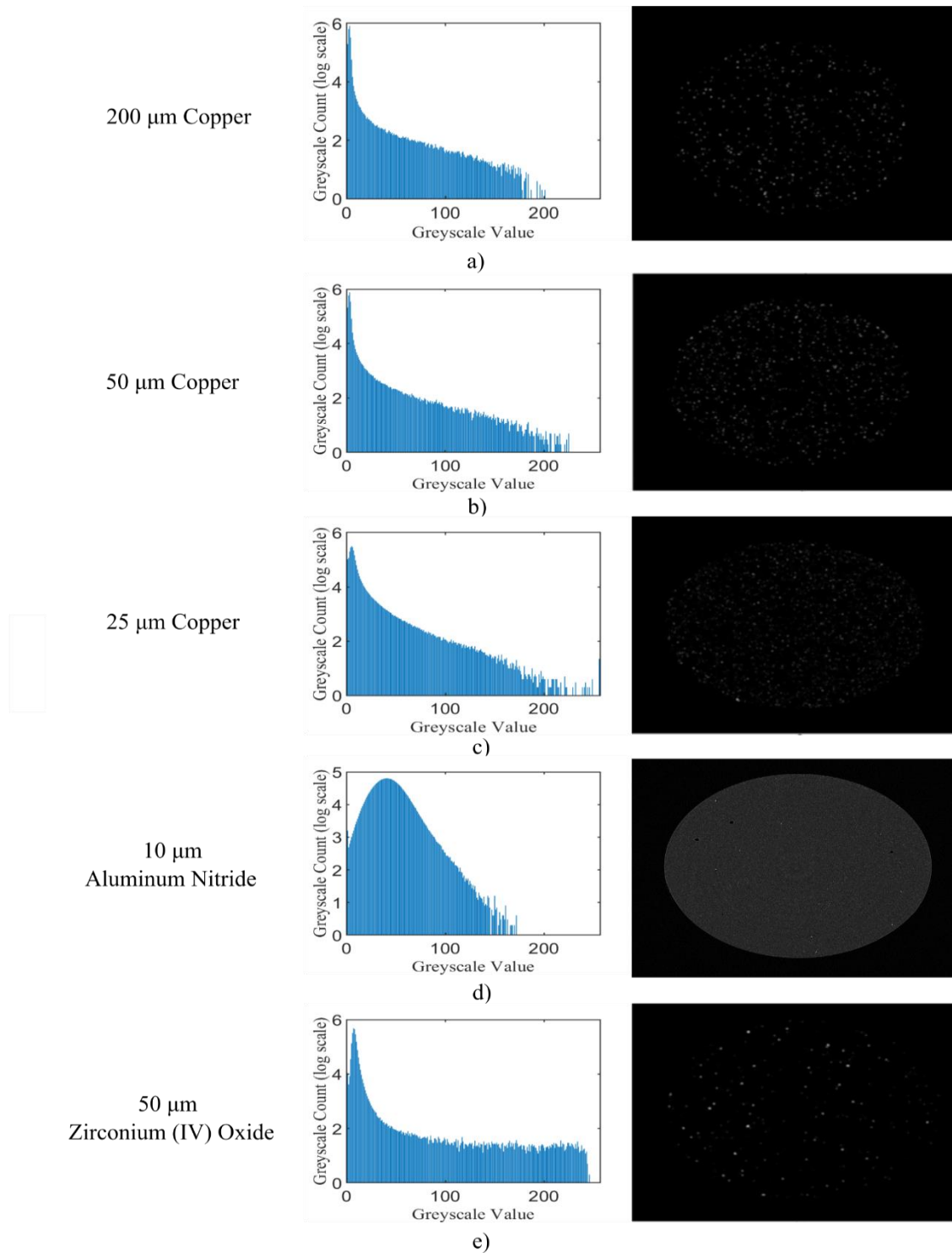


Figure 3-4: Comparison of the greyscale histogram and sample CT Slice: a) 200  $\mu\text{m}$  copper, b) 50  $\mu\text{m}$  copper, c) 25  $\mu\text{m}$  copper, d) 10  $\mu\text{m}$  aluminum nitride, and e) 50  $\mu\text{m}$  zirconium (IV) oxide

To quantify the particle distribution, there are two necessary measures to consider: the number of particles with a correlation window and their location within said window. There are two

possible cases that can form when considering the dispersion of particle within a sample, which are shown in Figure 3-5. Figure 3-5 a) shows the case in which all particle agglomerate in a particular region of the subset set. This case does not lend itself toward proper correlation as the bundling will behave as a single particle within the correlation window. This also may result in subsets devoid of particle entirely within the entire sample, reducing the overall accuracy of results. Figure 3-5 b) demonstrates the ideal case of spackles distributed randomly through the sample. This has previously been shown to provide the highest degree of accuracy for DIC experiments [26].

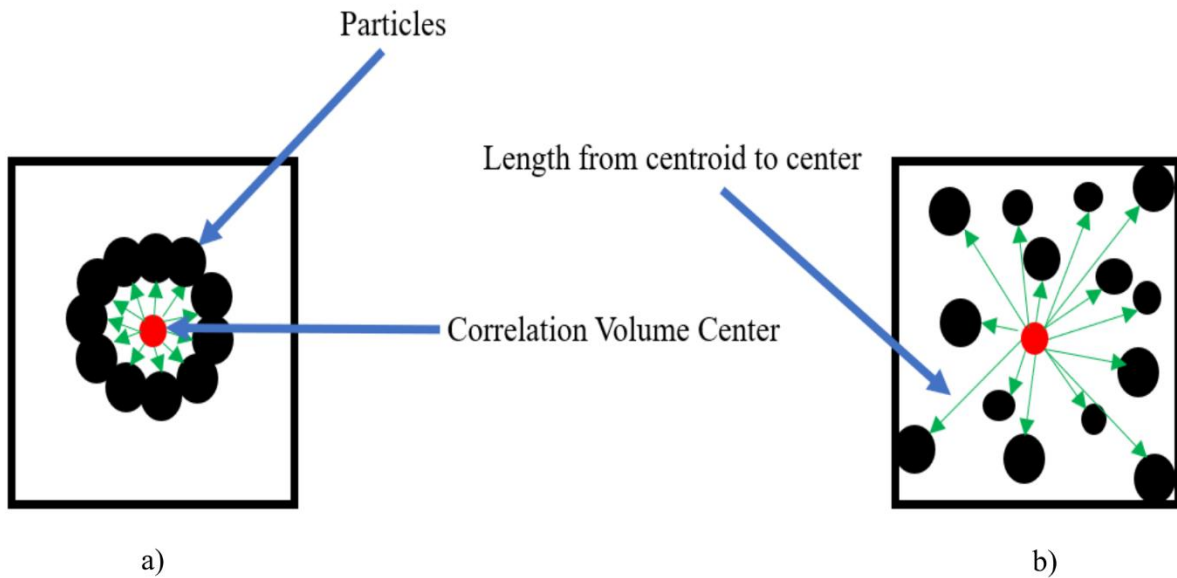


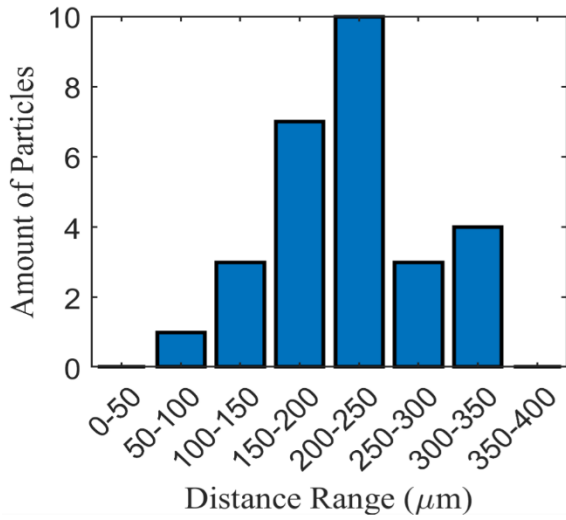
Figure 3-5: 2D representation of the two cases of particle distribution throughout the sample: a) agglomeration of particles within a region, and b) random distribution of particle

To determine the effectiveness of particle seeding the number of particles and their distribution was quantified within a correlation volume. Table 3-8 and Table 3-9 define these two metrics by showing the number of particles within a 128x128x128 correlation-volume and the standard deviation of the distance between their centroid and the center of the correlation window, respectively. As previously discussed, since the aluminium oxide emulsified within the sample it

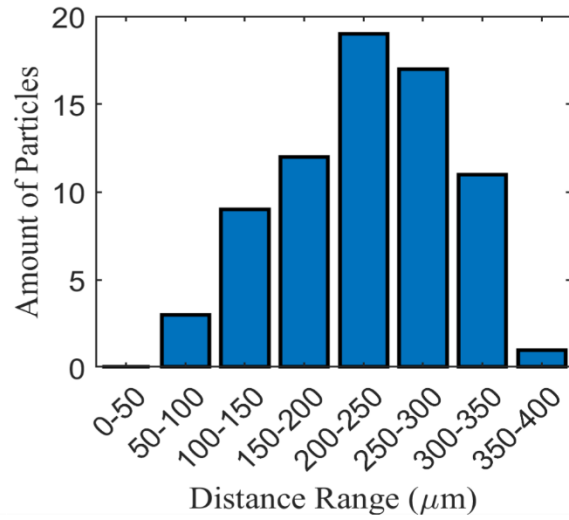
is excluded from this discussion. As a general guideline for DIC/DVC, it has been previously reported and put into practice by Croom *et al.* that any subset should contain a minimum of 27 particles for proper correlation [28]. In Table 3-8, it is evident that each sample meets these criteria, with the 200  $\mu\text{m}$  particles containing only 28 particles, which will be important when discussing the effect of subset size on particle accuracy. To measure the dispersion of particle within the sample, the frequency of particles appearing at differing distances and their variance were measured. It is seen in Figure 3-6 that the particle distances with respect to the center of the correlation window has an approximately normal distribution. This data shows that there is little agglomeration of particles within the correlation windows. To quantify their distribution, the standard deviation of these distances was quantified in Table 3-9. The high standard deviations are seen here show that there is little agglomeration of particles within the correlation windows. Thus, each sample should provide a reasonably accurate correlation for the 128 x 128 x 128 voxel correlation window size.

Table 3-8: Amount of particle within a 128x128x128 subset

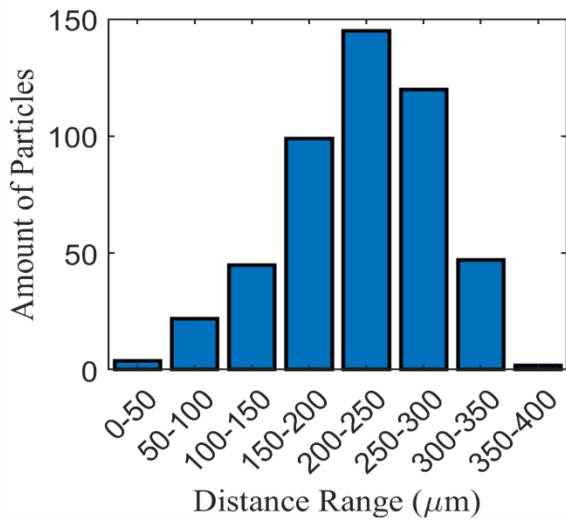
Particle	Quantity of Particles within Correlation	
	Voxel	
200 $\mu\text{m}$ Copper	28	
50 $\mu\text{m}$ Copper	72	
25 $\mu\text{m}$ Copper	484	
50 $\mu\text{m}$ Zirconium (IV) Oxide	87	



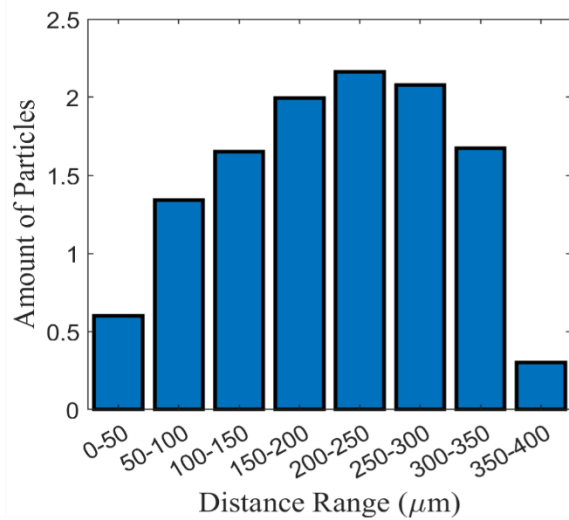
a)



b)



c)



d)

Figure 3-6: Histogram of amount of particles at different distances from correlation window centroid: a) 200  $\mu\text{m}$  copper sample, b) 50  $\mu\text{m}$  copper sample, c) 25  $\mu\text{m}$  copper sample, and d) 50  $\mu\text{m}$  zirconium (IV) sample

Table 3-9: Standard Deviation of the distance between the centroid of the seeding particle and center of the subset

Particle	Standard Deviation of Distance from Center ( $\mu\text{m}$ )
200 $\mu\text{m}$ Copper	60.08
50 $\mu\text{m}$ Copper	68.69
25 $\mu\text{m}$ Copper	65.65
50 $\mu\text{m}$ Zirconium (IV) Oxide	59.10

To determine the effectiveness of particle seeding the number of particles and their distribution was quantified within a correlation volume. Table 3-8 and Table 3-9 define these two metrics by showing the number of particles within a 128x128x128 correlation-volume and the standard deviation of the distance between their centroid and the center of the correlation window, respectively. As previously discussed, since the aluminium oxide emulsified within the sample it is excluded from this discussion. As a general guideline for DIC/DVC, it has been previously reported and put into practice by Croom *et al.* that any subset should contain a minimum of 27 particles for proper correlation [28]. In Table 3-8, it is evident that each sample meets these criteria, with the 200  $\mu\text{m}$  particles containing only 28 particles, which will be important when discussing the effect of subset size on particle accuracy. To measure the dispersion of particle within the sample, the frequency of particles appearing at differing distances and their variance were measured. It is seen in Figure 3-6 that the particle distances with respect to the center of the correlation window has an approximately normal distribution. This data shows that there is little agglomeration of particles within the correlation windows. To quantify their distribution, the standard deviation of these distances was quantified in Table 3-9. The high standard deviations are seen here show that there is little agglomeration of particles within the correlation windows. Thus, each sample should provide a reasonably accurate correlation for the 128 x 128 x 128 voxel correlation window size.

Table 3-10: Zero Normalized cross-correlation coefficients for 128x128x128 voxel displaced by 35  $\mu\text{m}$

Particle	Zero Normalized Cross-Correlation Coefficient
200 $\mu\text{m}$ Copper	0.7879
50 $\mu\text{m}$ Copper	0.7910
25 $\mu\text{m}$ Copper	0.8007
50 $\mu\text{m}$ Zirconium (IV) Oxide	0.6990
10 $\mu\text{m}$ Aluminum Nitride	0.7094

### 3.3.2 Artificial Displacement Error Calculations

#### 3.3.2.1 Effects of varying Subset Size

The measure of the effectiveness of each seeding particle for providing accurate displacement measurements was calculated by correlating the artificially displaced samples and calculating the percentage error between the digital translation and the DVC results. The error results across each sample are shown in Figure 3-7 as varying with each subset size. It can be immediately recognized from the data that as the correlation window or subset size increases, there is a decrease in the error on displacement. This trend of increase accuracy as a result of increasing subset size has been previously seen in experiments by Gates *et al.* [38].

In terms of the effects of particle size on correlation results, when comparing the trends seen between the copper samples, it is evident that as the size of the copper particles decreases, so too does the percentage error. The decrease in error as a result of decreasing particle size has been previously seen within DIC [39], [40]. Smaller particles allow for a more unique correlation pattern present in each correlation window which thus results in a pointier cross-correlation which increases accuracy of the algorithm and makes the data less susceptible to noise. This trend is verified for  $\mu$ -CT and DVC in this study by examining the particle distribution and number of particles within each subset. It was previously shown that while each sample had a similar random distribution between subsets, the 25  $\mu\text{m}$  copper has substantial more particles within each

correlation window, thus increasing the accuracy of the measurement. Both these parameters lead to a more pointy and thus accurate correlation. Indeed, the 25  $\mu\text{m}$  copper seeded samples show the highest degree of accuracy of all seeding particles, making it the optimal choice for seeding a sample for mechanical testing. The remaining tests that will be carried out in this paper are thus done utilizing this dataset.

Of note is the very high degree of error that is present at the smallest subset sizes for the 200  $\mu\text{m}$  copper sample, 50  $\mu\text{m}$  copper sample, 50  $\mu\text{m}$  Zirconium (IV) oxide, and aluminum nitride. This error is likely a result of the amount of particle within each correlation window being below the 27-particle minimum. To quantify this, the particle in 32 x 32 x 32 voxel subset was calculated using the same method presented in section 3.3.1. A subset of 32 x 32 x 32 voxel was cropped from the center of the 128 x 128 x 128 voxel subset, and the amount of particle contained within was then computed. The results from this are shown in Table 3-11. It is seen here that the number of particles within each correlation window is relatively small. The number of particles within each sub-volume for the 200  $\mu\text{m}$  copper sample, 50  $\mu\text{m}$  copper sample, and 50  $\mu\text{m}$  zirconium (IV) oxide are well below the 27 particles which are necessary for an accurate correlation [28]. While this analysis for the aluminum nitride sample could not be performed, the error present is also likely a result of the tomographs not containing enough indicators within to accurately correlate.

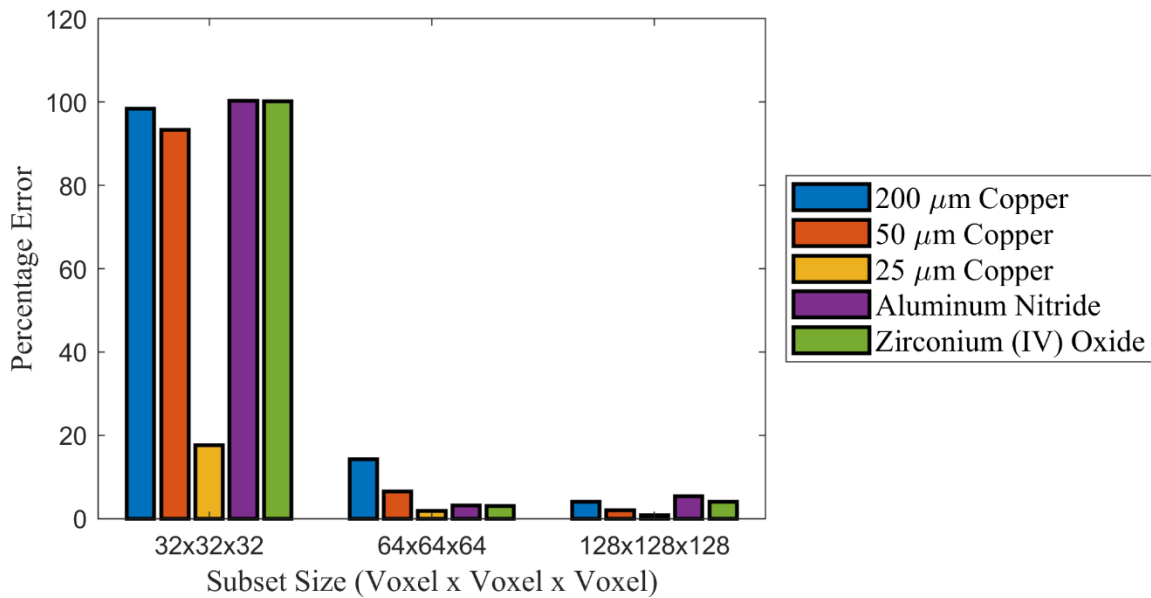


Figure 3-7: Percentage error produced from DVC calculation compared against three standard subset sizes

Table 3-11: Amount of particle within a 32 x 32 x 32 voxel correlation window

Particle	Number of Particles within Correlation Window
200 μm Copper	1
50 μm Copper	3
50 μm Zirconium (IV) Oxide	3

### 3.3.2.2 Effects of varying overlap

The effect of subset overlap was measured using the 25 μm copper, which proved to be the most accurate measurement of displacement. It is evident from Figure 3-8 that the effect of overlapping does not have a significant effect on mean accuracy as the correlation window size. The range of errors shown in this data only ranges from 2.372%-0.887%. However, when considering the variance between each dataset only the 50 % and 75 % dataset have what would be considered a reasonable range of variance which are 0.883 % and 1.24% respectively. There is a very clear break down in result reliability when correlation windows are overlap at 25%. This is likely a result of a insufficient region of comparison to capture displacement. Nevertheless, the



optimal subset overlap is 50%. This agrees with previous data reported by Gates *et al.*, that shown a 50% overlap as providing the highest accuracy toward displacement [41]. Thus, this analysis can confirm the optimal input parameter for the mechanical test. Additionally, the fact that both the effects of subset size and overlap show similar trends to data already seen in DVC studies and show a low degree of error demonstrates the effectiveness of the seeding pattern provided by the 25  $\mu\text{m}$  copper samples.

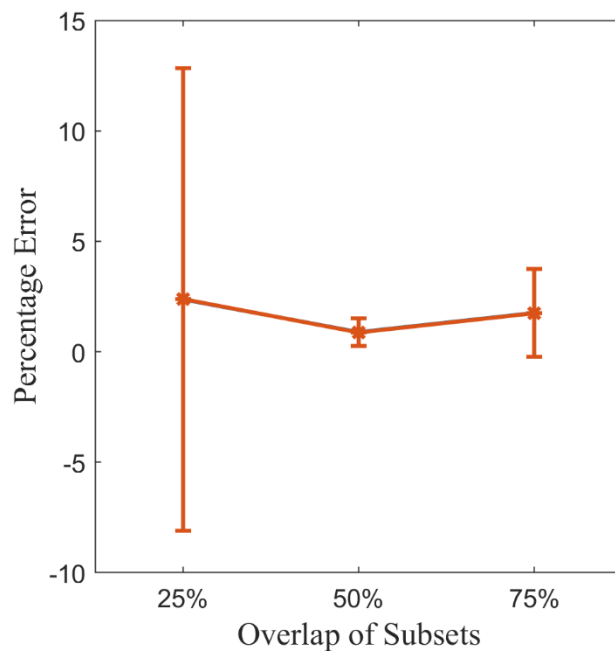


Figure 3-8: Effect of percentage overlap of subsets on overall accuracy

### 3.3.2.3 Effects of downsampling

To address the computational burden of the data set, the numerically displaced data was reduced by a third of its original resolution, and the resulting errors were observed. The effects of the resolution reduction are shown in Figure 3-9. While the overall trend has remained the same, the effects of downsampling introduced a non-insignificant amount of error. Within this figure the mean displacement and variance in results is plotted for the 128 x 128 x 128 voxel, the 64 x 64 x

64, and the 32 x 32 x 32 voxel correlation window for both the full resolution, and reduced resolution dataset. Due to the reduced resolution data including some black space around the outer area of the sample a border of 1.34 mm was removed from the results to unbiased the displaced data.

Comparing Figure 9 a) to Figure 9 b) by reducing the resolution of the dataset there is an accompanying increase both the accuracy of the program to capture the 35 voxel displacement and variance in displacement captured. For the full-resolution data error is between 17.75%-0.887% while for the reduced resolution dataset is 14.3%-7.682%. In addition to the increased error over each subset the full-resolution data shows very minimal variance in displacement data at the 128 x 128 x 128 voxel, and 64 x 64 x 64 voxel correlation window, while the reduced resolution shows increased standard deviation across all correlation windows. This error and variation are likely due to the 35  $\mu\text{m}$  displacement of particles being more difficult to capture in a correlation window size that has triple in size from 0.448 x 0.448 x 0.448 mm to 1.344 x 1.344 x 1.344 mm.

While this amount of error and variation may prevent a truly a precise and accurate measure of the displacement of the sample to be made, this data could still prove useful when performing a mechanical test. As a direct result of downsampling the data, a higher region of the sample can be analyzed without significantly increasing the computational burden. It is thus possible that the entire sample can be analyzed at a reduced resolution allowing for a general sense of the response of the sample to a mechanical load to be observed before doing full resolution measurement on regions of interest for accurate measurement. This methodology will be put into effect and analyzed when observing the effects of the compression test on the copper seeded epoxy sample.

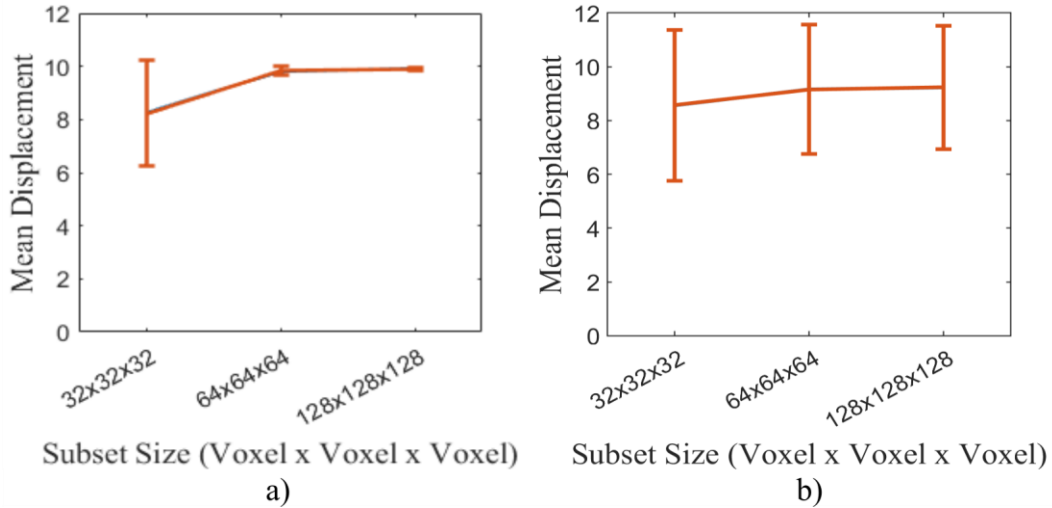


Figure 3-9: Error produced as a result of down sampling numerically displaced data: a) full resolution dataset, b) 1/3 reduced resolution dataset

### 3.3.3 Sample Displacement

By utilizing the data from the particle selection study and input parameter analysis, it became possible to select an optimal seeding particle and overlap for DVC analysis. A new sample was then prepared, and the DVC measurement technique was utilized to provide full-field measurements of the displacement and strain development from the compressive load applied in this study. The axial displacement measured in micrometres is shown in the yz-plane and xy-plane are shown in Figure 3-10 at the reduced resolution. In regard to the isometric view, a clip is shown to display the internal displacement behaviour of the sample. It can be seen in Figure 3-10 that the displacements there is no displacement along the 2 mm hole. From this point, the displacement radiates outward equivalently from the center hole of the samples. This even displacement seen is a result of direct uniaxial compression of the specimen. Figure 3-10 b) the displacement is shown in the yz-plane, which gives a clear view of the displacement field. The pattern of the field of displacement seen in the yz-plane is similar to that which can be seen from other compression

studies of the hole in sample designs [42]. This view clearly shows three bands of displacement within the sample.

The first band of displacement is shown at the bottom of the sample describing a displacement along the z-direction at the compression end. There are then two bands of displacement that radiate outward from the hole in the bulk of the material. The final region of displacement is at the top of the sample along the static end. While it is expected for there to be 0 displacement in this region, the displacement seen is between the 0 to  $-14\ \mu\text{m}$  range. This displacement is likely a result of a lack of rigidity in the MTS, resulting in some bulk movement of the sample near the static end. Viewing the xy-plane of the sample shown in Figure 3-10 c), there is minimal variation in displacement, and the bulk of the material translates. The results shown in Figure 3-10 demonstrate that the bulk deformation of the test sample can be measured using the DVC analysis technique. Additionally, the particle seeding technique has proven effective at detecting sub-millimetre levels of displacement from the applied loading.

Measurement of the actual displacement on the sample was done through an additional DVC study at full resolution. A section of the sample equal to  $898 \times 898 \times 768$  voxels was taken around the hole of the sample and analyzed utilizing the same DVC parameters. The results of this measurement are shown in Figure 3-11. A small trim around the dataset was performed to display only the displacement within the bulk of the sample and not capture the data at the artificially cropped edges. Indeed, the effect of downsampling of the data has an observable effect on the resolution of the displacement field. Comparing the data shown in Figure 3-10 compared to that in Figure 3-11, not only is the displacement field less detailed but as previously discussed of slightly higher displacement due to the introduction of error. Importantly, however, there is not a significant difference between the overall pattern of displacement between the downsampled data

and full-resolution data. It is thus possible to use the reduced resolution dataset to get a general idea of the overall displacement pattern and regions of interest and then utilize the full-resolution data to obtain an accurate portrayal of displacement within specific regions.

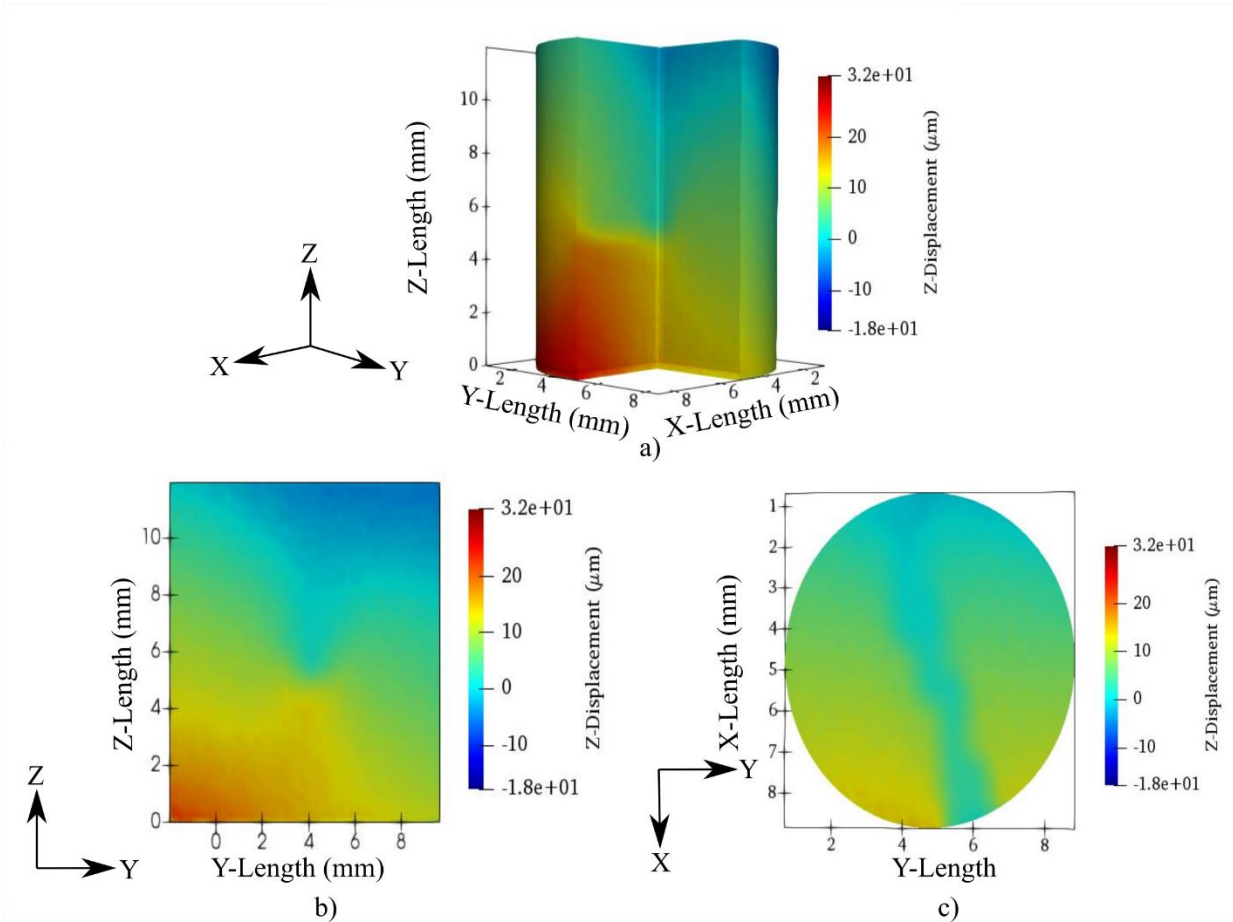


Figure 3-10: Views of displacement of the sample along the direction of compression: a) isometric view, b) yz plane, and c) xy plane

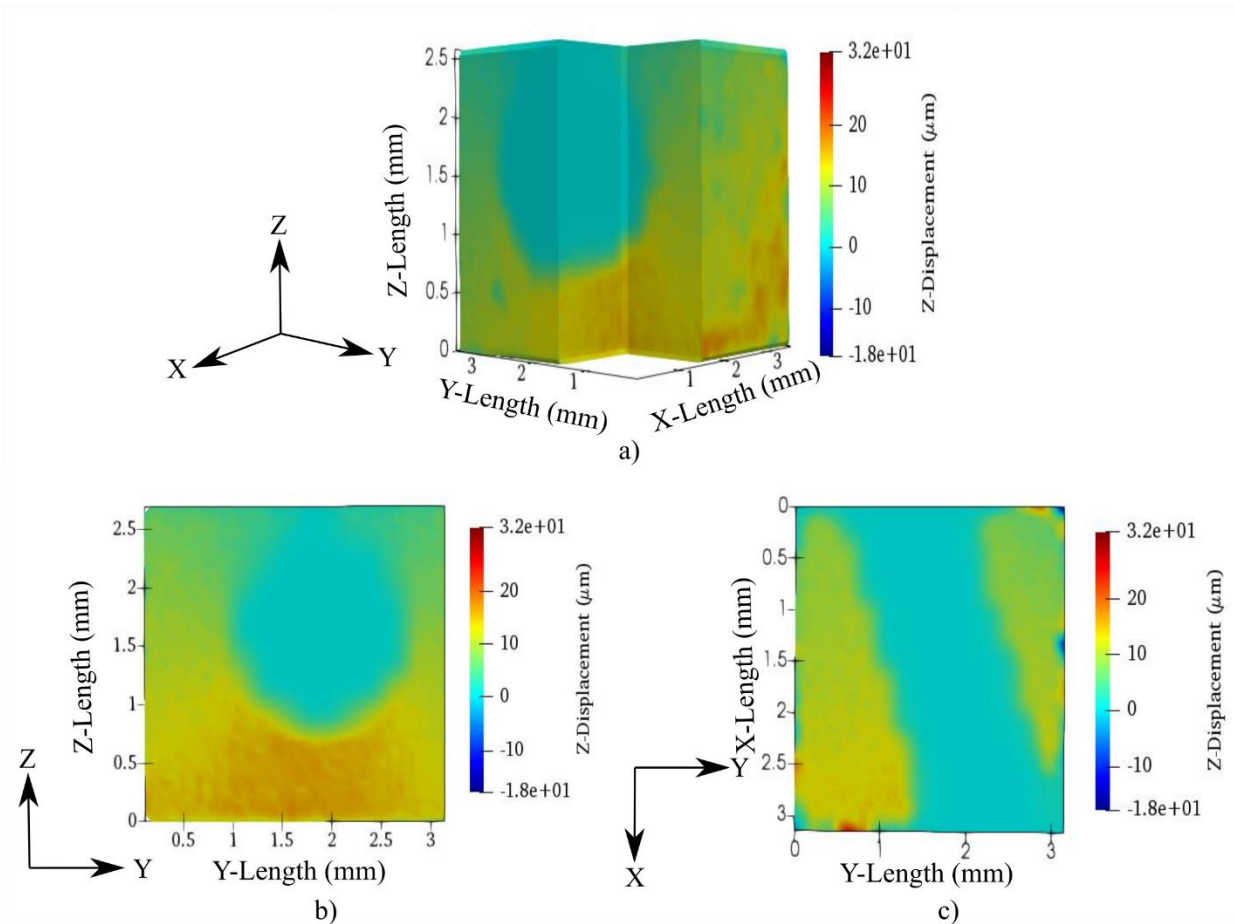


Figure 3-11: Views of displacement of the full resolution sample along the direction of compression: a) isometric view, b) yz-plane, and c) xy-plane

### 3.3.4 Strain Data

Along with the displacements, the equivalent Von Mises strain calculated for the full geometry of the epoxy resin and is shown in Figure 3-12. Figure 3-12 shows the Von Mises strain in the isometric view, yz-plane and xy-plane. From the xy-plane shown in Figure 3-12 c), the development of strain through the resin can be seen to form at the edge of the 2 mm hole. At the edge of the hole, it is expected that a region of high strain exists as the hole act as a concentration for high stress. Throughout the bulk of the material, there exists minimal to 0 strain. At the outer surface of the material, another high region of strain exists. At this point, it is essential to recognize that DVC software and strain extension are not optimized for strain measurements, but rather

displacement and traction force measurements. Thus, it is likely that the strain being captured on the surface of the cylinder is a result of the rigid body motion of the sample and poorer correlation that occurs at the border of the sample known as DVC edge effect. This rigid body motion, as previously discussed, is likely due to movement in the sample due to the MTS lack of rigidity. This lack of rigidity in the MTS could result in some unwanted sway or movement in the sample during loading which has already been seen in Figure 3-10. Figure 3-13 shows a visualization of the strain with the edge effects removed from the sample. By removing the edge effects, the strain around the center hole is highlighted within the sample and is shown to be less biased by the edge effects varying the colour scale. The surrounding strain around the hole for the reduced resolution is shown to have a two stage gradient 0.018-0.04 ( $\mu\text{m}/\mu\text{m}$ ).

As was done in the displacement study, a correlation at full resolution taking a region around the hole was performed. Figure 3-14 shows the result of the strain distribution around the hole of the sample along three viewing planes. What is immediately evident from this data is that the strain field around the center hole is more well defined than in the down-sampled data shown in Figure 3-12. The development of a concentric ring of equivalent strain around a hole has been previously seen for uniaxial loading by Yoon *et al.* [43]. In Figure 14 d), the strain along two lines crossing the sample through the y-axis and z-axis has been plotted. The normal development of strain increasing approaching the perimeter of the hole before decreasing to 0 at the center can be seen as plotted along both axes. The strain around the hole ranging between 0.02-0.1 ( $\mu\text{m}/\mu\text{m}$ ), with only slight variations when plotted along both axes in the magnitude of strain.

This methodology demonstrates the advantage of utilizing the full-resolution dataset in conjunction with a down-sampled dataset. The downsampled dataset has the advantage of providing a relatively accurate portrayal of how the development of strain happens within the full

bulk of the material. With this methodology, it is possible to locate a region of high strain, and then utilize the full-resolution dataset to investigate the behaviour of strain within these regions. Such was shown in Figure 3-14, where the perpetration of stress around the hole is shown in greater detail. These results demonstrate the capability of the seeding technique in combination with  $\mu$ -CT imaging and DVC for capturing the inner strain behaviour epoxies. These techniques can be extended toward full-field strain measurement of more complex composite materials.

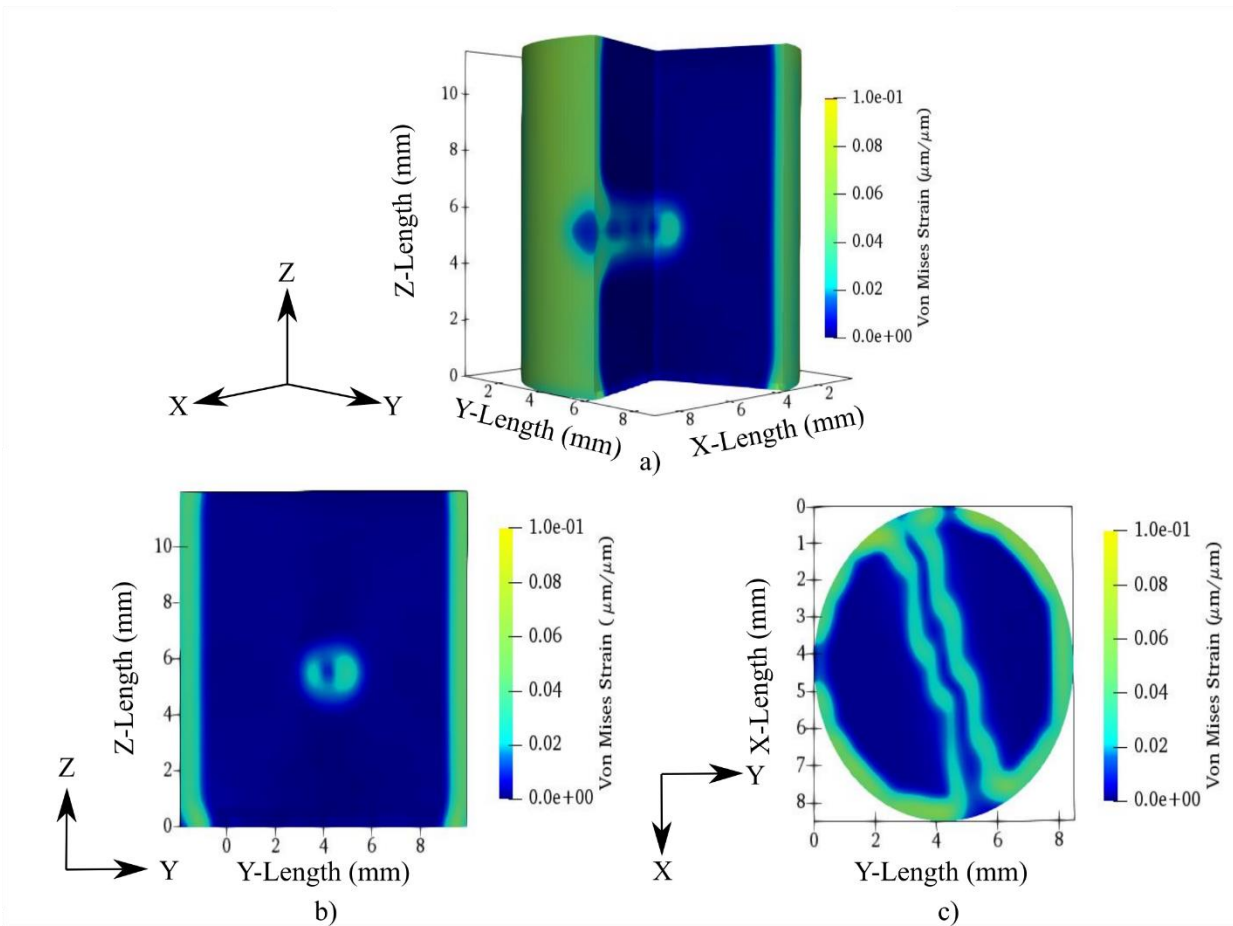


Figure 3-12: Equivalent Von Mises strain for the down-sampled epoxy sample subjected to compressive loading: a) Isometric View b) yz-plane and c) xy-plane.



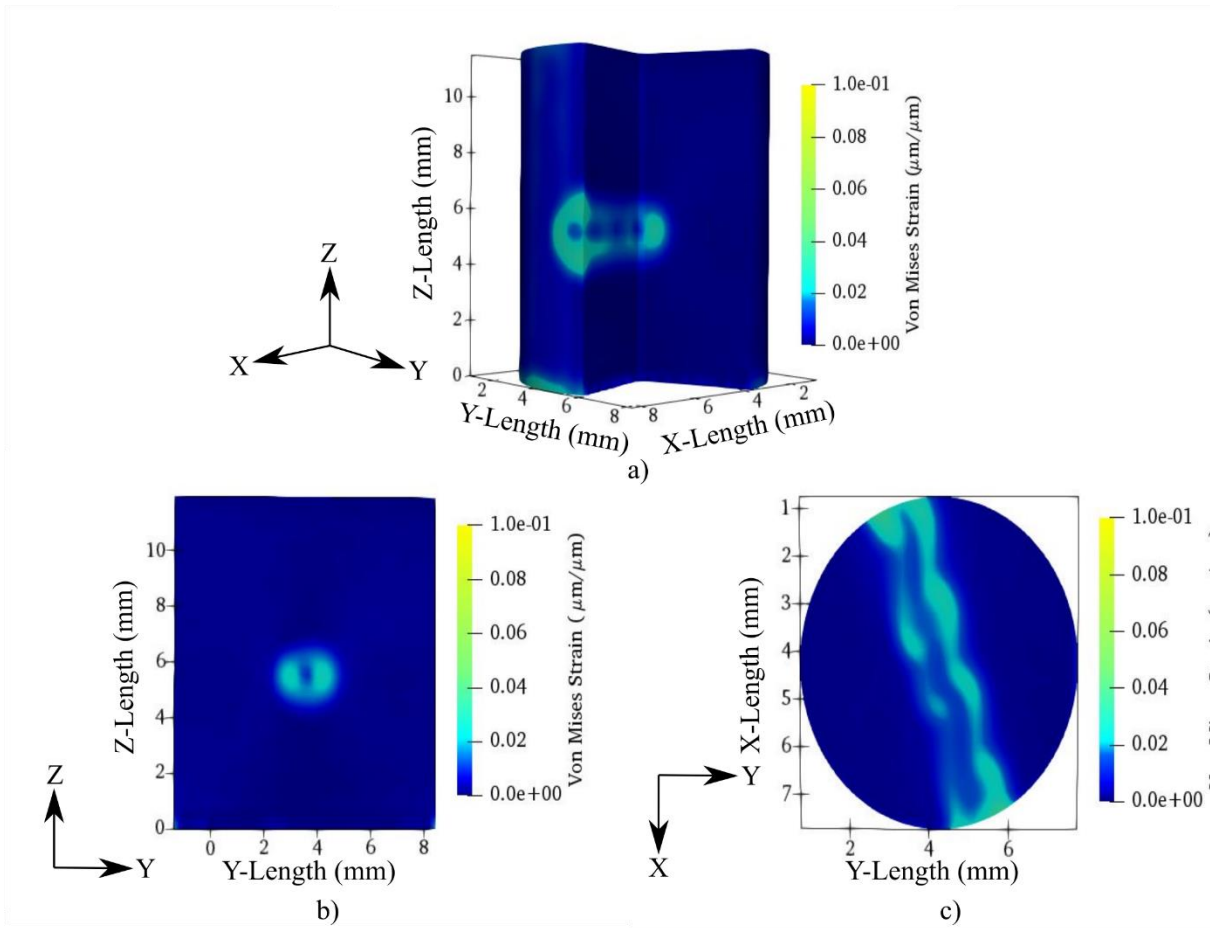


Figure 3-13: Equivalent Von Mises strain for the down-sampled epoxy sample subjected to compressive loading with edge effect removed: a) Isometric View b) yz-plane and c) xy-plane

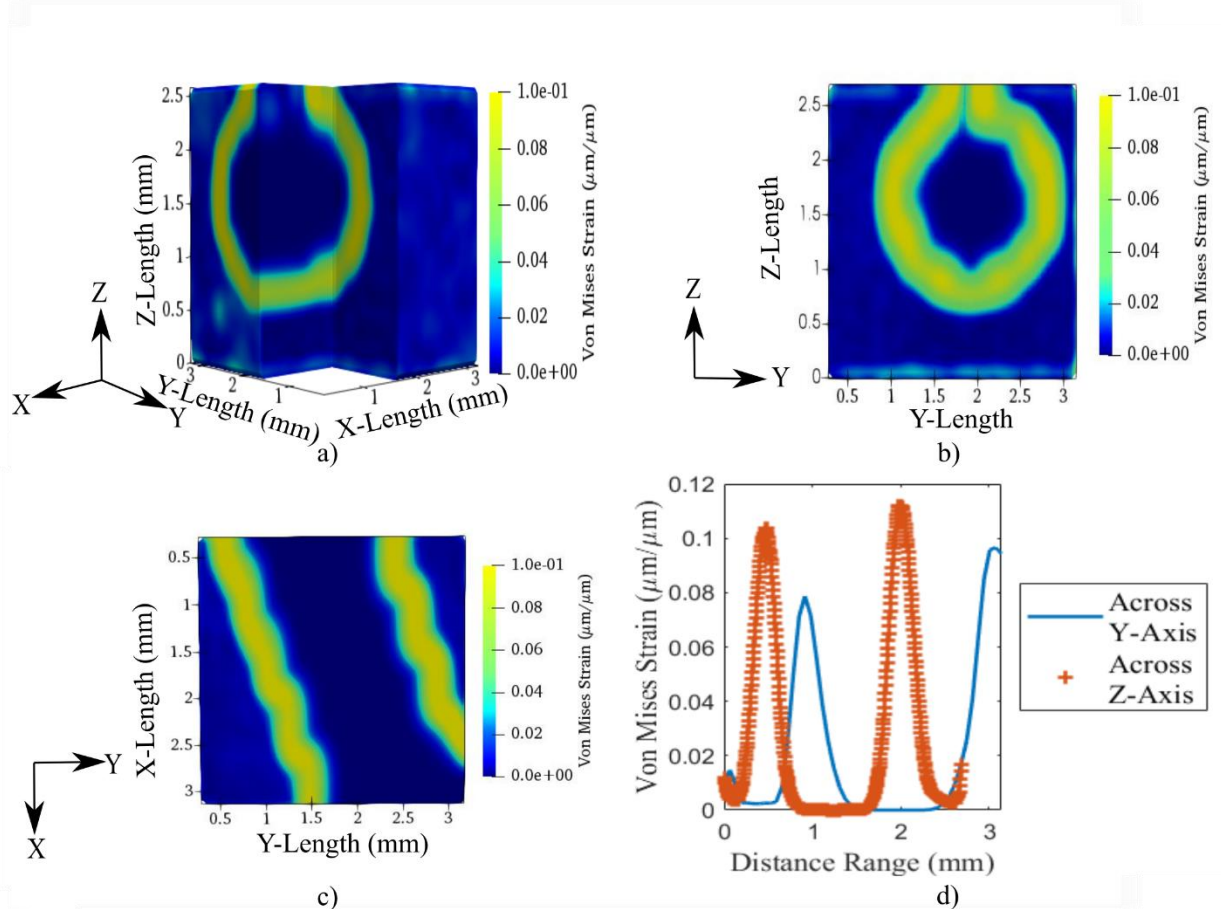


Figure 3-14: Equivalent Von Mises strain for the full-resolution epoxy sample subjected to compressive loading: a) Isometric View, b) yz-plane, c) xy-plane view and d) strain across y-axis and z-axis of hole

### 3.4 Conclusion

In this study, a particle seeding technique was utilized to improve the image contrast of tomographic images for DVC measurements. An epoxy resin was seeded with five different particles at a 5wt% ratio to epoxy: 200  $\mu\text{m}$  copper, 50  $\mu\text{m}$  copper, 14-25  $\mu\text{m}$  copper particles, zirconium (IV) oxide ( $\text{O}_2\text{Zr}$ ), and aluminium nitride. A 3D image stack was obtained via  $\mu\text{-CT}$  for each seeded epoxy to assess their quality for DVC. The particles were then analyzed for greyscale contrast, particle distribution, and correlation accuracy to determine the best seeding particle. Utilizing a  $\mu\text{-CT}$  segmentation technique, the number of particles and their greyscale contrast within a single correlation window was determined. These factors showed that each particle should

be utilizable for DVC comparison. To selected between particles, each dataset was numerically displaced by 35  $\mu\text{m}$  and correlated with its original dataset to determine the most accurate seeding particle. Considering these factors, the 14-25  $\mu\text{m}$  copper particles was determined the optimal seeding particles.

For the DVC measurement, a reference and deformed state was required for displacement and strain measurements. An integrated testing stage within the  $\mu\text{-CT}$  allowed for the performance of in-situ compressive loading at forces of 100 N and 300 N. Resultant displacement and strain fields for the test sample was demonstrated. Displacement and strain were computed using an open-source DVC software package. To address the computational burden associated with DVC measurement, two studies were conducted. A first study was done by analyzing the sample at a third of their original resolution to determine the overall displacement behaviour. Then a second study was conducted around the hole of the sample at full resolution to obtain accurate details on the strain and displacement around the sample hole.

The measurement technique allowed for the volumetric visualization of both the bulk movement of the epoxy and the equivalent strain. Displacements were shown to develop in 3 bands similar to what has previously been discussed in other holes-in sample compression tests. The equivalent volumetric strain displayed two regions of high strain through the sample. The first region of strain is present along the radius of the inner hole having a strain in the range of 0.02-0.1  $\mu\text{m}/\mu\text{m}$ . The second region of strain is occurred along the outer surface of the sample. The more considerable strain present on the perimeter of the sample is likely due to poor rigidity with the MTS and sample edge effects. This lack of rigidity likely caused possible sway in the sample while being compressed and scanned by the  $\mu\text{-CT}$ . To investigate further into the displacement and strain behaviour around the hole of the sample a VOI of interest was selected around it. By utilizing the

full-resolution dataset, it was evident this resulted in a better view of both the strain and displacement field. The full-resolution data demonstrated the advantage of utilizing first a down-sampled dataset to investigate regions of high strain within the sample and then utilizing a full-resolution data set to investigate in detail around these regions. The particle seeding method used in this work was demonstrated to be a useful technique for enhancing the image contrast for DVC results. This is a critical first step towards the measurement and investigation of volumetric deformation and strain of braided, laminated or textile structures.

### 3.5 References

- [1] A. K. Kaw, *Mechanics of composite materials, second edition*. 2005.
- [2] C. K. Leung, G. W. Melenka, D. S. Nobes, and J. P. Carey, “The effect on elastic modulus of rigid-matrix tubular composite braid radius and braid angle change under tensile loading,” *Compos. Struct.*, vol. 100, pp. 135–143, Jun. 2013.
- [3] B. Pan, K. Qian, H. Xie, and A. Asundi, “Two-dimensional digital image correlation for in-plane displacement and strain measurement: A review,” *Meas. Sci. Technol.*, vol. 20, no. 6, 2009.
- [4] G. W. Melenka and J. P. Carey, “Experimental analysis of diamond and regular tubular braided composites using three-dimensional digital image correlation,” *J. Compos. Mater.*, vol. 51, no. 28, pp. 3887–3907, 2017.
- [5] O. De Almeida, F. Lagattu, and J. Brillaud, “Analysis by a 3D DIC technique of volumetric deformation gradients: Application to polypropylene/EPR/talc composites,” *Compos. Part A Appl. Sci. Manuf.*, vol. 39, no. 8, pp. 1210–1217, 2008.
- [6] M. Kashfuddoja and M. Ramji, “Whole-field strain analysis and damage assessment of adhesively bonded patch repair of CFRP laminates using 3D-DIC and FEA,” *Compos.*

- Part B Eng.*, vol. 53, pp. 46–61, 2013.
- [7] M. A. Sutton, J. H. Yan, V. Tiwari, H. W. Schreier, and J. J. Orteu, “The effect of out-of-plane motion on 2D and 3D digital image correlation measurements,” *Opt. Lasers Eng.*, vol. 46, no. 10, pp. 746–757, 2008.
- [8] W. Tong, “An evaluation of digital image correlation criteria for strain mapping applications,” *Strain*, vol. 41, no. 4, pp. 167–175, 2005.
- [9] S. K. Boyd, “Micro-computed tomography,” in *Advanced Imaging in Biology and Medicine: Technology, Software Environments, Applications*, 2009, pp. 3–25.
- [10] G. W. Melenka, E. Lepp, B. K. Cheung, and J. P. Carey, “Micro-computed tomography analysis of tubular braided composites,” *Compos. Struct.*, vol. 131, pp. 384–396, 2015.
- [11] H. Bale, M. Blacklock, M. R. Begley, D. B. Marshall, B. N. Cox, and R. O. Ritchie, “Characterizing three-dimensional textile ceramic composites using synchrotron x-ray micro-computed-tomography,” *J. Am. Ceram. Soc.*, vol. 95, no. 1, pp. 392–402, 2012.
- [12] J. J. Orteu, “3-D computer vision in experimental mechanics,” *Opt. Lasers Eng.*, vol. 47, no. 3–4, pp. 282–291, 2009.
- [13] B. K. Bay, T. S. Smith, D. P. Fyhrie, and M. Saad, “Digital volume correlation: Three-dimensional strain mapping using x-ray tomography,” *Exp. Mech.*, vol. 39, no. 3, pp. 217–226, 1999.
- [14] B. K. Bay, “Methods and applications of digital volume correlation,” *J. Strain Anal. Eng. Des.*, vol. 43, no. 8, pp. 745–760, 2008.
- [15] H. Tran, P. Doumalin, C. Delisee, J. C. Dupre, J. Malvestio, and A. Germaneau, “3D mechanical analysis of low-density wood-based fiberboards by X-ray microcomputed tomography and Digital Volume Correlation,” *J. Mater. Sci.*, vol. 48, no. 8, pp. 3198–

- 3212, 2013.
- [16] T. F. Morgeneyer *et al.*, “In situ 3-D observation of early strain localization during failure of thin Al alloy (2198) sheet,” *Acta Mater.*, vol. 69, pp. 78–91, 2014.
- [17] R. Brault, A. Germaneau, J. C. Dupré, P. Doumalin, S. Mistou, and M. Fazzini, “In-situ Analysis of Laminated Composite Materials by X-ray Micro-Computed Tomography and Digital Volume Correlation,” *Exp. Mech.*, vol. 53, no. 7, pp. 1143–1151, 2013.
- [18] M. Mostafavi *et al.*, “Yield behavior beneath hardness indentations in ductile metals, measured by three-dimensional computed X-ray tomography and digital volume correlation,” *Acta Mater.*, vol. 82, pp. 468–482, 2015.
- [19] P. Lecomte-Grosbras, J. Réthoré, N. Limodin, J. F. Witz, and M. Brieu, “Three-Dimensional Investigation of Free-Edge Effects in Laminate Composites Using X-ray Tomography and Digital Volume Correlation,” *Exp. Mech.*, vol. 55, no. 1, pp. 301–311, 2015.
- [20] F. Gillard *et al.*, “The application of digital volume correlation (DVC) to study the microstructural behaviour of trabecular bone during compression,” *J. Mech. Behav. Biomed. Mater.*, vol. 29, pp. 480–499, 2014.
- [21] B. C. Roberts, E. Perilli, and K. J. Reynolds, “Application of the digital volume correlation technique for the measurement of displacement and strain fields in bone: A literature review,” *J. Biomech.*, vol. 47, no. 5, pp. 923–934, 2014.
- [22] F. Mortazavi, E. Ghossein, M. Lévesque, and I. Villemure, “High resolution measurement of internal full-field displacements and strains using global spectral digital volume correlation,” *Opt. Lasers Eng.*, vol. 55, pp. 44–52, 2014.
- [23] J. F. Gonzalez, D. A. Antartis, M. Martinez, S. J. Dillon, I. Chasiotis, and J. Lambros,

- “Three-Dimensional Study of Graphite-Composite Electrode Chemo-Mechanical Response using Digital Volume Correlation,” *Exp. Mech.*, vol. 58, no. 4, pp. 573–583, 2018.
- [24] G. W. Melenka, “Digital volume correlation analysis of braided composites,” in *Digital volume correlation analysis of braided composites*, 2018, p. 15.
- [25] A. Mendoza, J. Schneider, E. Parra, E. Obert, and S. Roux, “Differentiating 3D textile composites: A novel field of application for Digital Volume Correlation,” *Compos. Struct.*, vol. 208, pp. 735–743, 2019.
- [26] H. Haddadi and S. Belhabib, “Use of rigid-body motion for the investigation and estimation of the measurement errors related to digital image correlation technique,” *Opt. Lasers Eng.*, vol. 46, no. 2, pp. 185–196, 2008.
- [27] J. Gonzalez and J. Lambros, “A Parametric Study on the Influence of Internal Speckle Patterning for Digital Volume Correlation in X-Ray Tomography Applications,” *Exp. Tech.*, vol. 40, no. 5, pp. 1447–1459, 2016.
- [28] B. P. Croom, H. Jin, B. Mills, and X. Li, “Effect of Fragile Speckle Patterns on Accuracy of Digital Volume Correlation,” *Exp. Mech.*, vol. 49, no. 7, pp. 991–1005, 2019.
- [29] E. Bar-Kochba, J. Toyjanova, E. Andrews, K. S. Kim, and C. Franck, “A Fast Iterative Digital Volume Correlation Algorithm for Large Deformations,” *Exp. Mech.*, vol. 55, no. 1, pp. 261–274, 2015.
- [30] J. Toyjanova, E. Bar-Kochba, C. López-Fagundo, J. Reichner, D. Hoffman-Kim, and C. Franck, “High resolution, large deformation 3D traction force microscopy,” *PLoS One*, vol. 9, no. 4, 2014.
- [31] Bruker-MicroCT, “Method note An overview of NRecon : reconstructing the best images

- from your microCT scan.” Bruker-MicroCT, Kontich, pp. 1–48, 2013.
- [32] R. Mccaffrey, “normxcorr3.” GitHub, 2016.
- [33] H. M. Zhang *et al.*, “Fast Von Mises strain imaging on ultrasound carotid vessel wall by flow driven diffusion method,” *Australas. Phys. Eng. Sci. Med.*, vol. 41, no. 3, pp. 669–686, 2018.
- [34] A. H. Aitkenhead, “Plot a 3D Array Using Patch.” MathWorks File Exchange, 2010.
- [35] B. Pan, Z. Lu, and H. Xie, “Mean intensity gradient: An effective global parameter for quality assessment of the speckle patterns used in digital image correlation,” *Opt. Lasers Eng.*, vol. 48, no. 4, pp. 469–477, 2010.
- [36] J. Lambros and J. Patel, “Microscale digital image correlation study of irradiation induced ductile-to-brittle transition in polyethylene,” *J. Strain Anal. Eng. Des.*, vol. 46, no. 5, pp. 347–360, 2011.
- [37] B. Pan, Z. Wang, and H. Xie, “Generalized spatial-gradient-based digital image correlation for displacement and shape measurement with subpixel accuracy,” *J. Strain Anal. Eng. Des.*, vol. 44, no. 8, pp. 659–669, 2009.
- [38] M. Gates, J. Lambros, and M. T. Heath, “Towards High Performance Digital Volume Correlation,” *Exp. Mech.*, 2011.
- [39] P. L. Reu, W. Sweatt, T. Miller, and D. Fleming, “Camera System Resolution and its Influence on Digital Image Correlation,” *Exp. Mech.*, vol. 55, no. 1, 2015.
- [40] D. Lecompte, S. Bossuyt, S. Cooreman, H. Sol, and J. Vantomme, “Study and generation of optimal speckle patterns for DIC,” in *Proceedings of the SEM Annual Conference and Exposition on Experimental and Applied Mechanics 2007*, 2007.
- [41] M. Gates, J. Gonzalez, J. Lambros, and M. T. Heath, “Subset Refinement for Digital



Volume Correlation: Numerical and Experimental Applications,” *Exp. Mech.*, vol. 55, pp. 245–259, 2015.

- [42] F. Laurin, C. Julien, and P. Paulmier, “Damage and strength analysis of open-hole laminated plates under tensile, compressive and bending loadings,” in *ECCM 2016 - Proceeding of the 17th European Conference on Composite Materials*, 2016.
- [43] D. Yoon, S. Kim, J. Kim, and Y. Doh, “Development and evaluation of crack band model implemented progressive failure analysis method for notched composite laminate,” *Appl. Sci.*, 2019.

## **Chapter 4: Digital Volume Correlation Analysis of PLA based fused filament fabrication copper infused composites\***

\*a version of this chapter has been submitted to Material Characterization Journal as:  
Timpano, C.S, Melenka, G.W, Digital volume correlation analysis of PLA based fused filament fabrication printed composites

### **4.1 Introduction**

The emergence of additive manufacturing (AM) has provided a powerful tool for the rapid design and fabrication of parts for engineering applications. Fused filament fabrication (FFF) has become a popular option in the industrial sector due to the wide selection of compatible thermoplastic polymers with the process [1]. Additionally, the process is well suited for implementation into current manufacturing operations for mass production. Traditional FFF parts are held back due to their lower mechanical properties and inconsistent quality. The poor material strength of traditional FFF parts results in them typically being only suitable for prototyping [2]. Thus, to improve the material strength and improve AM produced pieces, researchers have begun to produce AM components composed of multiple materials. To this end, researchers have studied the effects of the addition of various reinforcing materials such as carbon nanotubes, graphene, or metal particles to the base polymer [1], [3]. These 3D printed composite materials help address the lack of strength of traditional AM and FFF produced parts but further complicate the already complex material analysis.

Before discussing the challenges involved in composite FFF parts, it is crucial first to discuss the issues with analyzing single-phase FFF parts. FFF parts exhibit anisotropic mechanical properties due to their complex microstructure. Regions of high localized porosity and imperfect layer bonding contribute to FFF parts' complex microstructure and anisotropic material properties [4], [5]. This complexity is further complicated by adding a reinforcing phase where factors such as particle loading, size, and adhesion affect the mechanical properties of the part [6]. Traditional

testing methods of material properties, such as strain gauges or extensometers, are unreliable for materials produced through FFF. Thus, researchers have proposed an alternative approach for analyzing samples with anisotropic material properties and heterogenous deformation fields known as Digital Image Correlation (DIC) [7]. DIC captures a coupon's images during material testing from either a 2D or 3D stereo camera set up to visualize the material's deformation [8]. These images are then utilized as input for a software algorithm to calculate the material's deformation and strain [8]. DIC provides an advantage over traditional testing methods as a full-field profile of deformation and strain can be determined.

Though DIC offers many advantages, its adoption for material analysis for FFF produced parts has been limited. Zaldivir *et al.* were one of the first groups to use DIC to study the effects of build orientation on FFF fabricated ULTEM 9085 tensile coupons [5]. The study showed that deformation developed in a highly anisotropic manner. Additionally, the build orientation had a significant effect on the material strength and formation of strain irregularities within the sample. Goodarzi Hosseinabadi *et al.* provided a comparison study aided by DIC on Acrylonitrile butadiene styrene (ABS) FFF honeycomb parts and photocured polyjet honeycomb parts [9]. The usage of DIC allowed for the resolution of strain fields for samples under a compressive load. An extension of this study was completed to understand the shearing effects of a compressive load on the piece. This study showed that shear occurred in three stages, which agreed with finite element analysis (FEA) models [10].

While DIC allows for full field testing of FFF parts, the cameras used for capturing images limit it to only surface level results [11]. The advent of micro-computed tomography ( $\mu$ -CT) has provided a non-destructive method to capture interior features of materials on the sub-millimeter level.  $\mu$ -CT operates by passing x-rays through a rotating sample to obtain a volumetric set of

images [11]. As the x-rays pass through the material, they are attenuated based on the density of the material they pass through and collected by an x-ray receptor [11]. This data is used to form shadow-projections of the images, which are reconstructed into 2D cross-sections of the volume [12].

$\mu$ -CT has recently emerged as a valuable tool for the analysis of AM produced parts. Researchers have begun to utilize  $\mu$ -CT to image the microstructure, quality, and printing parameters of various AM parts. The effects of printing parameters such as temperature, raster orientation, and extrusion width on the materials' microstructures are of particular interest [13]–[16]. Through the aid of the  $\mu$ -CT images, accurate measurements can be made on critical structural parameters such as porosity and raster size. This paper proposes to utilize  $\mu$ -CT to measure changes in the microstructure of FFF composites to external loading.

With the 3D data set provided through  $\mu$ -CT, the ability to capture volumetric full-field strain data is made possible via digital volume correlation (DVC). As a 3D alternative to DIC, DVC was first outlined in the ground-breaking paper by Bay *et al.* [17]. DVC operates by discretizing a reference and displaced data set into a series of subsets. For an accurate correlation, these subsets must contain features with a random variation of greyscale values. Greyscale variation can be formed naturally from the natural microstructure or as a result of elements externally seeded into the material. Features in each subset are tracked using an objective function to determine the displacement from the reference position to the deformed position. This data can then be directly converted into strain, thus providing a volumetric model of the internal deformation.

DVC is an emerging method for displacement and strain measurement; therefore, current literature in these areas is limited. DVC was first used in bioscience, particularly for obtaining existing strain fields in trabecular bone samples [18]–[20]. Current DVC research has begun to

extend out of the field of bioscience and into engineering material science. DVC has proved a powerful tool for analyzing heterogeneous materials such as wood, metal alloys, and composites laminates [21]–[28]. However, with the rapid advancements in additive manufacturing, the technique has been sparsely utilized to aid in the investigation of their mechanical properties [4].

This study aims to address the current gaps present in the literature on the analysis and application of  $\mu$ -CT and DVC for FFF produced composite materials. Mainly, this work demonstrates the viability and advantages of utilizing  $\mu$ -CT and DVC to obtain structural and mechanical data. For this purpose, an FFF part was constructed according to a modified ASTM-D648 14 Type V that is compatible with the utilized  $\mu$ -CT integrated material test stage (MTS). The samples were then imaged at each stage of a 3-part stepwise load to capture deformation progression on the sample's microstructure. The  $\mu$ -CT images were analyzed to demonstrate the bulk response of the material's microstructure and porosity and air gap orientation. This information was then utilized to lead the discussion on DVC results for internal displacement and strain fields.

The resulting  $\mu$ -CT tomographs were utilized as an input for DVC to capture the internal displacement and strain fields. To this end, an open-source DVC software known as Fast Iterative Digital Volume Correlation (FIDVC) was employed to calculate the 3D strain and displacement [29]. FIDVC operates based on an iterative algorithm, where the correlation window size becomes smaller through each pass to improve resolution on the sample's displacement. In this study, a 100 N load was first applied to the test sample as a reference point with subsequent loads applied at 150 N and 200 N load states. Due to the coupon's deformation experience and reduced computational burden, it was necessary to reduce the dataset to a quarter of their original resolution. Measurements of the longitudinal displacements and longitudinal and transverse strains

were then calculated via DVC at the 150 N and 200 N load conditions by utilizing the 100 N load as a reference point. Renderings of the displacement and strain behaviour were then made, allowing for the 3D visualization and analysis of the sample's mechanical response to the uniaxial load condition. The volumetric displacement and strain results can be built upon in later works allowing for input or direct comparison to improve current FEA models [30]–[33].

## **4.2 Methodology**

### **4.2.1 Manufacturing**

Samples were 3D printing using a 1.75 mm diameter PLA filament with embedded copper particles (Metal Filled PLA, CCTree-Mech solutions LTD, Concord, Ontario). Samples were designed and printed into tensile coupons based on ASTM D638-14 Type V [34]. Due to the MTS's restrictive size (440 N integrated test stage, Bruker, Belgium), modifications were required to the geometry. The coupon's total length was reduced to 30 mm and thickness to 3 mm while maintaining the gauge length and width to ensure the coupon fit within the MTS's. Additionally, the end tabs were increased to a width of 18 mm, and a pair of 3 mm holes were included to improve compatibility with the MTS. The difference between the ASTM D638-14 type V tensile coupon and the modified used in the current study are seen in Figure 4-1 a) and b), respectively.

Modelling the tensile coupons was done using a computer-aided design (CAD) modelling package (Solidworks, S2018, Dassault Systemes, Vélizy-Villacoublay, France). The sample CAD model was sliced using open-source software (Cura, 15.04.06, Ultimaker, Geldermalsen, Netherlands). The sliced sample was finally printed using a desktop 3D printer (Select mini V2, Monoprice, Rancho Cucamonga, California, United States) fitted with a 0.4 mm nozzle diameter. Table 4-1 shows a list of the printing parameters utilized to manufacture the tensile coupons. Samples were printed with a 100% infill at a layer thickness of 0.10 mm. The nozzle's temperature

was set to 210 °C, and the build plate temperature was 70 °C. Samples were printed first by creating a 0.8 mm shell on each layer that outlined the coupon’s geometry before completing the infill with rasters on a +45°/-45°. In Figure 4-2, a) the nozzle start position and path for a single layer is presented. Figure 4-2 b) shows the center layer’s corresponding view as produced by the utilized slicer software. To improve layer adhesion to the printer bed was increased by using the “raft” setting in Cura. A render of the tensile coupon housed inside the MTS is shown in Figure 4-3. The tensile coupon is connected to the sample’s end tabs via two 3 mm screws at each end. Surrounding the tensile coupon is a radiolucent pain, which provides some rigidity to the test frame during loading. During loading, the top end of the coupon remains static as the bottom face is displaced downward by 420 N rated load cells.

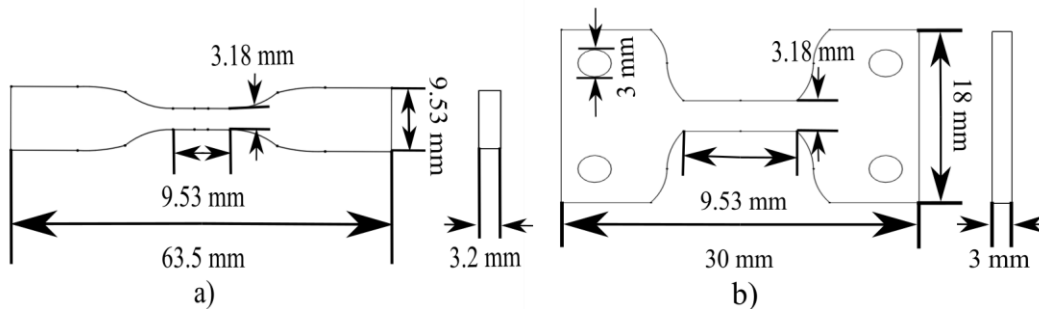


Figure 4-1: Cross-section sketch of the tensile couple: a) ASTM D638-14 type V b) modified design to fit in MTS

Table 4-1: Manufacturing parameters for slicer software utilized to produced tensile coupon

Manufacturing Parameter	Parameter Value
Layer Thickness	0.1 mm
Infill Density	100 %
Fill Direction	+45°/-45°
Shell Thickness	0.8 mm
Nozzle Temperature	210 °C
Bed Temperature	70 °C

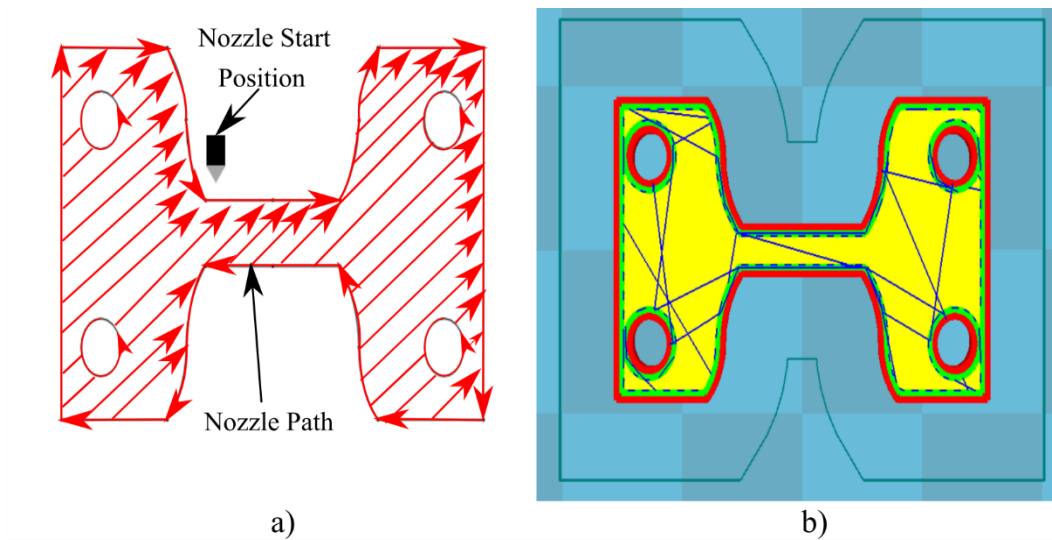


Figure 4-2: Representation of the tensile coupons printing scheme: a) nozzle path, b) slicer view of the center layer of coupon

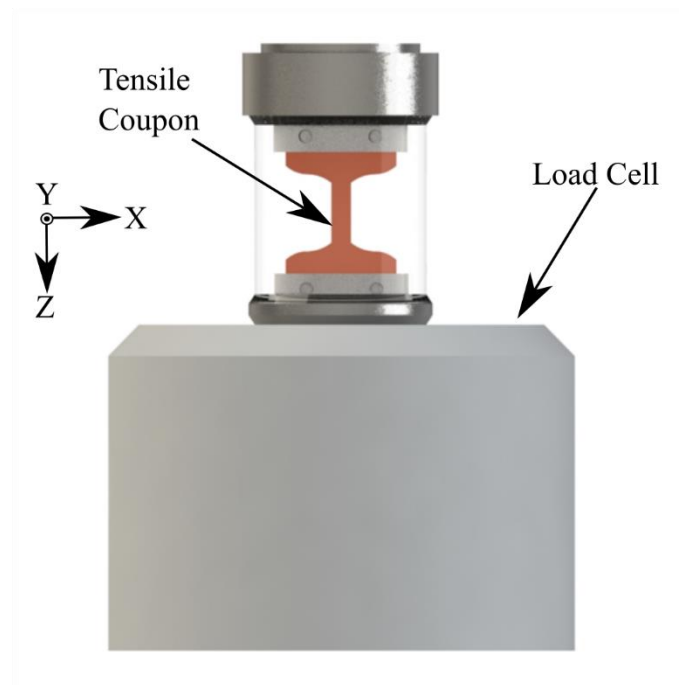


Figure 4-3: Model render of the MTS loaded with tensile coupon

#### 4.2.2 Micro-Computed Tomography

The copper PLA tensile coupons were imaged using a desktop  $\mu$ -CT (Skyscan, 1272  $\mu$ -CT, scanner, Bruker, Belgium.). Table 4-2 presents a complete list of the  $\mu$ -CT inputs employed to image the sample. The PLA samples were imaged using a pixel size of 1.6  $\mu\text{m}/\text{px}$  with a



4904x3280 pixel resolution. Settings were selected to ensure the embedded copper particles were captured in the image while allowing for a majority of the gauge length to be captured. The source voltage and current used in this study were 65 kV and 125  $\mu$ A. Due to metals' tendency to cause metal scattering artifacts and beam hardening, a 0.5 mm aluminum filter was used to reduce possible metal artifacts that may appear in tomographs post-reconstruction. Three scans were completed successively at loads of 100 N, 150N, and 200 with a 0.2° rotation step. The final dataset size before reconstruction for each load contained 938 shadow projections. A single shadow projection from each dataset is shown in Figure 4-4. Measurements of the sample thickness show a decrease in the width of approximately 0.01 mm per load step. This decrease in sample width as the tensile load increases is indicative of a reduction of cross-section size. Of note, the measurements shown are larger than the 3.18 mm width of the solid model used to manufacture the sample. The larger width seen in the sample shadow projections indicates manufacturing inconsistencies on the part of the 3D printer. The increase in the model's width is shown to be between 0.02 mm to 0.04 mm, which is well within the typical tolerancing of the FFF printed part [35].

Table 4-2: List of scan parameters utilized to image the tensile coupon

$\mu$ -CT Parameter	Setting
Source Voltage	65 kV
Source Current	125 $\mu$ A
Resolution (WxH)	4904 x 3280 px
Pixel Size	1.6 $\mu$ m/px
Filter	0.5 mm Aluminum
Rotation Step	0.2°

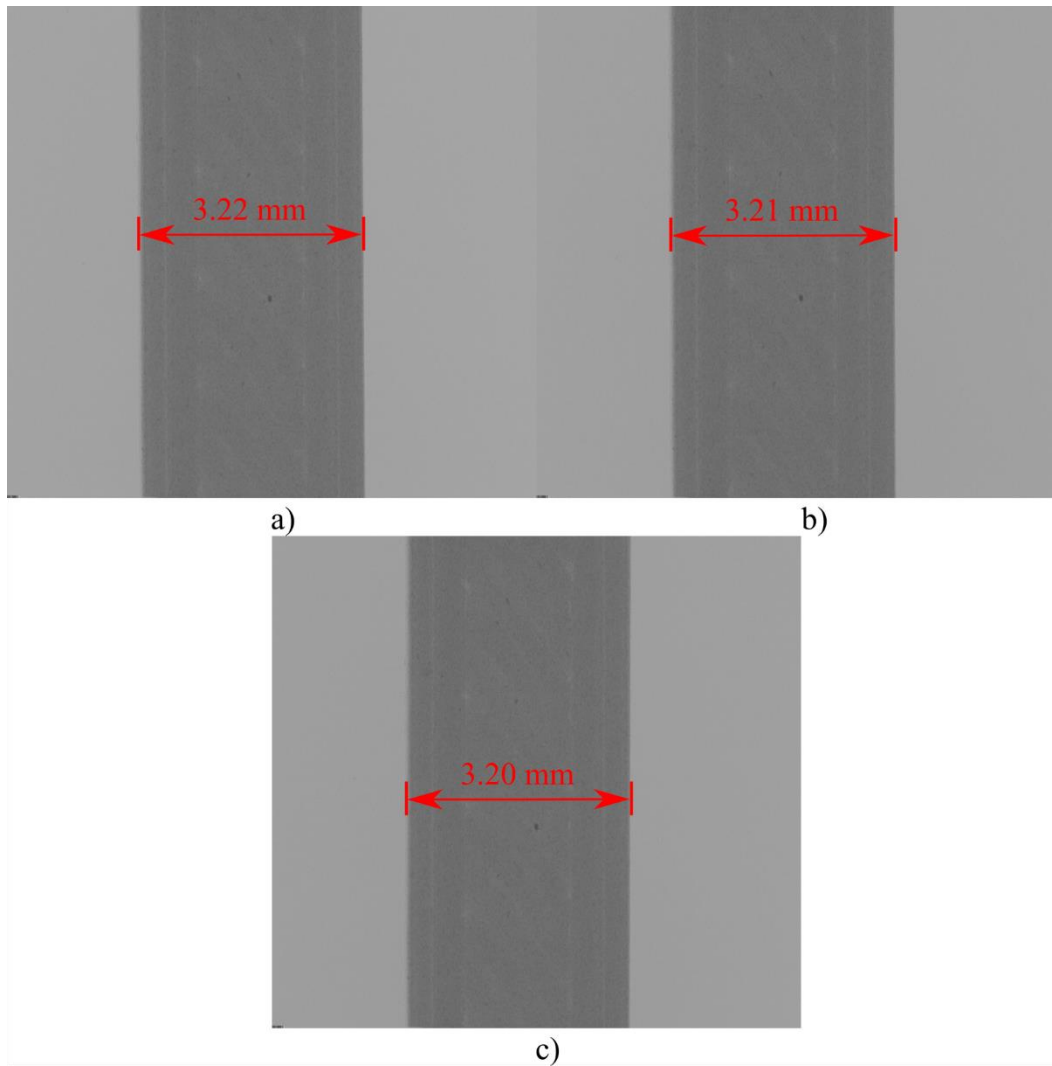


Figure 4-4: Shadow projections of the copper PLA sample for a) 100 N, b) 150 N, and c) 200 N loads

### 4.2.3 Reconstruction

A  $\mu$ -CT reconstruction package (NRecon version 1.7.1.0, Bruker, Belgium) was utilized to convert the shadow projection into a series of perpendicular cross-sectional images. Before reconstruction, a range of greyscale values must be selected to provide image contrast and allow for the visualization of microstructure features. It is recommended by the software package provider to set the lower limit of the attenuation range to 0 (-1000 HU) and the upper value to be around 10-20% greater than the maximum variation in greyscale [36]. Using the criteria previously

presented, the attenuation range selection was 0 (-1000 HU) to 0.5 (31768 HU) for the 100 N and 200 N and 0 (-1000 HU) to 0.25 (15384 HU) for the 150 N load. It is important to note that the attenuation ranger utilized for the 150 N load differs from the 100 N and 200 N load. The reason being is that samples were scan using a 180° scan rotation. Thus, starting position for the scans differed between the 150 N sample and the 100 and 200 N loads. Therefore, it was necessary to set the attenuation range differently to meet the previously mentioned criteria.

While procedures were put in place to reduce noise and artifacts before scanning, this does not eliminate the possibility that artifacts appear. Thus, a 49% beam hardening filter and a 10% ring artifact filter was applied to the image set during reconstruction. The beam hardening filter's aggressive use compensated for the streaking caused by metal particles' presence within the sample [37]. Figure 4-5 shows an example of a reconstructed cross-section from the 100 N dataset. The contrast in Figure 4-5 was enhanced beyond what was used in the current study to provide better microstructure visibility. Within the tomographs, the copper particles can be easily distinguished from the PLA due to higher greyscale values resulting from their higher density.

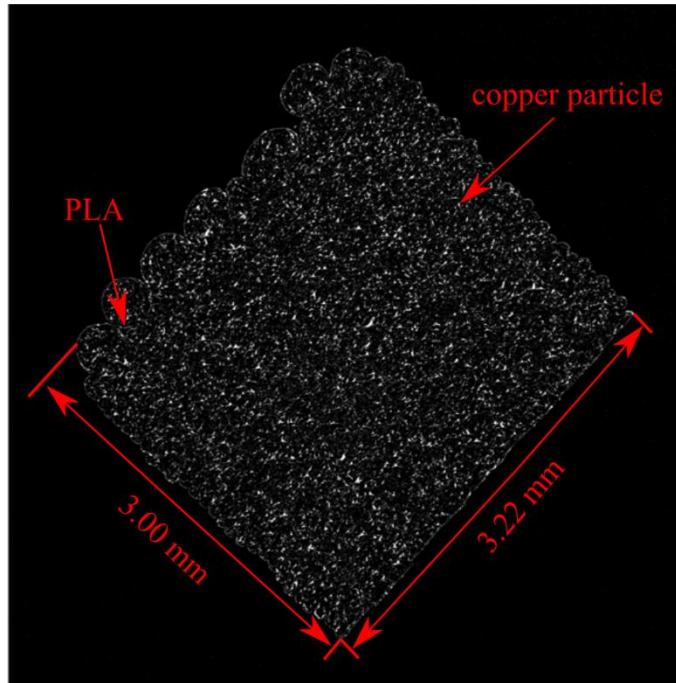


Figure 4-5: Reconstructed cross-section of copper PLA sample with enhanced contrast.

#### **4.2.4 Image Segmentation**

##### **4.2.4.1 Image Quality Assessment**

Before performing DVC measurements, the quality of the tomographic images must be assessed for DVC compatibility. For DVC measurements, the greyscale distribution and particle quantification can be used to evaluate image data quality. These parameters were measured within a single correlation window, which was cropped out of the full resolution 100 N dataset equal to 128 x 128 x 128 voxels or 0.2048 x 0.2048 x 0.2048 mm. The greyscale histogram of the 3D image stack was then measured using MATLAB (MATLAB R2018a, The MathWorks, Natick, Mass) digital image processing toolbox. The particle numbers' quantification was done through a commercial CT image segmentation software (CTan version 1.16.8.0, Bruker  $\mu$ CT, Belgium). As a requirement to quantify features within the images, it is first required that the dataset be binarized. Binarization was done by thresholding the dataset between greyscale values of 11-256, which

highlights the internal particles. Particles were then measured using the “3D analysis” command, which counts all-white features within the image sequence and measures their area and volume.

#### **4.2.4.2 Cross-Section Analysis**

Measurements of sample manufacturing variability and the microstructure response to the tensile load were first measured through an image segmentation procedure before a more detailed analysis of the latter was conducted utilizing DVC. Of particular interest for this paper was quantifying the change of cross-sectional area and air gaps between rasters with the tensile loading. This measurement was performed via CT image segmentation software. Typically, segmentation in CTAn is broken into three steps: 1) binarization, 2) filtering, and 3) morphological operation. For quantifying the sample’s cross-sectional area, the images were segmented to show one single-phase cross-section. Due to the large sizes of the reconstructed data, a 3 mm section of each sample was examined to decrease the computational burden.

As a result of the different attenuation ranges used to reconstruct the data, the 100 and 200 N dataset and 150 N dataset were processed slightly differently. The steps utilized for these two procedures are listed in Table 4-3 and Table 4-4, respectively. The 100 N and 200 N datasets were binarized by thresholding the sample between greyscale values of 10-255. This binarization was shown to provide the best compromise of realizing the sample’s internal features and reduce noise. Filtration of the resultant noise from binarization was done by performing a despeckling operation in 2D space, eliminating all white details below a size of 8 pixels. To fill the material’s internal structure, a morphological closing operation that consists of a dilation followed by erosion was used with a 10 pixel round kernel. While the morphological closing did homogenize most of the internal cross-section, it also increased the size of some of the noise not eliminated by the despeckling operation. Thus, an erosion operation of 5 pixels was utilized to eliminate this noise,

followed by a 5-pixel dilation to address a subsequent reduction in size resulting from the erosion. As a final step to close a few outstanding gaps in the cross-section, a 60-pixel square kernel morphological close was completed. The effects of this procedure on the  $\mu$ -CT images are shown in Figure 4-6. Figure 4-6 a) highlight the  $\mu$ -CT tomograph before image segmentation. Note that this has been intentionally left dark to highlight the true greyscale variation. While in Figure 4-6 b) the realized cross-sectional from the  $\mu$ -CT image segmentation procedure is shown.

Table 4-3: Image processing parameters used to define the cross-sectional area of 100 N and 200 N datasets

Image Processing Operation	Image Processing Parameter
Binarization (Greyscale threshold)	10-255
2D Despeckling (white pixels)	<8 pixels
2D Morphological Closing (Round)	10 pixels
2D Erosion (square)	5 pixels
2D Dilatation (square)	5 pixels
2D Morphological Closing (Square)	60 pixels

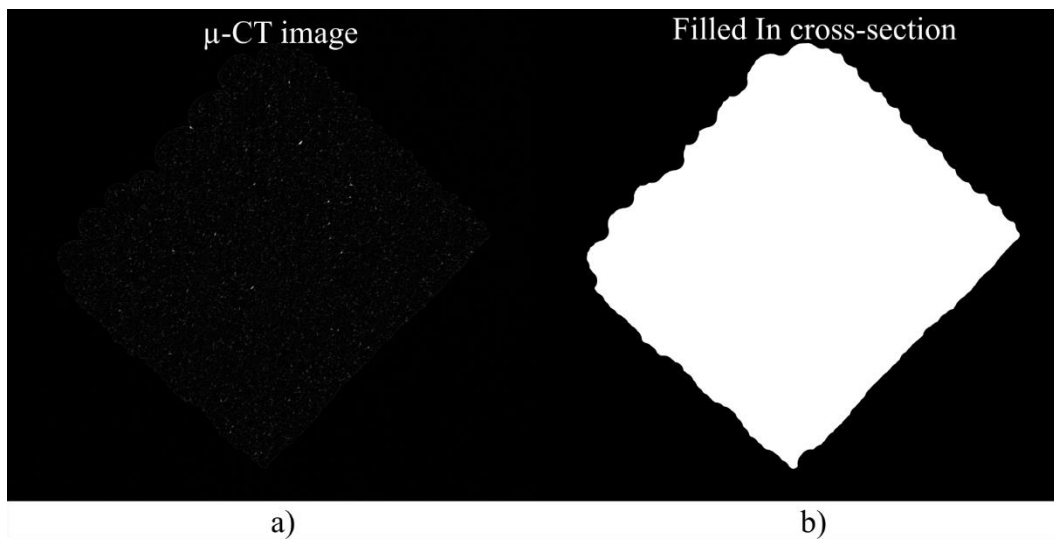


Figure 4-6: Segmentation of copper PLA sample cross-section: a)  $\mu$ -CT image, and b) filled sample cross-section

The procedure used to process the 150 N dataset followed the same general steps presented in Table 4-3. However, due to the difference in the attenuation range used for reconstructing the 150 N dataset, the input parameters differed slightly from the 100 N and 200 N datasets. In practice, the differing attenuation range only affects the binarization and despeckling steps. Due to the narrower attenuation range, the greyscale thresholding utilized to binarize the image was set between 23-255. As a consequence of this, the noise surrounding the sample was much more extensive. Thus, a more aggressively sized despeckling operation was performed by removing white features below a size of 15 pixels. Beyond this step, the remaining procedures and reasoning for utilization are the same for the 100 N and 200 N dataset. The entire utilized process is outlined in Table 4-4.

Table 4-4: Image processing parameters used to define the cross-sectional area of 150 N datasets

Image Processing Operation	Image Processing Parameter
Binarization (Greyscale threshold)	23-255
2D Despeckling (white pixels)	<15 pixels
2D Morphological Closing (Round)	10 pixels
2D Erosion (square)	5 pixels
2D Dilatation (square)	5 pixels
2D Morphological Closing (Square)	60 pixels

After segmenting the images, the cross-sectional area of each image within the stack was quantified. This quantification was done by utilizing the image processing toolbox in MATLAB. A series of statistical measurements can be made within MATLAB on the binarized image using the ‘regionprops’ command. For this study, the area parameter was used, which measures the size of all connected white pixels within a single image. By inputting each segmented image individually through the software, the area and its variation along the 3 mm section were computed.

#### **4.2.4.3 Air Gap Measurements**

A similar image segmentation procedure was utilized to quantify the air gaps present in the sample. Quantification of the air gaps allows for assessing the actual sample parameters post-manufacturing and how they change during the material's mechanical testing. Additionally, this will enable the examination and relation of the strain fields obtained from the DVC analysis to printing patterns. To perform this measurement, it was useful to reslice the reconstructed data in the layer thickness direction to improve visualization. Each dataset's reslicing was achieved by utilizing an open-source java-based image processing program (Fiji, National Institutes of Health, Bethesda, MD). As seen in Figure 4-5, the reconstructed data is slightly rotated; thus, before reslicing the data, images were first rotated  $45^\circ$  using a bilinear approximation interpolation scheme to realign the sample. An image stack could then obtain in the thickness direction by utilizing the reslice command. Figure 4-7 provides a comparison of the reconstructed images and the reconstructed dataset. The original reconstructed images are shown to lay in the XY plane of the sample and vary along the Z direction. By reslicing the dataset into the XZ plane, the cross-section area's variation along Y or the nozzle's height-wise direction, visualization of the airgaps becomes possible.



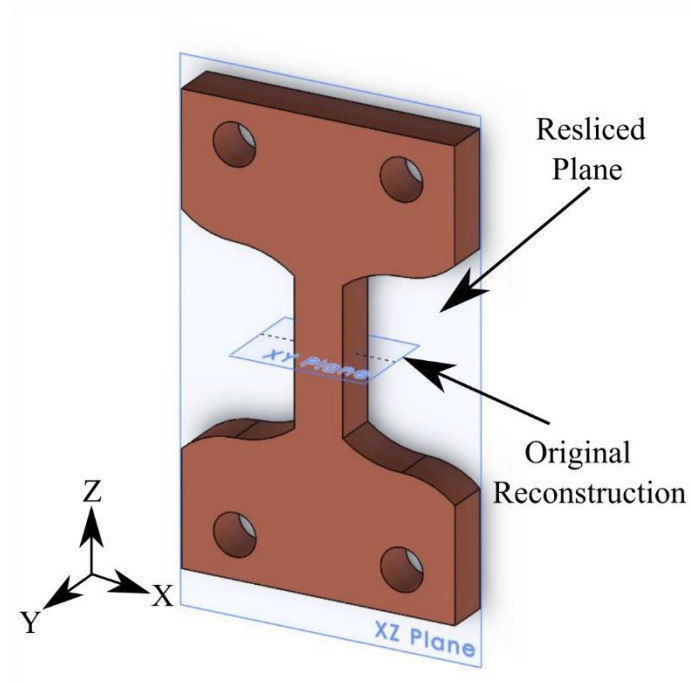


Figure 4-7: Schematic showing original reconstruction plane from micro-CT, and resliced plane

After reslicing the data, a segmentation procedure was again utilized to visualize and measure the sample air gaps. Unlike the cross-sectional analysis, each dataset was processed using the same parameters as it was found the best range for binarization was to contain the entire greyscale range. A similar image segmentation procedure was followed to that used in a previous  $\mu$ -CT study to quantify open pores in PVDF foams [38]. For this analysis, the datasets were reduced to half their original resolution to decrease computation time.

The image processing parameters for each dataset are shown in Table 4-5. As a first step toward filling in the sample, small black features that did not constitute air gaps were removed. This was done in two stages first by removing all-black features surrounded by white with a volume of 50 voxels and second by eliminating all features with an area of 200 pixels or less. After removing the majority of small black features within the sample, three items still existed within the image data: the significant air gaps, white noise, and unfilled gaps in the PLA that don't

constitute air gaps. A 2D white despeckling operation was undergone to remove all white pixels below 200 pixels to remove the image’s white noise. Removal of the unfilled openings in PLA, a 3D despeckling was done to remove voxels below a size of 2000 voxels. This procedure was then followed by a small morphological close in 3D space to reduce the size of any remaining gaps before passing over the data one final time with the same 2000 voxel despeckling operation. After these steps, the PLA was successfully realized as white pixels within the image. Thus, to analyze the air gaps, the images were inverted by subtracting the original image from a region of interest (ROI) surrounding the sample. Finally, measurements were conducted on these images using the built-in 3D analysis tool to quantify the volume of the air gaps. The resulting images for each significant step in the image segmentation process are shown in Figure 4-8. Figure 4-8 a) was notably left dark to reflect the true contrast of the image before binarization and segmentation.

Table 4-5: Image processing parameters to segment out sample air gaps for 100 N, 150 N and 200 N dataset

Image Processing Operation	Image Processing Parameter
Binarization (Greyscale Threshold)	1-255
Despeckling (3D black voxels)	<50 voxels
Despeckling (2D black pixels)	<300 pixels
Despeckling (2D white pixels)	<200 pixels
Despeckling (3D black voxels)	<2000 voxels
Morphological Close (3D Round)	1 Voxel
Despeckling (3D black voxels)	<2000 voxels
Arithmetic Operation	Sub ROI

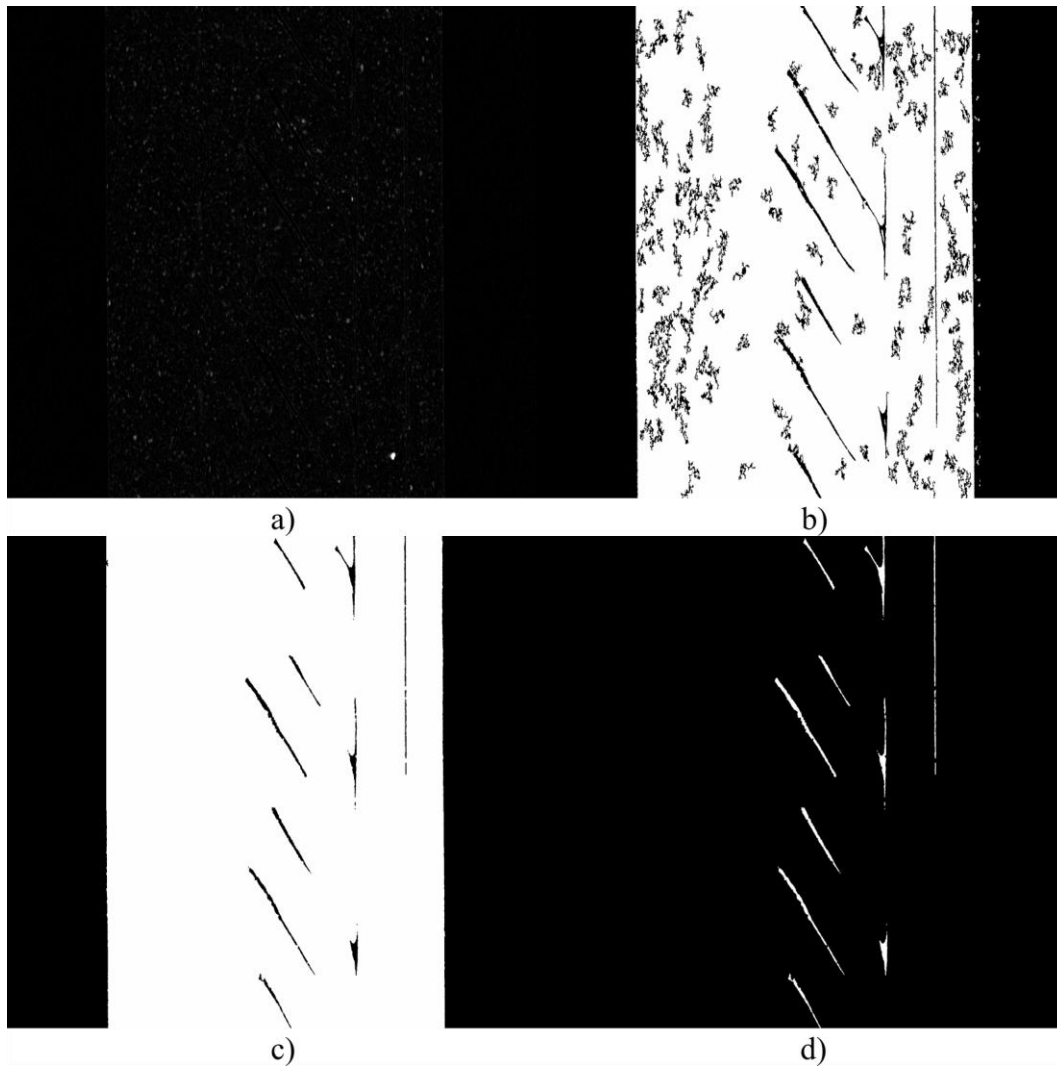


Figure 4-8: Pores identification steps for copper PLA sample: a)  $\mu$ -CT image, b) filtered and despeckled, c) large despeckled and closed, d) inversed image highlighting air gaps

## 4.2.5 Digital Volume Correlation

### 4.2.5.1 Fundamental principles of FIDVC

Calculations of internal displacements and strains were determined using an open-source MATLAB based DVC software (FIDVC, version 1.2.4) [29]. The DVC software utilized operates by first discretizing a volume into a series of subsets based on a user-selected subset size and subset spacing. The DVC software used an iterative approach where the subset's size is reduced between passes to a volume as small as  $32 \times 32 \times 32$  voxel to increase correlation accuracy. After correlation displacement is provided by four separate 3D arrays. These four arrays consisted of displacements

in the x-direction, y-direction, z-direction, and displacement magnitude. Figure 4-9 shows a representation of the dataset after discretization. Each subset in the array contains a single value representing the estimated displacement in that region. Not shown in Figure 4-9 is the overlap of each subset. After discretization each subset is overlapped by a specified percentage from the user with all other surrounding subsets in order to improve spatial resolution.

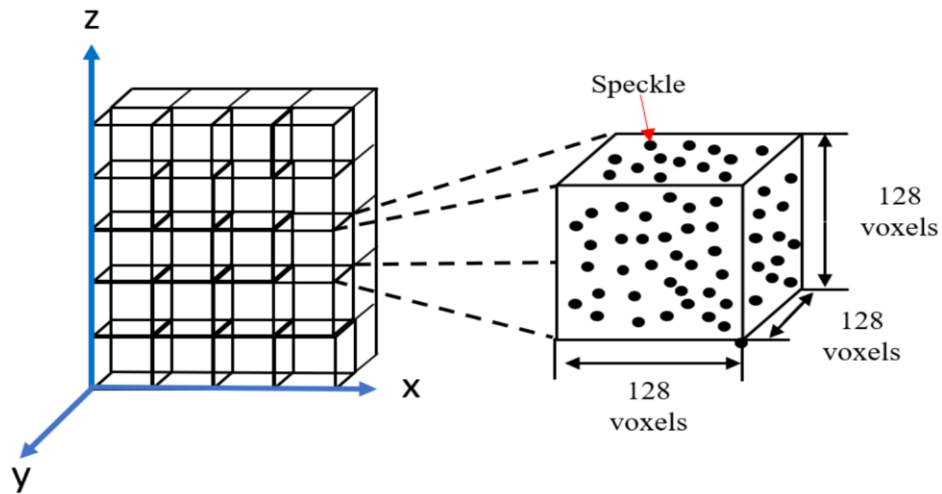


Figure 4-9: Illustration of DVC discretization process of sample into individual speckled subset.

Strain measurements were computed using an open-source extension to the DVC software (LD-3D-TFM, version 1.1). This extension calculates strain values directly from the displacement data according to the Lagrangian strain formulation. Equation 1 shows the general form for Lagrangian linear elastic strain tensor where  $E$  represents the strain tensor,  $i$  represents the first coordinate direction,  $j$  the second coordinate direction,  $u$  the displacement, and  $x$  the direction of the displacement [39]. Equation 2 shows the final strain tensor matrix with six unique entries: the three normal strain ( $\epsilon$ ) and three shear strain ( $\tau$ ). Each strain tensor component is made up of a 3D matrix of equal size to the displacement matrix. Custom code was used to convert the matrices into the Visualization Toolkit (VTK) to visualize the data in 3D. Visualization and analysis were then

carried out using an open-source scientific visualization platform (Paraview, 5.8.0, Sandia National Laboratories, Kitware Inc, Los Alamos National Laboratory).

$$E_{ij} = \frac{1}{2} \left( \frac{\partial u_i}{\partial x_j} + \frac{\partial u_j}{\partial x_i} \right) \quad i = 1,2,3 \quad j = 1,2,3 \quad (4.1)$$

$$\varepsilon = \begin{bmatrix} \varepsilon_{xx} & \tau_{xy} & \tau_{xz} \\ \tau_{yx} & \varepsilon_{yy} & \tau_{yz} \\ \tau_{zx} & \tau_{zy} & \varepsilon_{zz} \end{bmatrix} \quad (4.2)$$

#### 4.2.5.2 Digital Volume Correlation Input Parameters

This study's DVC measurement was conducted on a server computer (Precision T5600, Dell, Round Rock, Texas) equipped with 112 Gb of Ram and two Intel® Xeon® CPU E5-2680, 2701 Mhz 8 core processors. Before the DVC was run first, the dataset was downsampled to a quarter of its original size. The downsampling algorithm works by averaging voxel greyscale level in a cube with dimensions equal to the user selected resizing, for this study a 4x4x4 downsampling voxel was utilized. While downsampling the dataset reduces image resolution and may introduce a source of error, this process provided many benefits that aided in the analysis of displacement and strain. The first benefit associated with downsampling is the associated reduction computational burden required to perform DVC on the full volume of interest (VOI). Additionally, this can increase the size of data contained within a correlation window. With the restrictive number of subset sizes provided, for the full resolution, the data was restrained to between a 128 x 128 x 128 voxel (0.2048 x 0.2048 x 0.2048 mm) subset size and 32 x 32 x 32 voxel (0.052 x 0.052 x 0.052 mm) subset size. Considering the rigidity of copper filled PLA sample, which has previously been presented by Liu *et al.*, the displacements seen are likely to exceed some of the sizes of these subsets [40]. Thus, by reducing the data, it was found that enough detail is provided within each

subset so that the DVC software will be effectively able to capture the sample displacement and strain caused by the applied forces of 100 N, 150 N, and 200 N.

Table 4-6 shows a list of input parameters utilized for the DVC studies. The preload state of 100 N was used as the reference dataset from which displacements and strains were calculated. A list of the program input parameters can be seen in Table 4-6. The analysis was started with a course subset size of 128 x 128 x 128 pixels, and over four iterations, the correlation subsets were reduced to 32 x 32 x 32 pixels. A subset overlap was of 50% was utilized, which has previously been shown to provide the most accurate results for DVC measurements [41]. Finally, the mesh spacing was set to a size of 16, which is equivalent to half the size of the final subset as recommended by the software providers [29].

Table 4-6: Digital volume correlation input parameters for displacement and strain measurements of copper-PLA sample

Correlation Parameter	Value
Subset Size	128 x 128 x 128
Mesh Spacing	16
Max Iteration	5
Overlap	50%
Convergence Criteria	0.25,0.5,0.0625
Cross-Correlation Threshold	0.0001

### **4.3 Results and Discussion**

#### **4.3.1 Image Segmentation**

##### **4.3.1.1 Greyscale Distribution and Particles**

The quality of the obtained images was first assessed for the sample’s greyscale distribution. The ideal greyscale patterns utilized for DIC measurements exhibit a unimodal profile centering around mean greyscale values [42]–[44]. Figure 4-10 shows a sample slice taken from the dataset and the entire subsets representative greyscale pattern. The greyscale histogram shows data with a

peek at the low grayscale values representing black pixels within the image. Pan *et al.* has previously demonstrated the accuracy of a similar greyscale pattern for digital correlation measurement [45]. Thus, while this does not display the typical greyscale distribution, it should still provide enough variation for correlation measurement to be obtained.

Before discussing the sample particle quantification, it is first necessary to discuss potential sources in error for the measurement. Observing Figure 4-10 a), one can quickly identify beam hardening and streaking within the image due to the metal particles. These features within the tomographs make a precise measurement of the copper particle's volume challenging to resolve. Fortunately, particle quantity is a more meaningful indication of image performance for DVC measurement. Thus, the discussion here will be focused on the amount of the particles rather than their size. However, in regards to the DVC, it has been shown that beam hardening has little effect on the accuracy of displacement measurement [46]. For these measurements' particles smaller than  $4.097 \mu\text{m}^3$ , the volume of a resolved voxel was considered noise. Segmentation showed 1022 features with a volume above  $4.097 \mu\text{m}^3$ . This quantity is well above the minimum number required for an accurate correlation of 27 presented by Croom *et al.* and should provide an exact correlation [47].

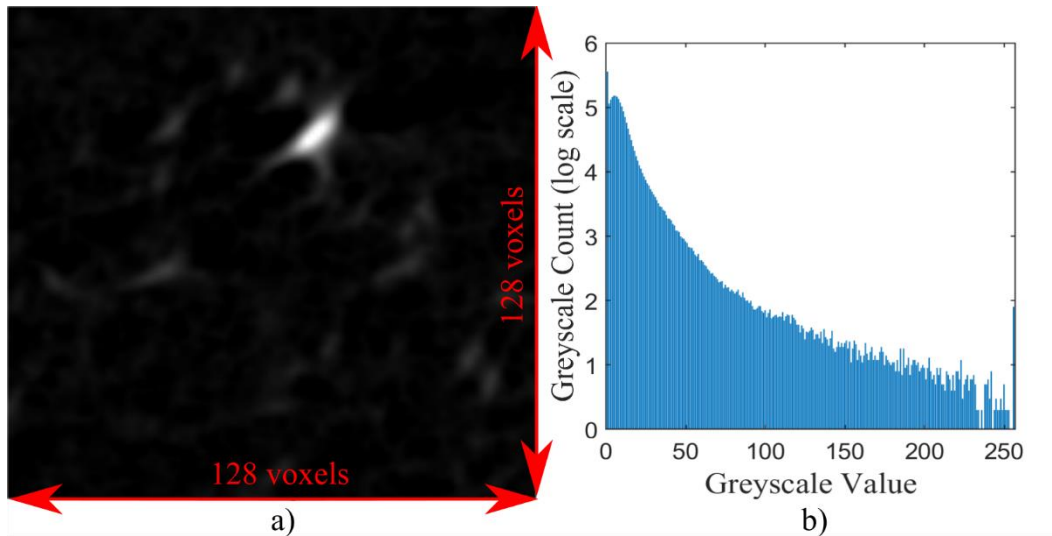


Figure 4-10:  $\mu$ -CT data for 128 voxel correlation window size: a) single  $\mu$ -CT slice from correlation window, b) resultant greyscale histogram for correlation window

#### 4.3.1.2 Cross-Sectional Analysis

Results from the CT segmentation analysis of the cross-sectional area through a 3 mm section of each dataset are shown in Figure 4-11. Two clear trends can be seen regarding the cross-sectional area along the gauge length of the sample. The first trend seen is that each slice's cross-section is shown to vary along the gauge length of material. Variation of the cross-sectional area is likely a result of manufacturing inconsistencies, which has led to specific layers forming larger than other layers. The standard deviation of the area along each slice is reported in Table 4-7 to quantify the cross-section area variation across the gauge length. It is shown here that variation in each segment lies in the range of  $\pm 0.0493 \text{ mm}^2$  to  $\pm 0.0536 \text{ mm}^2$ . These tolerance ranges are well within the printer's linear tolerance range of 0.1 mm to 0.3 mm. This cross-sectional area variation is reflected through the mean cross-sectional area of each sample:  $9.7013 \text{ mm}^2$ ,  $9.6081 \text{ mm}^2$ , and  $9.5763 \text{ mm}^2$  at the 100 N, 150 N, and 200 N loads, respectively. These areas are all slightly larger than the theoretical cross-sectional area of  $9.42 \text{ mm}^2$  obtained from the sample's solid model.



The second trend observed through the data is the reduction in the cross-sectional area due to the increased tensile load. As seen in Figure 4-11 b), the cross-sectional area has reduced between 0.4-1.8% of the preloaded condition. Furthermore, the mean area's observation shows a resulting reduction in the area of  $0.0932 \text{ mm}^2$  and  $0.125 \text{ mm}^2$  or 0.9607% and 1.2880% from the preloaded state to 150 N and 200 N, respectively. This reduction in the cross-sectional area is reflected in a later section discussing the resolved DVC strain data. As a final note, as seen in Figure 4-10 a) the reduction of the cross-section is more significant between the 100 N to 150 N load than between the 150 N to 200 N. This is indicative of an increase in sample stiffness, which will be discussed in the porosity and air gap measurement section of this report.

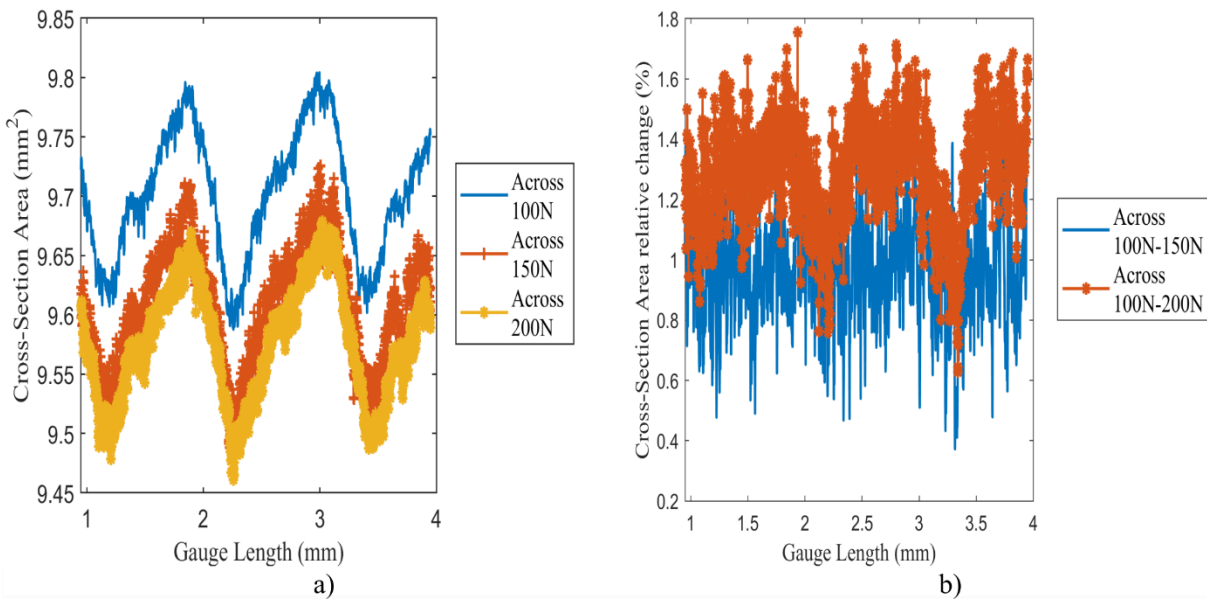


Figure 4-11: Variation of cross-section area through 3mm section of the sample: a) cross-section area variation through 3mm gauge length of the sample, b) percentage change of cross-section area compared to 100 N load

Table 4-7: Statistical analysis of the cross-section area for different load conditions

Sample Load	Mean Cross-Section Area (mm <sup>2</sup> )	Percent Change from 100 N load	Standard Deviation
100 N	9.7013	-	±0.0536
150 N	9.6081	0.9607	±0.0681
200 N	9.5763	1.2880	±0.0493

### 4.3.1.3 Air Gap Analysis

Before making a quantitative assessment of the air gap volume, it is crucial to discuss the qualitative benefits of performing this CT segmentation procedure. As seen in Figure 4-8 d), segmenting out the sample air gaps, the print pattern can easily be identified. Within the sample, there are two significant sources of pores that can be recognized. The first source of porosity is between the sample's shell layers and the infill of the material. The second is between the supporting infill raster of the material. As expected, these air gaps occur between the raster at an approximate +45°/-45° angle as specified by the print parameters. The orientation of these air gaps will play a significant role in assessing strain within the sample. As previously discussed by Tao *et al.*, features contained by air gaps support more of the tensile force [48].

The total air gap volume is shown in Table 4-8. It is evident that even though the samples were sliced to be produced with an infill density of 100%, air gaps are still present between raster. As calculated through the CT segmentation procedure, the actual infill density lies between 99.2% to 99.5% as force is applied. As a result of the increasing tensile load samples, pores and air gaps begin to close. The changes in air gap size can be detected using the  $\mu$ -CT analysis process. The closure of these air gaps is not linearly proportional to the applied load. The reason being is as these air gaps begin to close, there is a resultant increase in the young's modulus of the sample [16]. This increase in stiffness is likely why the decrease in cross-sectional area between the 100 N to 150 N is much more significant than between 150 N to 200 N.

Table 4-8: Air gap volume and actual sample infill density measured for a 3 mm section through  $\mu$ -CT

Applied Force (N)	Air Gap Volume (mm <sup>3</sup> )	True infill (%)
100	0.025	99.2
150	0.020	99.4
200	0.017	99.5

### **4.3.2 Digital Volume Correlation of Downsampled data**

#### **4.3.2.1 Sample Displacement**

While a wealth of information about the sample's manufacturing and surface-level microstructure changes can be obtained strictly from sample segmentation, the DVC method was utilized for precise volumetric displacement and strain measurements. The longitudinal displacement fields are shown in Figure 4-12. Figure 4-12 provides two views of the resulting displacement fields between the preload condition of 100 N and the 150 N load and 200 N load. The longitudinal displacement is displayed with an isometric view and view of the XZ plane from the sample's direct center. The isometric view aims to provide a 3D view of displacement fields and highlight the displacement variation within the 3D space. This view of experimental displacement variation within 3D space is only possible to obtain via DVC. Simultaneously, the XZ plane's displacement provides a detailed perspective of the total variation along the sample's gauge length.

The gradient of displacements through the sample shows a typical development to ones obtained from DIC for +45°/-45° FFF samples under tensile loading [49]. There is a displacement of 28  $\mu$ m for the 100-150 N test, and 71  $\mu$ m for the 100-200 N test at the samples end closest to the load cell. This displacement slowly decreases toward the static end of the load cell. One would

expect that at the stationary face, the displacement to be 0, but there is a small concentration of displacement present. The absence of an absolute static end is likely to present due to a lack of rigidity within the MTS, leading to a small region of longitudinal displacement.

While the displacement development is similar to ones obtained through DIC, a distinction can be made between the two based on the displacement pattern. Previous DIC results show longitudinal displacement in horizontal bands from the tensile face through the sample [49]. DVC results from this study show the development of strain in angular segments throughout the piece. A probable cause for the evolution of displacement in this manner is due to incongruent loading between two the load pins attached to the sample's end tabs. The development of this incongruent loading is possibly due to the nozzle starting position creating a stress concentration at the end of one side of the gauge length. This loading would result in a single end receiving slightly higher force than the other face, leading to angular displacement. Additionally, as previously mentioned, the MTS's lack of rigidity could also contribute to unsymmetrical loading conditions. While this is a potential source of error, the purpose of this study is to prove the validity of DVC for displacement and strain analysis of FFF parts. Thus, the resulting strain field will be analyzed under the presumption that the developed force within the tensile coupon has been applied on a slight angle.

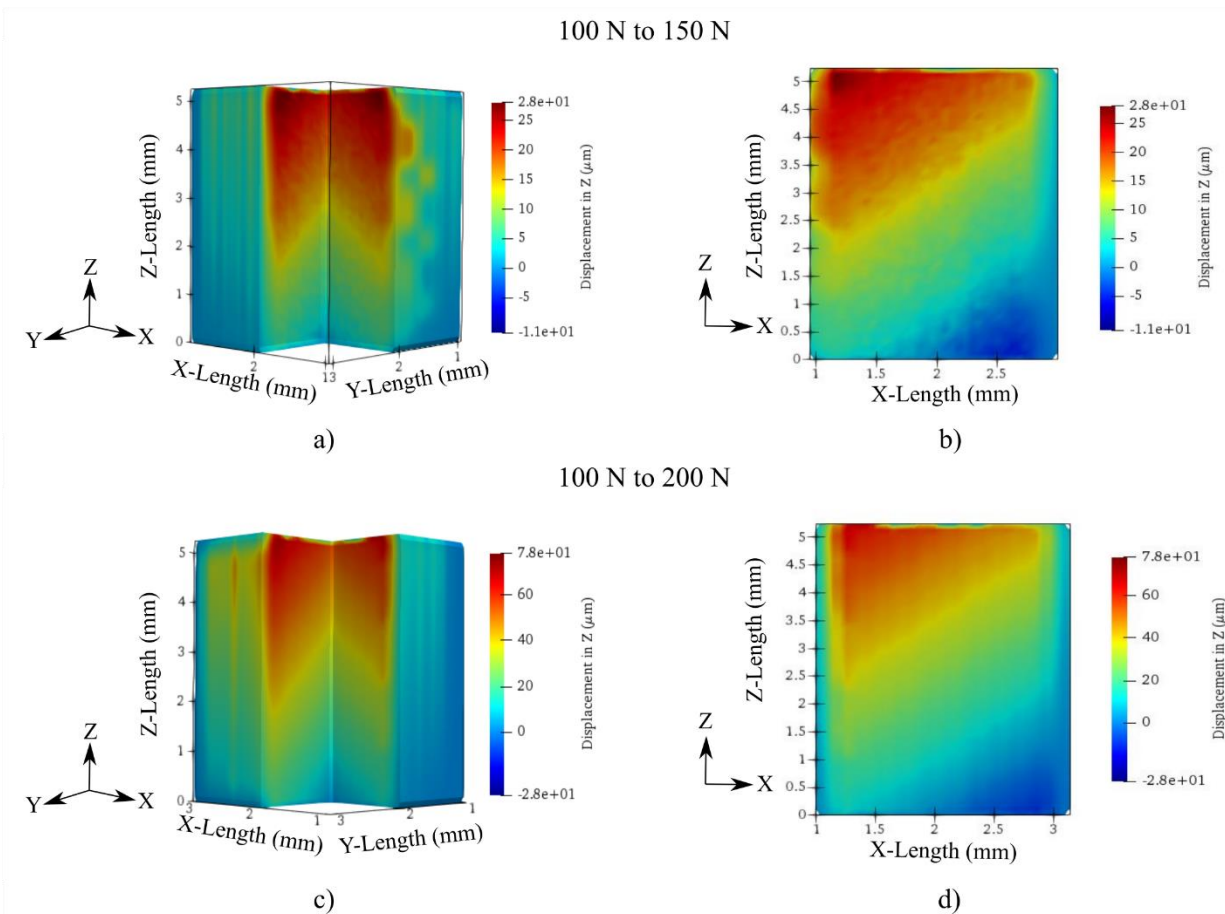


Figure 4-12: Displacement in direction (z-axis) of tensile load: a) isometric view of displacement for 100-150 N test, b) XZ plane displacement for 100-150 N test, c) isometric view of displacement 100-200 N test, d) XZ plane view of displacement for 100-200 N test

**4.3.2.2 Sample Strain Analysis**

Figure 4-13 displays an isometric view and XZ plane view of strain for the sample. Similarly to the displacement, this demonstrates a variation of the strain in 3D space and provides a detailed outlook of strain in a single plane. Additionally, Figure 4-13 shows the 1D development of strain along the x-axis about the samples' center. Two loading states between the coupon are shown here, the first being between 100 N and 150 N and the second between 100 N and 200 N. It is seen that the strain develops mostly on the outer surface of the material, particularly within the shell of the sample. Comparing the isometric view to the XZ plane view, a positive strain is shown to develop on the shell's leftward face and the area closest to the build plate. In contrast, the negative

strain is realized in the sample's rightward front and face furthest from the build plate. As expected, the strain between the 100 N and 200 N test is greater than the 100 to 150 N test indicating the overall cross-sectional contraction in the x-direction as the load increases.

Figure 4-14 demonstrates the isometric view and XZ plane for both the 100 N to 150 N load step and the 100 N to 200 N load step. As expected, the strain increased between the two different loading conditions. The transverse strain,  $\epsilon_{yy}$ , is shown to develop on the sample's outer faces similar to that of the strain  $\epsilon_{xx}$ . This similarity is seen on the material's shell as the leftward shell face is in positive strain, and the rightward face is experience strain in the opposite direction. For  $\epsilon_{yy}$ , the strain on the sample face closest to the build plate is negative, while the face furthest from the build plate is positive.

Analyzing Figure 4-13 and Figure 4-14 in conjunction provides details on the strain similarities between the transverse strain and the sample's overall behavior. The development of strain in the transverse direction indicates the overall contraction of the coupon. It is notably shown that the material's shell is reducing in size in the XY plane. This size reduction is reflected in the  $\mu$ -CT tomographs, demonstrating an overall cross-sectional area across this sample plane. The development of strain within the shell of the sample is not entirely unprecedented. As previously mentioned, it has been reported that a higher concentration of force is supported within features that have surrounding air gaps [48]. As observed in Figure 4-4 and Figure 4-7, large air gaps exist between the material's shell and the infill. Thus, the material's outer shell is likely bearing a more significant portion of stress, which is reflected through the development of strain.

Precise quantification of the transverse strain is plotted in Figure 4-13 (e) and Figure 4-14 (e). The data shown within these graphics were collected by plotting the 1D strain variation across the x-direction from the sample's midpoint. The analysis of strain development of the material is

reflected within these plots. Strain  $\epsilon_{xx}$  and  $\epsilon_{yy}$  are shown to peak approximately evenly on each face of the material. The 100 to 150 N dataset strain  $\epsilon_{xx}$  is between 0.03 to -0.035, and  $\epsilon_{yy}$  is between 0.069 to -0.080. The 100 to 200 N strain  $\epsilon_{xx}$  is between 0.083 to -0.081, and  $\epsilon_{yy}$  is between 0.157 to -0.125. The transverse strain peaks occur on the test samples' outer faces, which are associated with the material shell. Measuring the mean width of the peaks for the 100 to 150 N and 100 to 200 N data, the strain peaks' size is 0.78 mm and 0.75 mm. It can be seen that the size of these peaks relates closely to the slicer shell thickness shown in Table 4-1.

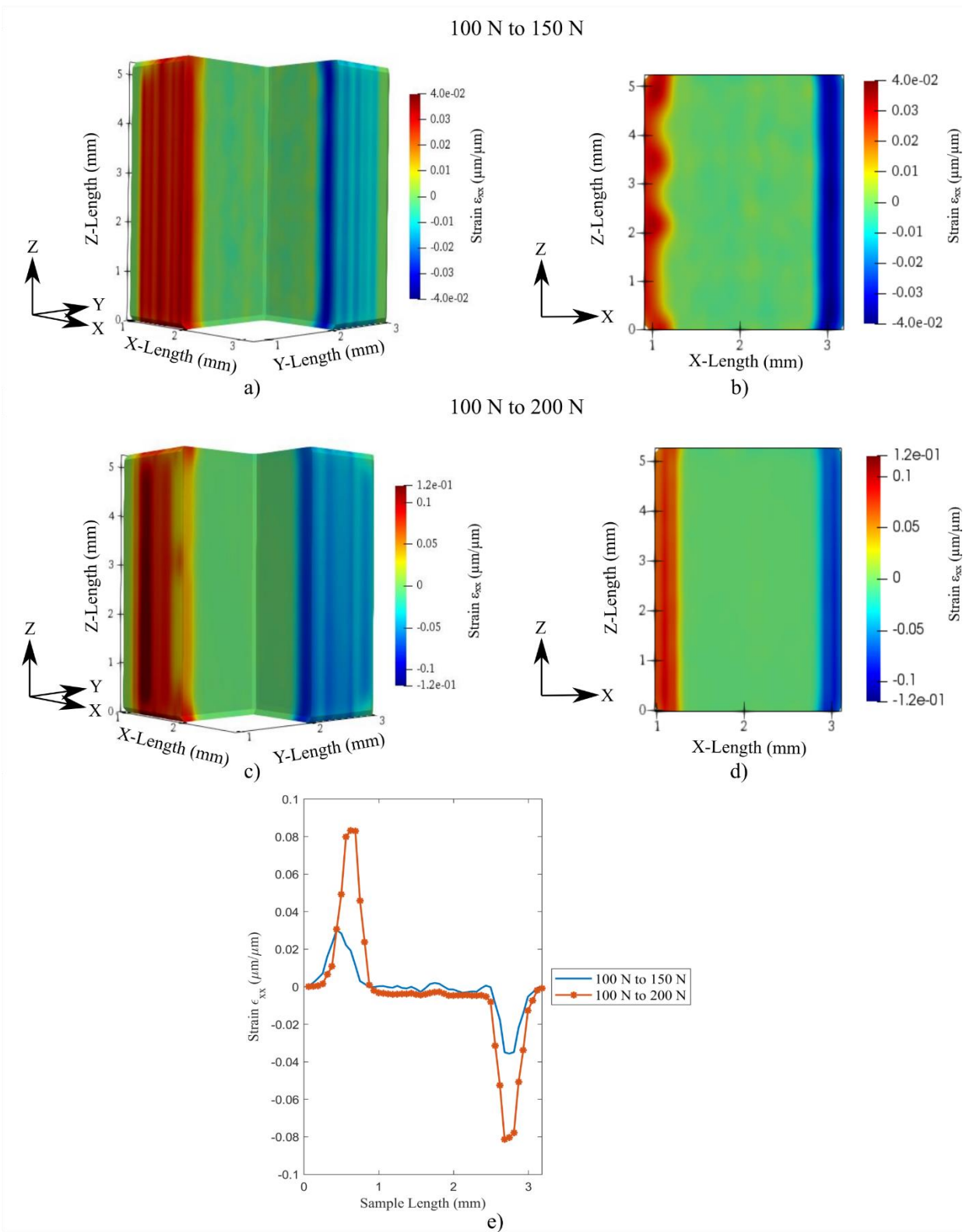


Figure 4-13: Volumetric strain  $\epsilon_{xx}$  developed through the sample: a) isometric view of 100 to 150 N test, b) XZ plane view of 100 to 150 N test, c) isometric view of 100 to 200 N test, d) XZ plane view of 100 to 200 N test, e) strain profile across the sample width.



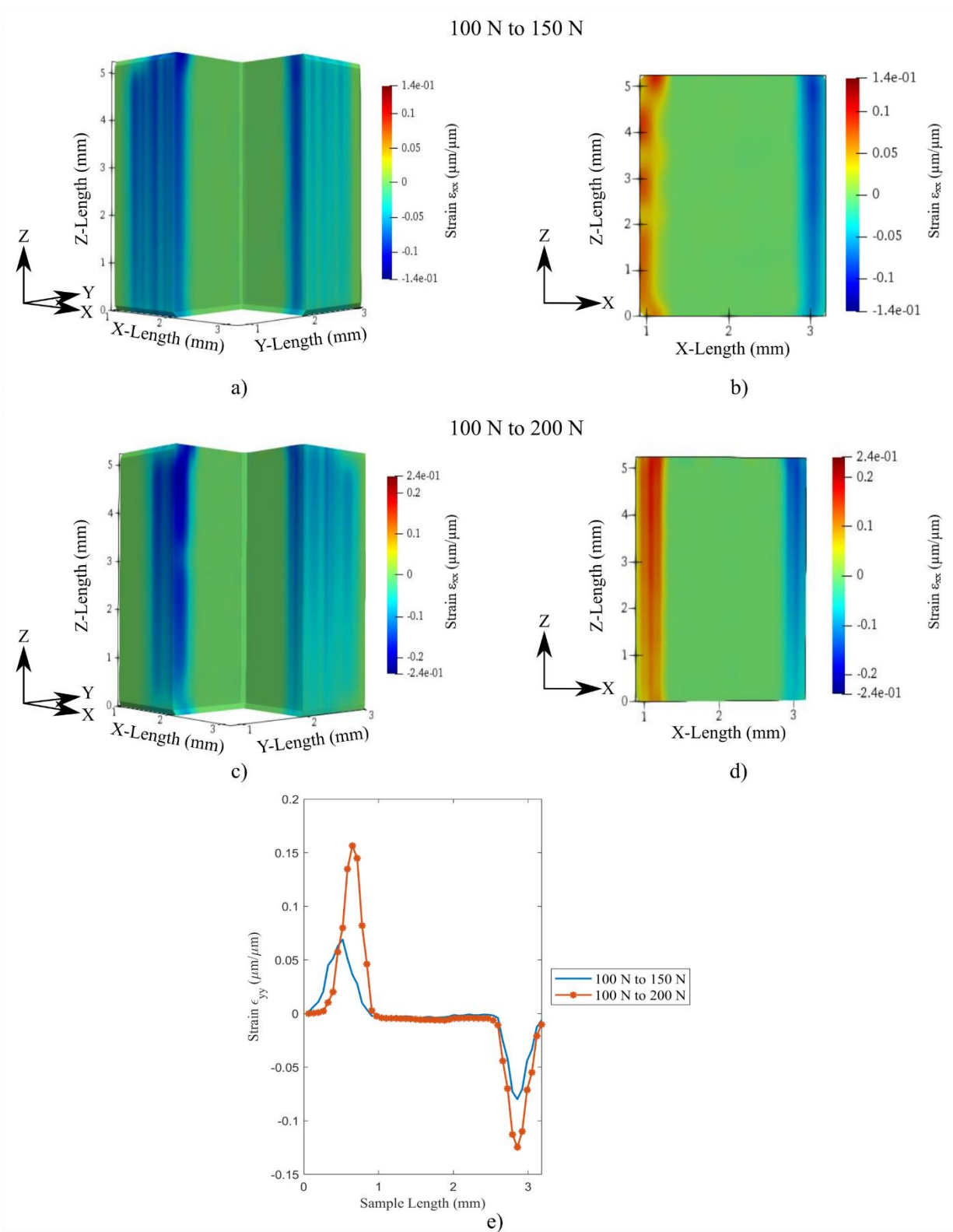


Figure 4-14: Volumetric  $\epsilon_{yy}$   $yy$  developed through the sample: a) isometric view of 100 to 150 N test, b) XZ plane view of 100 to 150 N test, c) isometric view of 100 to 200 N test, d) XZ plane view of 100 to 200 N test, e) strain profile across the sample width.

The longitudinal strain ( $\epsilon_{zz}$ ) uniquely does not develop on the sample's shell but within the sample cross-section. This difference in strain development is indicative of the anisotropic and nonhomogeneous deformation of the sample. In Figure 4-15 a) and Figure 4-15 b), the longitudinal strain develops within the infill at an angle. As the load is increased to 200 N, strain within the sample forms in periodic diagonal bands within the material's bulk. These diagonal bands of strain appear to form at a 45° angle within the sample's internal layers, which coincide directly with the raster infill pattern. This strain pattern has previously been seen for FFF printed parts within 2D DIC studies but has not been previously shown volumetrically [49]. Notably is the lack of strain forming on the -45° raster. This lack of strain development at a -45° angle relates to the previous discussion concerning the displacement fields. As previously mentioned, the sample is likely to be loaded on a slight angle. This uneven loading experienced by the sample results in the 45° bearing the majority of the load, while the -45° experience minimal loading.

Figure 4-15 (c) displays the 1D strain through the material's gauge length about its center. The 100-150 N test is visibly less smooth, indicating the beginning formation of strain within the sample. Subsequently, the 100-150 N presents a bimodal profile indicating only the initial strain formation within a few rasters. Observation of the 100-200 N test shows a much smoother profile, representing neatly formed bands of strains. An approximation of the strain band size was made from the strain data, resulting in mean size of 0.489 mm in width. This length relates directly to the rasters' measure, which should have a theoretical size of 0.4 mm in width based on the nozzle size. The increase in raster size can be attributed to the DVC data's discretization and the approximation made by not calculating the raster geometry directly perpendicular to the raster print direction. As a final comment, the longitudinal strain on the sample can be seen to be much smaller than the transverse strain shown figures Figure 4-13 and Figure 4-14. This is a direct result

of the transverse strain developing on the sample's shell, directly in line with the load [48]. Thus, the material's shell bearing a more substantial portion of the force and consequently experiences higher strain. Both the DVC transverse and longitudinal strain results can provide useful inputs for creating a complete FEA of FFF composites [30]–[33].

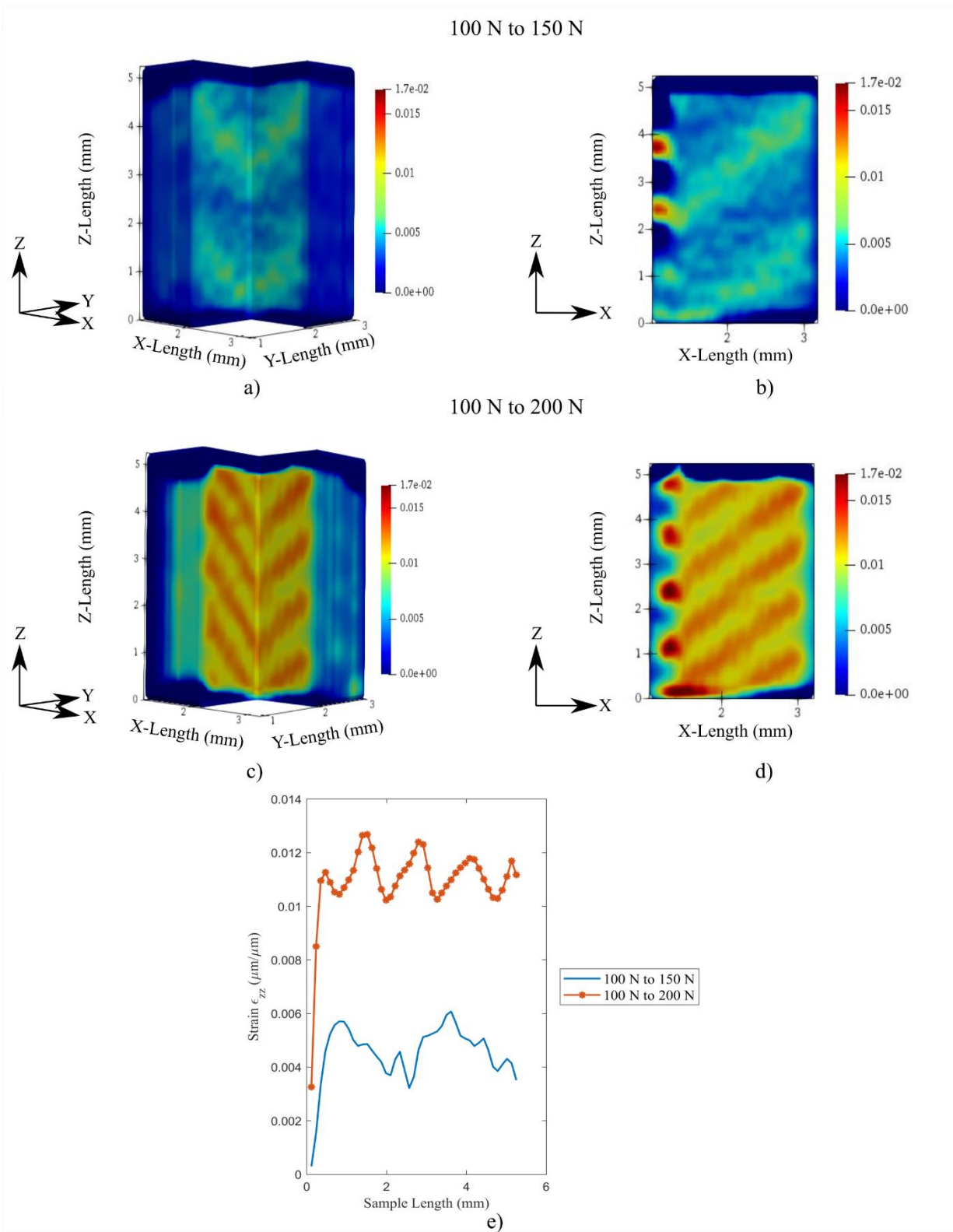


Figure 4-15: Volumetric strain  $\epsilon_{zz}$  developed through the sample: a) isometric view of 100 to 150 N test, b) XZ plane view of 100 to 150 N test, c) isometric view of 100 to 200 N test, d) XZ plane view of 100 to 200 N test, e) strain profile across the sample width.

#### 4.4 Conclusions

A uniaxial tensile test at three loads was conducted on a 3D printed copper reinforced PLA tensile coupon in-situ with a  $\mu$ -CT. According to ASTM-D648 14 Type V standards, the tensile coupon's geometry was made with slight modifications to ensure compatibility with the utilized MTS. As a preliminary step toward the analysis displacement and strain analysis, the sample's bulk structural response was measured through  $\mu$ -CT image segmentation. The specimen was shown to have a bulk cross-sectional area larger than the solid model used to develop FFF but still within the printer tolerance. As the sample's load increased, it was clear that the mean cross-sectional area was reduced due to the sample's elongation. However, the sample cross-section decrease was much more significant between the 100-150 N than 150-200 N indicating an increase in material stiffness as the sample was strained. The raster air gap was segmented from the sample and measured to support this statement. Two significant air gaps contributed to the sample's porosity: 1) air gaps between the samples shell and infill, and 2) between the infill rasters. The formation of airgaps was aided in the analysis strain as features surrounded by air gaps are seen as regions that bear significantly more loading [48]. The resulting volume of the air gaps showed a decrease in porosity as a tensile force increase, which has previously been shown to relate to a rise in sample stiffness [16].

After segmenting the samples to determine DVC image compatibility, the resulting images were used as input into an open-source DVC software, FIDVC, to obtain the tensile coupon's internal displacement and strain behaviour Lagrangian linear elastic strain formulation. Sample displacement had a similar gradient to typical tensile tests but was developed on an angle due to potential incongruent force application from the load cell. Thus all analysis for the strain fields was considered under the pretense of a slightly angular load condition. The resulting strain fields

showed the effects of printing geometry on the development of strain within the sample. The axial strain on the part was developed on the 3D printed structure's surrounding faces, which relates to the overall reduction in the cross-sectional area seen from the image segmentation study. The development of this strain appears to form in 0.75-0.78 mm, which is associated with the shell thickness printing parameter

The longitudinal strain was shown to develop within the bulk of the material along the internal rasters uniquely. The development of strain along the rasters rather than the shell is due to the angularity of the rasters. The strain was observed to only develop on the +45° degree raster, but not the -45° raster, which relates to the force of load cell being skewed in +45° raster direction. Furthermore, the longitudinal strain developed within the sample was much less than the axial strain due to the shell's alignment compared to the rasters. The sample shell in direct alignment with the load direction will bear a much higher degree of force than the rasters. DVC's ability to capture the internal strain behavior provides a necessary first step towards a greater understanding of 3D printed composites' deformation behaviour. Future work on the effects of different print parameters and loads is essential for a complete understanding of these materials' mechanical behaviour using the DVC measurement method. Additionally, these results can help build more intricate FEA models of FFF materials and allow for FFF parts to reach full potential in industrial applications.

#### **4.5 References**

- [1] P. S. Ujeniya and N. V. Rachchh, "A review on Manufacturing, Machining, and recycling of 3D printed composite materials.," *IOP Conf. Ser. Mater. Sci. Eng.*, vol. 653, no. 1, 2019.
- [2] Y. Sano, R. Matsuzaki, M. Ueda, A. Todoroki, and Y. Hirano, "3D printing of discontinuous and continuous fibre composites using stereolithography," *Addit. Manuf.*,

- vol. 24, pp. 521–527, 2018.
- [3] S. Hwang, E. I. Reyes, K. sik Moon, R. C. Rumpf, and N. S. Kim, “Thermo-mechanical Characterization of Metal/Polymer Composite Filaments and Printing Parameter Study for Fused Deposition Modeling in the 3D Printing Process,” *J. Electron. Mater.*, vol. 44, no. 3, pp. 771–777, 2015.
  - [4] B. Wang, L. Sun, and B. Pan, “Mapping internal deformation fields in 3D printed porous structure with digital volume correlation,” *Polym. Test.*, vol. 78, 2019.
  - [5] R. J. Zaldivar, D. B. Witkin, T. McLouth, D. N. Patel, K. Schmitt, and J. P. Nokes, “Influence of processing and orientation print effects on the mechanical and thermal behavior of 3D-Printed ULTEM ® 9085 Material,” *Addit. Manuf.*, vol. 13, pp. 71–80, 2017.
  - [6] I. Blanco, “The Use of Composite Materials in 3D Printing,” *J. Compos. Sci.*, vol. 4, no. 42, 2020.
  - [7] B. Pan, K. Qian, H. Xie, and A. Asundi, “Two-dimensional digital image correlation for in-plane displacement and strain measurement: A review,” *Meas. Sci. Technol.*, vol. 20, no. 6, 2009.
  - [8] J. J. Orteu, “3-D computer vision in experimental mechanics,” *Opt. Lasers Eng.*, vol. 47, no. 3–4, pp. 282–291, 2009.
  - [9] H. Goodarzi Hosseinabadi, R. Bagheri, L. Avila Gray, V. Altstädt, and K. Drechsler, “Plasticity in polymeric honeycombs made by photo-polymerization and nozzle based 3D-printing,” *Polym. Test.*, vol. 63, pp. 163–167, 2017.
  - [10] H. Goodarzi Hosseinabadi, R. Bagheri, and V. Altstädt, “Shear band propagation in honeycombs: numerical and experimental,” *Rapid Prototyp. J.*, vol. 24, no. 2, pp. 477–484, 2018.
  - [11] S. K. Boyd, “Micro-computed tomography,” in *Advanced Imaging in Biology and Medicine: Technology, Software Environments, Applications*, 2009, pp. 3–25.
  - [12] M. J. Paulus, S. S. Gleason, S. J. Kennel, P. R. Hunsicker, and D. K. Johnson, “High

- Resolution X-ray Computed Tomography: An Emerging Tool for Small Animal Cancer Research,” *Neoplasia*, vol. 2, no. 1–2, 2000.
- [13] R. Bibb, D. Thompson, and J. Winder, “Computed tomography characterisation of additive manufacturing materials,” *Med. Eng. Phys.*, vol. 33, no. 5, pp. 590–596, 2011.
- [14] I. Gajdoš and J. Slota, “Influence of printing conditions on structure in FDM prototypes,” *Teh. Vjesn.*, vol. 20, no. 2, pp. 231–236, 2013.
- [15] A. Thompson, I. Maskery, and R. K. Leach, “X-ray computed tomography for additive manufacturing: A review,” *Meas. Sci. Technol.*, vol. 5, no. 3, 2016.
- [16] X. Wang, L. Zhao, J. Y. H. Fuh, and H. P. Lee, “Effect of porosity on mechanical properties of 3D printed polymers: Experiments and micromechanical modeling based on X-ray computed tomography analysis,” *Polymers (Basel)*, vol. 11, no. 7, 2019.
- [17] B. K. Bay, T. S. Smith, D. P. Fyhrie, and M. Saad, “Digital volume correlation: Three-dimensional strain mapping using x-ray tomography,” *Exp. Mech.*, vol. 39, no. 3, pp. 217–226, 1999.
- [18] M. Peña Fernández, A. H. Barber, G. W. Blunn, and G. Tozzi, “Optimization of digital volume correlation computation in SR-microCT images of trabecular bone and bone-biomaterial systems,” *J. Microsc.*, vol. 272, no. 3, pp. 213–228, 2018.
- [19] B. C. Roberts, E. Perilli, and K. J. Reynolds, “Application of the digital volume correlation technique for the measurement of displacement and strain fields in bone: A literature review,” *J. Biomech.*, vol. 47, no. 5, pp. 923–934, 2014.
- [20] F. Gillard *et al.*, “The application of digital volume correlation (DVC) to study the microstructural behaviour of trabecular bone during compression,” *J. Mech. Behav. Biomed. Mater.*, vol. 29, pp. 480–499, 2014.
- [21] H. Tran, P. Doumalin, C. Delisee, J. C. Dupre, J. Malvestio, and A. Germaneau, “3D mechanical analysis of low-density wood-based fiberboards by X-ray microcomputed tomography and Digital Volume Correlation,” *J. Mater. Sci.*, vol. 48, no. 8, pp. 3198–3212, 2013.



- [22] T. F. Morgeneyer, L. Helfen, H. Mubarak, and F. Hild, “3D Digital Volume Correlation of Synchrotron Radiation Laminography Images of Ductile Crack Initiation: An Initial Feasibility Study,” *Exp. Mech.*, vol. 53, pp. 543–556, 2013.
- [23] T. F. Morgeneyer *et al.*, “In situ 3-D observation of early strain localization during failure of thin Al alloy (2198) sheet,” *Acta Mater.*, vol. 69, pp. 78–91, 2014.
- [24] R. Brault, A. Germaneau, J. C. Dupré, P. Doumalin, S. Mistou, and M. Fazzini, “In-situ Analysis of Laminated Composite Materials by X-ray Micro-Computed Tomography and Digital Volume Correlation,” *Exp. Mech.*, vol. 53, no. 7, pp. 1143–1151, 2013.
- [25] M. Mostafavi *et al.*, “Yield behavior beneath hardness indentations in ductile metals, measured by three-dimensional computed X-ray tomography and digital volume correlation,” *Acta Mater.*, vol. 82, pp. 468–482, 2015.
- [26] P. Lecomte-Grosbras, J. Réthoré, N. Limodin, J. F. Witz, and M. Brieu, “Three-Dimensional Investigation of Free-Edge Effects in Laminate Composites Using X-ray Tomography and Digital Volume Correlation,” *Exp. Mech.*, vol. 55, no. 1, pp. 301–311, 2015.
- [27] J. F. Gonzalez, D. A. Antartis, M. Martinez, S. J. Dillon, I. Chasiotis, and J. Lambros, “Three-Dimensional Study of Graphite-Composite Electrode Chemo-Mechanical Response using Digital Volume Correlation,” *Exp. Mech.*, vol. 58, no. 4, pp. 573–583, 2018.
- [28] A. Mendoza, J. Schneider, E. Parra, E. Obert, and S. Roux, “Differentiating 3D textile composites: A novel field of application for Digital Volume Correlation,” *Compos. Struct.*, vol. 208, pp. 735–743, 2019.
- [29] E. Bar-Kochba, J. Toyjanova, E. Andrews, K. S. Kim, and C. Franck, “A Fast Iterative Digital Volume Correlation Algorithm for Large Deformations,” *Exp. Mech.*, vol. 55, no. 1, pp. 261–274, 2015.
- [30] M. Somireddy and A. Czekanski, “Mechanical Characterization of Additively Manufactured Parts by FE Modeling of Mesostructure,” *J. Manuf. Mater. Process.*, vol. 1, no. 2, 2017.

- [31] P. J. Baikerikar and C. J. Turner, "Comparison of as-built fea simulations and experimental results for additively manufactured dogbone geometries," in *Proceedings of the ASME Design Engineering Technical Conference*, 2017.
- [32] A. Cattenone, S. Morganti, G. Alaimo, and F. Auricchio, "Finite element analysis of additive manufacturing based on fused deposition modeling: Distortions prediction and comparison with experimental data," *J. Manuf. Sci. Eng. Trans. ASME*, vol. 141, no. 1, 2019.
- [33] B. K. Bay, "Methods and applications of digital volume correlation," *J. Strain Anal. Eng. Des.*, vol. 43, no. 8, pp. 745–760, 2008.
- [34] ASTM-D638-14, "Standard Test Method for Tensile Properties of Plastics," *ASTM Stand.*, 2014.
- [35] M. N. Sudin, S. A. Shamsudin, and M. A. Abdullah, "Effect of part features on dimensional accuracy of fdm model," *ARPJ. Eng. Appl. Sci.*, vol. 11, no. 13, pp. 8067–8072, 2016.
- [36] Bruker-MicroCT, "Method note An overview of NRecon : reconstructing the best images from your microCT scan." Bruker-MicroCT, Kontich, pp. 1–48, 2013.
- [37] J. F. Barrett and N. Keat, "Artifacts in CT: Recognition and avoidance," *Radiographics*, vol. 24, no. 6, 2004.
- [38] C. Timpano, H. Abdoli, S. N. Leung, and G. W. Melenka, "Characterization of open-cellular polymeric foams using micro-computed tomography," *Polymer (Guildf)*, vol. 202, 2020.
- [39] A. F. Bower, *Applied mechanics of solids*. 2009.
- [40] Z. Liu, Q. Lei, and S. Xing, "Mechanical characteristics of wood, ceramic, metal and carbon fiber-based PLA composites fabricated by FDM," *J. Mater. Res. Technol.*, vol. 8, no. 5, pp. 3741–3751, 2019.
- [41] M. Gates, J. Gonzalez, J. Lambros, and M. T. Heath, "Subset Refinement for Digital Volume Correlation: Numerical and Experimental Applications," *Exp. Mech.*, vol. 55, pp.

- 245–259, 2015.
- [42] J. Gonzalez and J. Lambros, “A Parametric Study on the Influence of Internal Speckle Patterning for Digital Volume Correlation in X-Ray Tomography Applications,” *Exp. Tech.*, vol. 40, no. 5, pp. 1447–1459, 2016.
- [43] B. Pan, Z. Lu, and H. Xie, “Mean intensity gradient: An effective global parameter for quality assessment of the speckle patterns used in digital image correlation,” *Opt. Lasers Eng.*, vol. 48, no. 4, pp. 469–477, 2010.
- [44] J. Lambros and J. Patel, “Microscale digital image correlation study of irradiation induced ductile-to-brittle transition in polyethylene,” *J. Strain Anal. Eng. Des.*, vol. 46, no. 5, pp. 347–360, 2011.
- [45] B. Pan, Z. Wang, and H. Xie, “Generalized spatial-gradient-based digital image correlation for displacement and shape measurement with subpixel accuracy,” *J. Strain Anal. Eng. Des.*, vol. 44, no. 8, pp. 659–669, 2009.
- [46] N. Limodin, J. Réthoré, J. Adrien, J. Y. Buffière, F. Hild, and S. Roux, “Analysis and Artifact Correction for Volume Correlation Measurements Using Tomographic Images from a Laboratory X-ray Source,” *Exp. Mech.*, vol. 51, no. 6, 2011.
- [47] B. P. Croom, H. Jin, B. Mills, and X. Li, “Effect of Fragile Speckle Patterns on Accuracy of Digital Volume Correlation,” *Exp. Mech.*, vol. 49, no. 7, pp. 991–1005, 2019.
- [48] Y. Tao, P. Li, and L. Pan, “Improving tensile properties of polylactic acid parts by adjusting printing parameters of open source 3D printers,” *Medziagotyra*, vol. 21, no. 1, pp. 83–87, 2020.
- [49] J. T. Cantrell *et al.*, “Experimental characterization of the mechanical properties of 3D-printed ABS and polycarbonate parts,” *Rapid Prototyp. J.*, vol. 23, no. 4, 2017.

## Chapter 5: Conclusions, Recommendations, and Future Works

### 5.1 Conclusions

This thesis aims to utilize the novel DVC measurement technique to assess and examine advanced materials. A comprehensive literature review was first conducted to provide the necessary background knowledge in composites and digital measurement techniques. Composites were shown to have many material properties that make them attractive as an engineering design material, such as their lightweight, high strength, and material tailorability. However, composites are often difficult to analyze due to inhomogeneous deformation fields and anisotropic material properties. Thus, traditional contact-based methods for measuring deformation, such as strain gauges and extensometers, cannot capture the actual sample deformation.

Two alternatives were shown to exist in digital image correlation (DIC) and digital volume correlation (DVC). DIC is the more established of the two methods and provides a full-field view of displacement and strain but can only capture in-plane and out-of-plane motion of the sample's surface. For precise measurements within the bulk of a material, the novel DVC technique is required. Thus, for complete measurement of the internal displacement and strain behaviour DVC is utilized in this study. However, as DVC is relatively new, the supporting literature surrounding it is less developed than DIC or other material measurement methodologies. It was the purpose of this thesis to begin to address these current gaps in the literature. This work focused on how to obtain and assess sample quality for DVC measurements and utilize DVC to analyze fused filament fabrication (FFF) printed composites, which are two areas where the current literature is still limited.

To meet the end goal of applying the DVC technique to composite structures, developing a method for obtaining and assessing high-quality images for DVC measurements was critical. It

was determined that the artificial seeding technique, a technique that has previously seen successful results in a relatively limited amount of studies, was a potential candidate for achieving the desired image contrast. However, to implement this technique, an investigation of the advantages and sources of error were required.

Achievement of this goal was undergone by seeding epoxy with five different marker particles: 200  $\mu\text{m}$  copper, 50  $\mu\text{m}$  copper, 25  $\mu\text{m}$  copper, 50  $\mu\text{m}$  zirconium oxide, and 10  $\mu\text{m}$  aluminum nitride. As a preliminary step to assess the seeding particle technique, a micro-computed tomography ( $\mu\text{-CT}$ ) segmentation analysis was first performed to analyze and measure the greyscale distribution, particle quantity, and particle distribution within a single correlation window. It was shown that each particle provided a greyscale distribution to the sample that would contribute toward proper correlation. The seeding particles could be measured and locations pinpointed within the correlation window by utilizing image segmentation techniques. Each particle met the correlation recommendation of 27 particles per subset for the 128 x 128 x 128 voxel correlation window. The 200  $\mu\text{m}$  copper was just above the limit at 29 particles, and the 25  $\mu\text{m}$  copper contained the most features with 484 particles. Finally, there was no significant particle clumping source, with each sample having a unimodal distribution of particles at different distances from the correlation windows center.

A rigid body displacement (RBD) test was performed for each seeding particle to assess the accuracy and narrow the optimal DVC inputs. The seeding particles were digitally displacement rather than experimentally to decouple the effects of seeding from the tolerance of a load cell or micro-positioning stages. This procedure was determined to provide more accurate results than displacing them experimentally. For each sample, it was shown that as the correlation window size was increased from 32 x 32 x 32 voxel to 128 x 128 x 128, the error on displacement diminished,

with the 25  $\mu\text{m}$  copper particles proving to be the most accurate across the three subsets studied. Thus, the 25  $\mu\text{m}$  copper particles were selected as the most optimal seeding particle and were utilized to determine the percent overlap necessary for analysis. A final study was done to examine the error associate with downsampling. Downsampling was shown to introduce some error to the displacement data but was still useful in studying displacement for a hole-in epoxy coupon that had been compressed. This usefulness was mainly due to downsampling, reducing the computational workload resulting from the full-resolution images.

The longitudinal displacement within the sample was shown to form in three bands, all radiating from the center hole. Each displacement band was associated with a different region of the epoxy. The top-end designated the static face, the bottom band designated the compressive end, and the side bands the outward expansion of the sample. Precise measurements of displacement were highlighted by undergoing a full resolution analysis around the center hole. This method of utilizing downsampled data to obtain a full sample view of deformation has allowed for identifying smaller regions of interest to perform the DVC at full resolution. The equivalent strain was shown to develop in two areas: the center hole and the sample's perimeter. The strain on the border of the epoxy was likely a result of RBD and edge effects. However, the second region of high strain is located around the center hole due to deformation around a strain concentration. An accurate and more defined strain gradient was shown to propagate from the center by utilizing the full-resolution data.

With the particle seeding technique's success at providing strong  $\mu\text{-CT}$  image contrast, the method was put into practice for FFF material testing. A polylactic acid (PLA) filament commercially impregnated with copper micro-particles was examined to extend the knowledge gained in the previous study. Tensile coupons were printed utilizing a commercially purchased

FFF 3D printer according to a modified ASTM D638-14 Type 5 design. The coupon's important printing parameters were the  $+45^\circ/-45^\circ$  raster orientation, 100 percent infill density, nozzle size of 0.4 mm, and shell thickness of 0.8 mm. Samples were loaded and imaged at three load states 100 N (preload), 150 N, and 200 N.

One of the notable advantages of the DVC technique is the amount of data obtained and analyzed from the  $\mu$ -CT images before correlation. Examining the sample's cross-sectional area highlighted the printer's dimensional tolerance and an overall reduction in cross-sectional area derived from the tensile load. Additionally, air gaps were segmented from the rasters and shown to form at alternating  $+45^\circ/-45^\circ$ . Two significant air gaps existed within the sample: ones along the internal rasters and ones between the materials shell and infill. Identification of these air gaps within the coupon plays a critical role in understanding the displacement and strain behaviour as features between them support a high degree of tensile force. The real infill percent and its variation with loading could be quantified through measurement of the air gap volume.

Due to the lack of stiffness of the PLA sample and imaging parameters utilized to capture the deformation, it was required to downsample the data by a quarter of its initial resolution to capture the displacement. The longitudinal displacement showed of the sample at each load condition showed an angular gradient from the loading end to the static end. The displacement gradient's angularity was likely due to the incongruent load between the pins due to the nozzle start position creating a stress concentration near one end. The displacement gradient played an essential role in understanding the longitudinal strain behaviour as the rasters angled toward this direction bore most of the load. The strain result of the transverse load showed the overall sample contraction. Additionally, the transverse strain manifested itself on the out surfaces of the material, the most important of which was the shell. In comparison, the longitudinal strain was shown to

develop on the internal rasters. Of final note, the shell's strain was a greater magnitude than the rasters' strain, as the shell was in direct alignment with the tensile force, thus bearing the majority of the strain.

This thesis's key finding showed the particle seeding technique's successfulness to acquire sufficient contrast patterns for DVC. While each seeding particle seemed to provide accurate displacement measurement across the 64 x 64 x 64 voxel subset and 128 x 128 x 128, inaccuracies began to form when the subset was reduced to 32x32x32 voxels. However, across all subsets, the 25  $\mu\text{m}$  copper particles were shown to provide the highest degree of accuracy. This accuracy resulted from a random distribution of higher density particles existing within the correlation window leading to a stronger correlation. While downsampling the data provided an increase in displacement inaccuracy, it benefited from reducing computational burden, thus allowing for a greater volume of interest to be analyzed. By utilizing both full resolutions and downsampled resolution data, multiple displacements and strain views could be obtained for the compressed copper epoxy. The equivalent von-mises strain was between 0.08 to 0.11  $\mu\text{m}/\mu\text{m}$  and was shown to propagate from the compressed sample's center hole. The development of strain around a strain concentration is prevalent in many works and highlights the particle seeding technique's successfulness for strain measurements.

By utilizing the previously discussed information, some key findings could be made on the analysis and behaviour of copper filled PLA samples manufactured through FFF. The bulk response of the material, manufacturing tolerance, and material geometry was quantified through image segmentation. Of these three parameters, the sample raster and air gap configuration were particularly crucial for understanding the material strain measurements. The directional strain tensors were shown to be concentrated within regions that are surrounded by air gaps.



Transverse strains  $\epsilon_{xx}$ , and  $\epsilon_{yy}$  are shown to develop on the material shell in bands visualized in 3D to highlight their variation in the material's bulk. The 1D variation of strain  $\epsilon_{xx}$  and  $\epsilon_{yy}$  were plotted and shown to be between 0.03 to -0.035  $\mu\text{m}/\mu\text{m}$  and 0.069 to -0.08  $\mu\text{m}/\mu\text{m}$  for the 100-150 N load dataset, respectively, and 0.083 to -0.081  $\mu\text{m}/\mu\text{m}$  and -0.125 to 0.157  $\mu\text{m}/\mu\text{m}$ . The longitudinal strain  $\epsilon_{zz}$ , on the other hand, was shown to develop within the internal rasters of the material at diagonal bands between material air gaps. This strain tensor is particularly significant as this view of strain is not obtainable through other measurement techniques without modifying the sample to expose internal features. Additionally, the utilization of a more aggressive metal filter on the  $\mu$ -CT side will reduce the effects of scattering and beam hardening. Of final importance is the magnitude of  $\epsilon_{zz}$ , which is seen to be between 0.011 to 0.012  $\mu\text{m}/\mu\text{m}$ , which was significantly smaller than  $\epsilon_{xx}$  and  $\epsilon_{yy}$ . This development of strain was due to the material's shell being in direct alignment with the load cell, which could be seen in the  $\mu$ -CT images, thus bearing a higher strain.

In conclusion, DVC proved a useful tool for examining the internal strain behaviour of complex materials. The implication for this work in the scientific community revolves around fundamentally what this thesis was looking to achieve. Broadly this work looked to establish a methodology from which a sample can be prepared, imaged, and then 3D deformation behaviour analyzed. First, to accomplish this goal, a method was presented to allow high-quality  $\mu$ -CT images to be obtained that are compatible with the DVC correlation based on the artificial seeding technique. It was then necessary to present a way to allow complete analysis and evaluation of the sample speckling quality. The method showed the added benefit of simultaneously measuring errors, and consolidating DVC parameters was presented. This analysis was then utilized to meet the ultimate goal of this study, the analysis of the deformation behaviour of advanced material, by

examining a compressed epoxy sample's internal strain behaviour with a center hole and FFF composite loaded in tension.

## **5.2 Recommendations**

The artificial speckling methodology, in conjunction with  $\mu$ -CT and DVC, has proved a versatile method for the analysis of complex materials. The recommendations provided in this section of the report will ensure repeatable and successful DVC experimentation. These recommendations have been based on best practice guidelines developed through the author's thesis work experience. These recommendations are broken up into three main sections: 1) sample preparation, 2)  $\mu$ -CT image parameters, and 3) DVC analysis.

When preparing a seeding sample, one must select particles with a differing and preferably higher density than the medium that the particles are to be embedded inside. The difference in density becomes particularly essential when seeding low-density polymers as this will allow for each phase to appear within the  $\mu$ -CT images. High-density particles will provide the necessary variation in greyscale distribution required for correlation. Additionally, smaller speckling particles seem to give a better distribution, but it is important to note that these particles must be in the resolution range of the  $\mu$ -CT. Nano-particles may not provide the desired contrast, as they may be impossible to resolve via the  $\mu$ -CT machine. Finally, working with particles of much larger density to the matrix, particles may settle toward the bottom rather than remain in the material's bulk. It is recommended to choose fast curing matrix materials or expedite the curing time through heat curing or photocuring to mitigate particle settling in the case of thermosetting material or expediting the solidification process of thermoplastics through means such as a cooling system. These processes will ensure that most particles remain suspended within the sample instead of settling towards the bottom.

Selecting proper  $\mu$ -CT image parameters can allow for better image quality for ease of segmentation analysis and ensure repeatability for DVC studies. When working with metal particles, there is a tendency for these particles to create artifacts in the form of beam hardening and scattering. While post-scanning filtration may help reduce these effects, this author's opinion is that the best course of action is to select  $\mu$ -CT parameters that diminish their presence. The manufactures of the  $\mu$ -CT used in this study provided best practice guidelines for imaging, which were followed in this work. However, these settings do not seem to consider the presence of high-density particles leading to metal artifacts. Thus, this author's opinion is that increasing frame averaging and rotation step may help reduce artifacts.

When imaging with  $\mu$ -CT to utilize loading data image for DVC, it is recommended that as many imaging parameters as possible be kept the same for each load. While  $180^\circ$  rotation reduces the overall scan time, and as shown, able to produce valid datasets for DVC, in future studies, it may be recommended to utilize  $360^\circ$  scans to ensure the start position is also kept the same between load steps. A higher quality material test stage (MTS) would lead to ideal loading conditions for sample loading. The MTS provided by the CT manufacturers has a lack of rigidity that can affect DVC results. For higher accuracy testing, a more rigid structure can reduce RBD and sample set up time. Additionally, the loading parameter and information from the load cell is limited. Of final note, the open-source DVC software was restricted to only four subsets and reporting the cross-correlation peaks. One may wish to modify this code to allow for larger or smaller subsets depending on the expected scale of material deformation. One may also want to have the software output a more meaningful correlation quantity, such as the normalized cross-correlation or zero normalized cross-correlation.

### 5.3 Future Works

With the establishment of the artificial speckling technique and successful utilization of DVC to analyze FFF produced copper seeded PLA composites, several avenues are open for potential future research. A logical extension of the work may be to first study the effect of the seeding particles on the constituent mechanical properties of the material. Additionally, with the success of utilizing copper seeding within a common matrix material such as epoxy can be used as a starting point for the analysis of differing composites. Applying this technique by first seeding the epoxy with particles before impregnating it into the reinforcement phases of a laminate can allow DVC to measure the displacement and strain data during different loading conditions. This technique could potentially be used to help gain a greater understanding of the complex behaviour between the different phases and their interfaces.

Another potential research area is to utilize this technique for the analysis of the novel braided composite material. Braided composite's intricate weaving pattern, behaviour under loading, and thru-thickness interactions make them prime for analysis via DVC. A complete understanding of braided composites' deformation behaviour could be explored through the utilization of particle seeding and DVC. Besides the benefits already mentioned for composite laminates, insights could be gained about the yarns' internal behaviour within woven fibre tows.

On the side of additive manufacturing (AM), the DVC technique has been utilized in limited capacity as the works described in this thesis is one of the first to be conducted. Thus, there are several areas for unique research opportunities. A direct extension of the work done in chapter 4 can be completed by varying the printing parameter. Thus, the effects of infill percentage, print direction, print pattern, and layer thickness on mechanical properties can be investigated. Additionally, a comparison study between different filament compositions will provide valuable

information on deformation behaviour that can be utilized to select the appropriate material for practical applications. Finally, several other AM techniques such as stereolithography (SLA) printing, material jetting, binder jetting, and sheet lamination can benefit from analysis through DVC.

Finally, finite element analysis (FEA) models for composites are challenging to create due to the complex interaction between the material phases and requirements of accurate material and mechanical data. One of the upsides of DVC is its usefulness for the development of detailed analytical material models. As DVC is a volumetric measurement technique, testing on composite materials can be useful in validating new FEA models. Furthermore, DVC results can provide experimental data on crucial material parameters such as Young's modulus, shear modulus, and Poisson's ratio that can be used to build more complete models. Additionally, by utilizing the DVC displacement and strain data as inputs for FEA, the inverse problem can be solved to obtain maps of materials' mechanical properties with complex behaviours. Finally, displacement fields as inputs to develop models for the virtual field method will allow for the superior quantification of mechanical properties.

## Appendix A: Image Segmentation Formulations

### A.1: Image Dilation

The image dilation procedure increases the size of all white objects within an image. This procedure requires the image to be first converted to binary format, so all black pixels within the image are represented by 0 and white features 1. The image dilation procedure in function expands all objects within a region of interest by the desired size and kernel shape of the user. Figure A-1 shows the schematic representation of the image dilation procedure of a binarized image by a 3x3 square kernel. The 3x3 square kernel is superimposed onto the image, with the center of aligning with each white pixel. Figure A-1 d) the white space inside the image matrix is shown to increase by a single pixel. This process is mathematically shown in equation A.1, where  $A$  represents the reference image,  $B$  the structural element, and  $\oplus$  the image dilation procedure. The variable  $\hat{B}$  is representative of the reflection of structural element, which is overlapped on white pixels in image  $A$  at a set of pixel locations  $z$ . This process can be adapted for 3D images sets by replacing the 2D kernel with its corresponding 3D projection, thus expanding the size of white image voxels.

$$\mathbf{A} \oplus \mathbf{B} = (z|_z(\hat{B})_z \cap A \neq \emptyset) \quad \text{A.1}$$

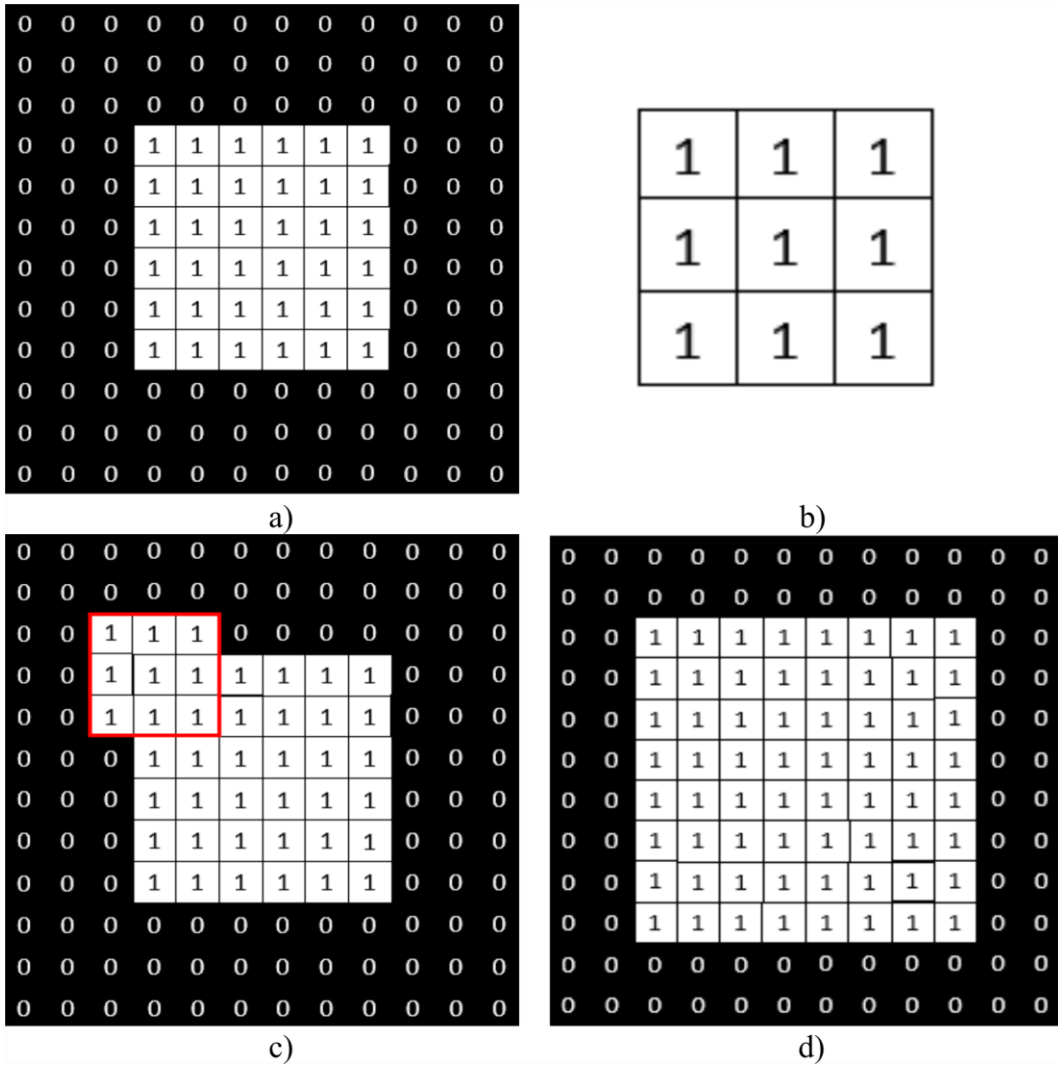


Figure A-1: Dilation procedure of binarized image: a) original image matrix, b) 3x3 square structural element, c) superposition of structural element, d) complete dilated image.

### A.2: Image Erosion

The image erosion procedure provides a digital method for reducing the size of all white features within a digital image. As with the image dilation procedure previously shown, the image erosion procedure discussed here requires the image first to be computed in binary. Image erosion works similarly to image dilation, just in reverse. Thus, all-white features within an image are reduced by the size of the corresponding kernel. Equation A.2 presents the underlying formula for

image dilation ( $\ominus$ ). This formula describes the overlapping of the structural element at each pixel location within the image and preceding elimination of each white pixel that is not surrounded by white pixels. Figure A-2 shows a graphical representation of the erosion procedure via a 3x3 structural element. Figure A-2 d) presents the final product of the image shown in Figure A-2 a) that has been eroded by the structural elements shown in Figure A-2 c). It is evident from this image that each white pixel that was not surrounded by other white pixels has been replaced by black pixels. As with image dilation, image erosion is easily expanded into 3D by using the associated 3D kernel to reduce the size of white voxels.

$$A \ominus B = z|(B_z \subseteq A) \quad \text{A.2}$$



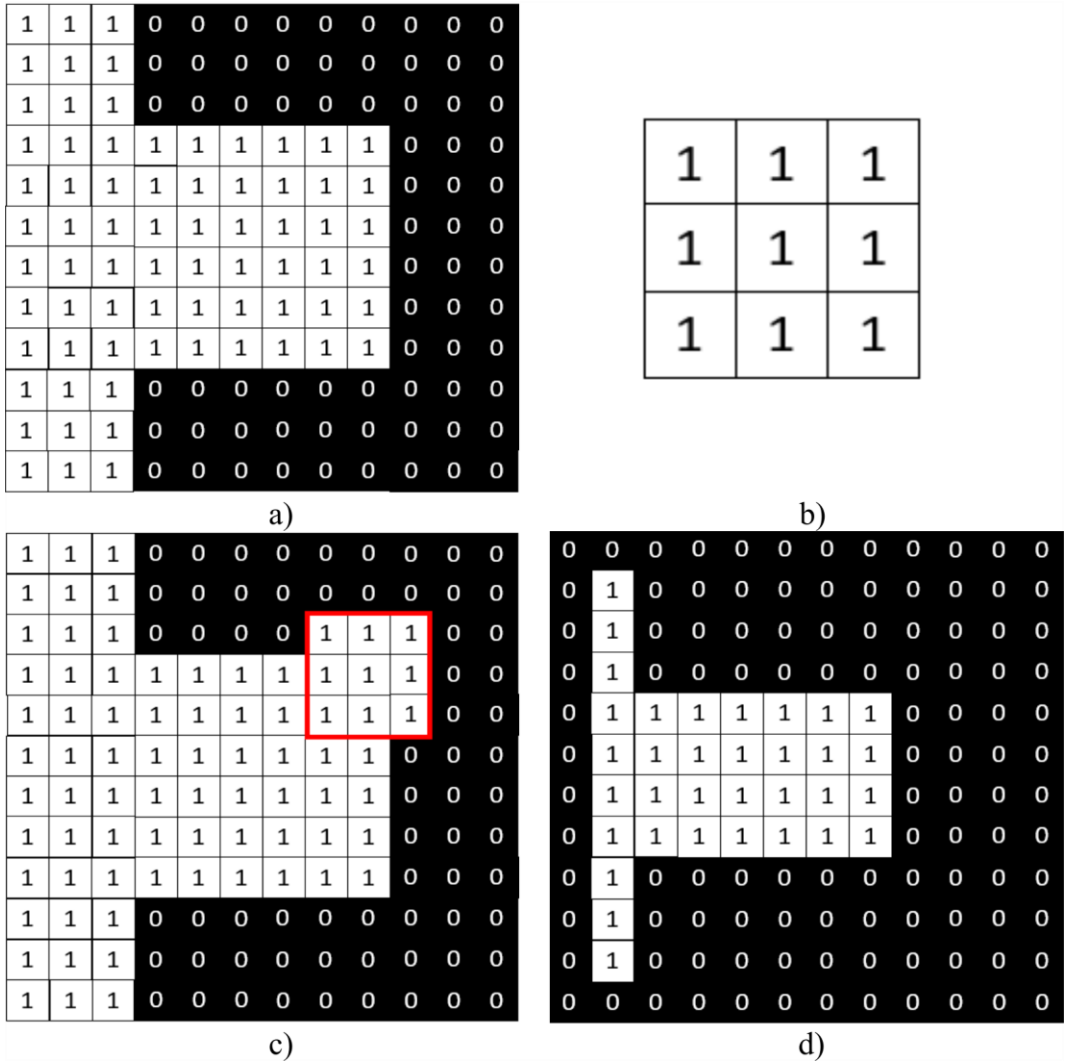


Figure A-2: Erosion procedure of binarized image: a) original image matrix, b) 3x3 square structural element, c) superposition of structural element, d) complete eroded image

### A.3: Morphological Closing

The equation A.3 defines the morphological closing operation. A morphological closing procedure is undergone by first applying a dilation to increase of all-white features within the image. The dilation is then accompanied by following image erosion by the same kernel. Figure A-3 shows an image matrix that has gone through a morphological close by a 3x3 square structural element. The growth of the image due to the dilation procedure can be seen in Figure A-3 c). This image then goes through an erosion procedure that leads to the final image shown in Figure A-3

d). It is immediately evident that the closed image looks completely different than the initial image shown in Figure A-3 a). The benefits of the closing procedure are that elements without other features in its vicinity remain the same size, while others are connected.

$$A \bullet B = (A \oplus B) \ominus B$$

A.3

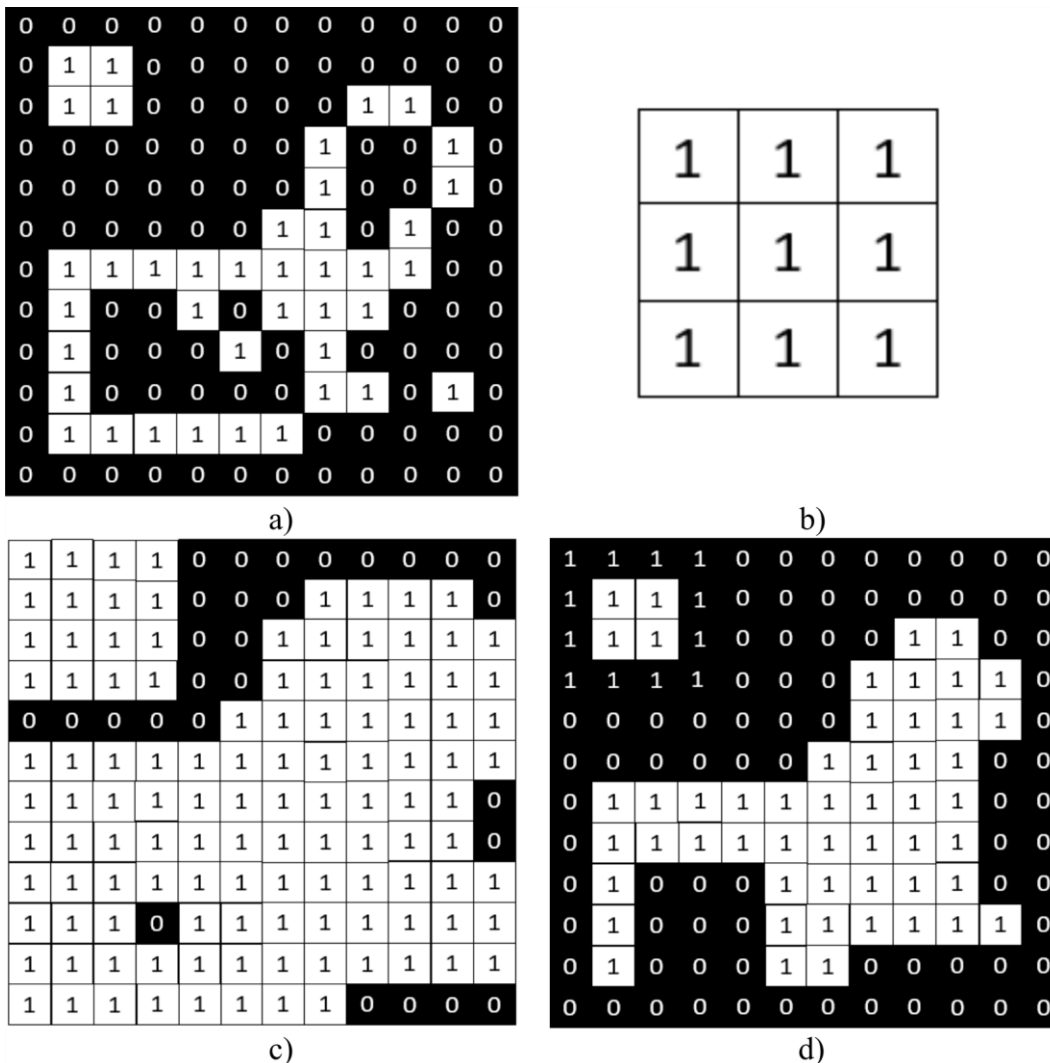


Figure A-3: Morphological closing procedure of binarized image: a) original image matrix, b) 3x3 square structural element, c) image dilation, d) erosion of the dilated image

#### A.4: Despeckling

There are many different methods, formulations, or filters for achieving a despeckling operation. However, all methods look to achieve the same results, which is remove all features below a specified size and shape, while keeping all features above the designated size. This method

has become incredibly useful for removing noise within an image space. Thus, rather than provide a specific formulation for this procedure, it is more important to demonstrate the process, which is shown in Figure A-4. All features below the size of the 3x3 structure element in Figure A-4 a) have been removed from the final image in Figure A-4 c). Thus, only large features are presented within the image shown in Figure A-4 c) effectively removing image noise.

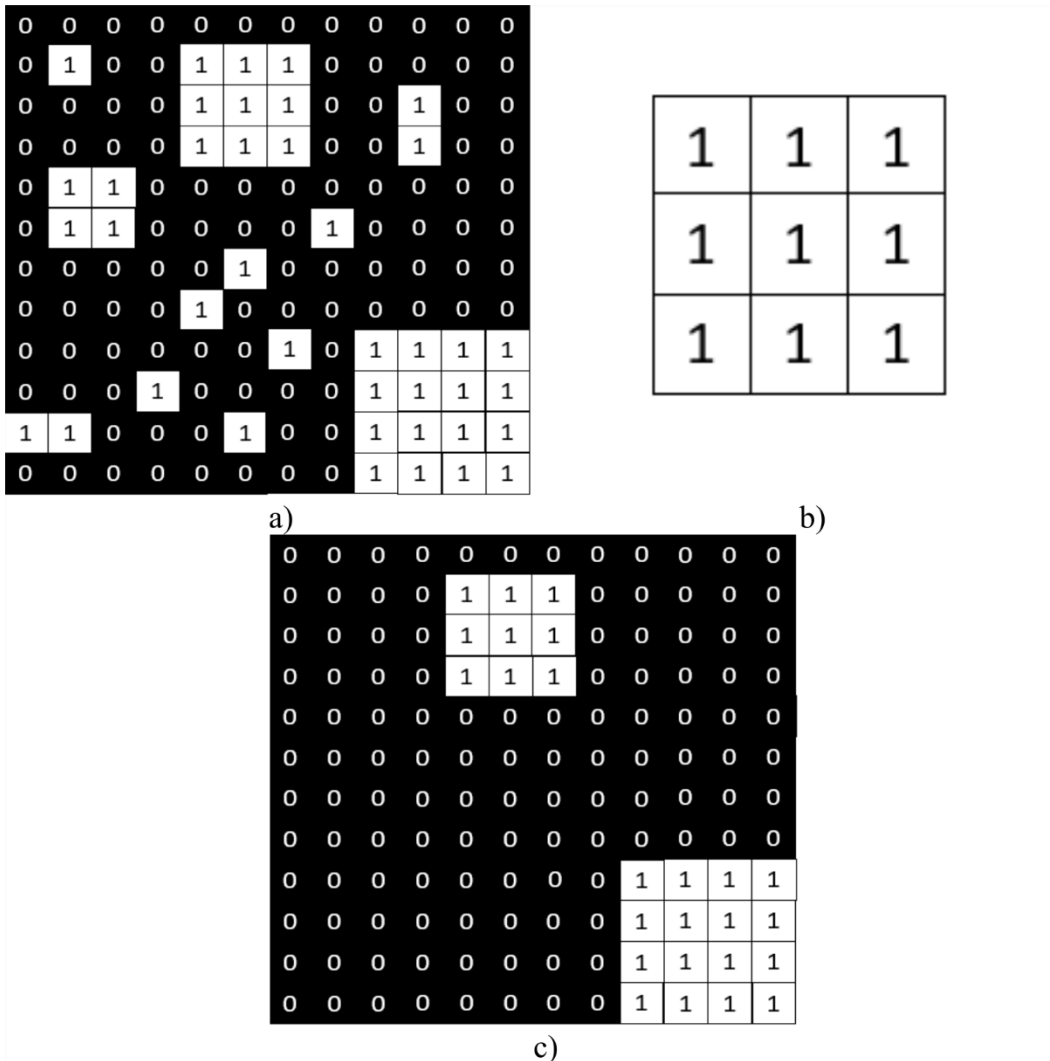


Figure A-4: Despeckling procedure of binarized image: a) original image matrix, b) 3x3 square structural element, c) despeckled image

## Appendix B: MATLAB Code

### B.1: Image Stack Crop

This program was developed to allow for batch cropping of the  $\mu$ -CT dataset.

```
% Author: Cristofaro Timpano
```

```
% Date: September 9, 2020
```

```
% this program allows for the batch cropping of micro-CT images to reduce % the overall data size of the image set for DVC. This program will crop the same area from each % sample, thus ensuring a similar volume of interest between reference and deformed data
```

```
% the name of the file for the sample code is 'ImageXXXXX' where X is a series of numbers
```

```
% search for the first file in the dataset (one can change *.bmp to the file extension their image % data is capture in, i.e. *.tif, *.jpg, *.png, etc.)
```

```
[file, path]=uigetfile('*.bmp');
```

```
% combine the file name and file path of the image to create the full file string
```

```
Filename=strcat(path,file);
```

```
% read the first image file and saving its data to a MATLAB variable
```

```
I=imread(Filename);
```

```
% selecting the crop window size
```

```
[j, rect2]=imcrop(I);
```

```
% x-coordinate in pixels relative left edge of the image of the cropping rectangles upper left corner
```

```
x2=rect2(1,1);
```

```
% y-coordinate in pixels relative left edge of the image of the cropping rectangles upper left corner
```

```
y2=rect2(1,2);
```

```
% looping over all images in the designated file path and crop them down to specified size
```

```
% replace k with the number of images you wish to crop over
```

```
for x=1:k
```

```
    % set the file indicator number for the first file you wish to start at, i.e. Image00128
```

```
    X=sprintf('%05d',127+i);
```

```
    % image file name
```

```
    Name=strcat('Image', X, '.bmp');
```

```
    % create the file path extension for the image
```

```
    File=strcat(path, Name)
```

```
    % read the image file
```

```

    Img=imread(File);

    %crop down the file to a rectangle with the top left corner at x2, and y2, and width and
    %height of x and y pixels, not MATLAB always adds a pixel to cropping, so you must
    %subtract by 1 to get the desired size

    ImgCrop=imcrop(Img, [x2, y2, x-1, y-1]);

    %create the new file path to save the cropped image data to
    FL=strcat('C:\croppeddata\', Name);

    %write data into a new file path
    Imwrite(ImgCrop,FL);
end

%crop the deformed data set to create the same VOI as the cropped reference
%search for the first file in the deformed dataset (one can change *bmp to the file extension their
%image data is capture in i.e. *.tif, *.jpg, *.png, etc)
[file2,path2]=uigetfile(*.bmp');

%looping over all images in the designated file path and crop them down to specified size
%replace k with the number of images you wish to crop over

for x=1:k
    %set the file indicator number for the first file you wish to start at, i.e. Imagedef00128
    X=sprintf('%05d',127+i);

    %image file name
    Name2=strcat('Imagedef', X, '.bmp');

    %create the file path extension for the image
    File2=strcat(path2, Name2)

    %read the image file
    Img2=imread(File2);

    %crop down the file to a rectangle with the top left corner at x2, and y2, and width and
    %height of x and y pixels, not MATLAB always adds a pixel to cropping, so you must
    %subtract by 1 to get the desired size
    ImgCrop2=imcrop(Img2, [x2, y2, x-1, y-1]);
    %create the new file path to save the cropped image data to
    FL2=strcat('C:\croppeddata\', Name);

    %write data into a new file path
    Imwrite(ImgCrop, FL2);
end

```

## **B.2: Greyscale Histogram**

The development of this code was written to obtain the greyscale histogram for  $\mu$ -CT images. This code was adapted from a previous code developed by G.W. Melenka to convert tif files to MATLAB image stacks.

```
% Author: Cristofaro Timpano  
% Date: September 9, 2020
```

```
% search for the first file in the image dataset (one can change *bmp to the file extension their  
% image data is capture in i.e. *.tif, *.jpg, *.png, etc)  
[file, path]=uigetfile('*.*tif')
```

```
% combine the file name, and the path to create the full file string  
Filename=strcat(path, file)
```

```
% allocate a block of memory to save the image files. Set pixX to the x-resolution, pixY to the y-  
% resolution, and ImgN the number of images in your image stack  
I=Zeros(pixX, pixY, ImgN, 'unit8');
```

```
% loop over the image files and save within a 3D image matrix
```

```
For i=1:ImgN
```

```
    % set the file indicator number for the first file you wish to start at i.e. Image00128  
    X=sprintf('%05d', 127+i)
```

```
    % image file name  
    Name=strcat('Image', X, '.tif')
```

```
    % create the file path extension for the image  
    File=strcat(path, Name)
```

```
    % save the image file to the preallocate image block space  
    I(:, :, i)=imread(File)
```

```
End
```

```
% obtain the greyscale distribution of the 3D image matrix I  
[counts, binlocation]=imhist(I);
```

```
% save the 256 element vector of greyscale data to a variable  
Save('greyscalecounts.mat', counts)
```

### B.3: VTK Converter

The MATLAB program presented here was developed to convert the 3D matrix data output from FIDVC in the VTK format to allow for it to be visualized in 3D.

% Author: Cristofaro Timpano

% Date: September 9, 2020

% Required Prerequisites: Tim (2020). WriteToVTK

(<https://www.mathworks.com/matlabcentral/fileexchange/23416-writetovtk>), MATLAB Central File Exchange. Retrieved September 9, 2020.

% Instruction: this code has been developed to run the required MATLAB function to convert  
% MATLAB 3D matrix data to VTK Files for input into Paraview. To convert voxel data into  
% displacement data, you must multiply each value in the MATLAB matrix by the CT scan  
% resolution. Additionally, if any downsampling was conducted, one must multiply this by the  
% downsampled data.

% Function WriteToVTK(Variable, 'name of file')

% xs is the lower matrix size in x

% xf is the upper matrix size in x

% ys is the lower matrix size in y

% yf is the upper matrix size in y

% zs is the lower matrix size in z

% zf is the upper matrix size in z

% displacement in x

$U_x = u_{\{1,1\}\{1,1\}}(x_s:xf, y_s:yf, z_s:zf);$

% displacement in y

$U_y = u_{\{1,1\}\{1,2\}}(x_s:xf, y_s:yf, z_s:zf);$

% displacement in z

$U_z = u_{\{1,1\}\{1,3\}}(x_s:xf, y_s:yf, z_s:zf);$

% displacement in magnitude

$U_m = u_{\{1,1\}\{1,4\}}(x_s:xf, y_s:yf, z_s:zf);$

% strain xx

$e_x = E_{ij\{1,1\}\{1,1\}}(x_s:xf, y_s:yf, z_s:zf);$

% strain yy

$e_y = E_{ij\{1,1\}\{2,2\}}(x_s:xf, y_s:yf, z_s:zf);$

% strain zz

```
ez=Eij{1,1}{3,3}(xs:xf, ys:yf, zs:zf);
```

```
%strain xy
```

```
txy=uij{1,1}{1,2}(xs:xf, ys:yf, zs:zf);
```

```
%strain xz
```

```
txz=uij{1,1}{1,3}(xs:xf, ys:yf, zs:zf);
```

```
%strain yz
```

```
tyz=uij{1,1}{2,3}(xs:xf, ys:yf, zs:zf);
```

```
WriteToVTK(Variable (i.e. ux), 'name of file')
```